

ISSN:2538-516X

Journal of  
**Civil  
Engineering  
Researchers**

Volume: 5; Number: 2; June 2023

Chief Editorial:  
Morteza Jamshidi

Managing Editor:  
Kamyar Bagherineghad



**J-Researchers**



**Volume 5, Number 2, June 2023**

## **Contents**

1. **Evaluation of Mechanical Properties and Microstructure of Pozzolanic Geopolymer Concrete Reinforced with Polymer Fiber** 1-13  
Mohammadhossein Mansourghanaei
2. **Three-dimensional simulation of granular materials by discrete element method (DEM) by considering the fracture effect of particles** 14-28  
Amir Mahboob, Omid Hassanshahi, Ashkan Sarabi Tabrizi
3. **Investigating the relationship between NDVI and EVI vegetation indices with ground surface temperature in Tehran** 29-35  
Amir Nazarinejad, Mehrdad Nourbakhsh
4. **A review on Simulate Fracture and Ultra-Low Cycle Fatigue in Steel Structures by ABAQUS** 36-45  
Ali Mirzaee, Ayoub Harouni Kajal
5. **Investigating the effectiveness of fluid viscous damper in reducing the effect of seismic sequence on steel bending frame designed on type c soil** 46-54  
Javad Pourali
6. **Evaluation of effective operation parameter on High Efficiency Particulate Air and Ultra Low Particulate Air filters** 55-60  
Seyed Mohammad Hosseini, Sepideh Sahebi



## Evaluation of Mechanical Properties and Microstructure of Pozzolanic Geopolymer Concrete Reinforced with Polymer Fiber

Mohammadhossein Mansourghanaei <sup>a\*</sup>

<sup>a</sup> Ph.D. in Civil Engineering, Department of Civil Engineering, Chalous Branch, Islamic Azad University, Chalous, Iran

**Journals-Researchers use only:** Received date: 2023.04.10; revised date: date 2023.05.21; accepted date: 2023.05.27

### Abstract

in recent decades, Geopolymer concrete (GPC) is a new material in the construction industry, which has favorable performance and workability and contains aluminosilicate materials full of silicate (Si), aluminum (Al), and alkaline solution as a binder. The advantages of using geopolymer materials instead of cement in concrete are not limited to high mechanical and microstructural properties. It also has a remarkable effect in reducing greenhouse gas emissions. In the current study, Granulated Blast Furnace Slag (GBFS) GPC was used with 0-2% polyolefin fibers (POFs) and 0-8% nano-silica (NS) to improve its structure. After curing the specimens under dry conditions at a temperature of 60 °C in an oven, they were subjected to compressive strength, tensile strength, elastic modulus, ultrasonic pulse velocity (UPV) and impact resistance tests to evaluate their mechanical properties. The addition of NS enhanced the whole properties of the GBFS geopolymer concrete. The compressive strength, tensile strength, and elastic modulus of the concrete increased by up to 22%, 14%, and 24%, respectively. Besides, it leads to ultrasonic wave velocity enhancement to 12% in the room temperature. The addition of the fibers to the GPC significantly increased the tensile strength (by up to 9%) and the energy absorbed due to the impact. Moreover, compared to Concrete containing ordinary portland cement (OPC), the GPC demonstrated much better mechanical and microstructural properties. Besides, the presence of POFs in the GPC compound substantially affects tensile strength and resistance against an impact. Accordingly, the sample's tensile strength had an improvement by 8.4% in the room temperature. In the following, by conducting the X-Ray Fluorescence (XRF), X-Ray Diffraction (XRD), and Scanning electron microscope (SEM) tests, a microstructure investigation was carried out on the concrete samples. In addition to their overlapping with each other, the results indicate the GPC superiority over the regular concrete. © 2017 Journals-Researchers. All rights reserved. (DOI: <https://doi.org/10.52547/JCER.5.1.1>)

### Keywords :

Geopolymer Concrete, Granulated Blast Furnace Slag, Nanosilica, Polyolefin Fibers, Mechanical Properties, Microstructure.

\* Corresponding Author. Tel: +989121712070; E-mail: Mhm.Ghanaei@iauc.ac.ir

## 1. Introduction

GBFS and NS containing abundant aluminosilicate materials are known as synthetic pozzolans. Using this material instead of cement can improve concrete resistance and decrease the increasing demand for its usage in concrete [1,2]. Comparing the concrete containing regular Portland cement with GPC, McNulty [3] asserted that the geopolymer concretes have higher compressive strength. The properties and the bonding type are different in regular and geopolymer concretes. The bonding in regular concretes is based on calcium oxide hydration and silicon dioxide reactions in order to form calcium silicate hydrate. However, the GPC bonding is established via alkaline activator contact with the Aluminosilicate raw materials, reshaped in the polymerization reaction product, and slowly cooled in a high pH medium and hydrothermal condition (hydrothermal condition is referred to the chemical reactions in the presence of solvent in higher pressure and temperature). This structure (related to the geopolymer concrete) has some merits compared to the regular concrete, e.g., it provides better resistance performance at higher temperatures [4]. The presence of NS in GPC not only has a positive effect on its physical and mechanical properties but also accelerates the geopolymer reaction, reduces the system's alkalinity, and thus, lowers the degradation of the used fibers [5]. It also increases the compressive strength of the geopolymer concrete. This rise occurs at the Si/Al ratios of up to 2% in the mixture. However, the addition of more than the optimal value of NS particles, reduces the compressive strength [6]. Improved compressive strength [7], elastic modulus, and UPV have been reported with the use of NS in GPC [8]. Another study on the GPC cured at the ambient temperature has investigated the effect of adding 0% to 10% NS to specimens with different concentrations of activator liquid (NaOH) (M 8, 10, 12). The optimum compressive strength and tensile strength coefficient were obtained by adding 6% NS [7]. Preventing the connection of pores and bonding the flow channels in the concrete, the POFs strengthen it and avoid its spalling [9]. A study on the effect of POFs with various lengths and diameters on different geopolymer concretes has shown that the proper use of fibers raises the tensile strength, elastic modulus, and impact energy. The addition of fibers reduces the

compressive strength [10]. The addition of POFs to a concrete beam remarkably improves its strength after cracking by increasing its elastic modulus [11]. The Crack Mouth Opening Displacement (CMOD) analysis has also indicated that the POFs have proper bonding properties and, due to their proper stiffness, they can keep the concrete pieces beside each other after the initial cracking [12]. In a study into the effect of adding 0.5% POFs on the geopolymer concrete, a reduction by 12% to 15% was observed in the compressive strength. The reduction was larger in the specimens containing fibers with a length of 55 mm compared to those with a length of 44 mm [13, 14]. This study mainly aims to investigate the mechanical and microstructural properties of the geopolymer concretes based on the GBFS containing NS and also reinforced with POFs. For this purpose, the compressive and tensile strength, modulus of elasticity, and impact tests have been conducted. In order to accurately analyze the ultrasonic wave's velocity test and also the relationship between the compressive strength and tensile strength, the compressive strength and modulus of elasticity, the compressive strength and ultrasonic wave velocity have also been examined. Ultimately, the microstructure was examined by caused by samples' by SEM, XRF and XRD tests.

## 2. Experimental Program and Test Methods

### 2.1 Materials

In this experimental study, the Portland cement type II with a  $2.35 \text{ gr/cm}^3$  of specific weight according to standard En 197-1 and the GBFS was used in powder form with the specific weight of  $2.45 \text{ g/cm}^3$  according to ASTM C989/C989M standard. The chemical properties of these materials are indicated in Table 1. The used fine aggregates were natural clean sand with a fineness modulus of 2.95 and a specific weight of  $2.75 \text{ g/cm}^3$ , and the coarse aggregates were crushed gravel with a maximum size of 19 mm and a specific weight of  $2.65 \text{ g/cm}^3$  according to the requirements of the ASTM-C33. The curing was performed at a temperature of  $60^\circ\text{C}$  according to the standards of the geopolymer concrete. The NS particles made up of 99.5%  $\text{SiO}_2$  with an average diameter in the range of 15 to 25 nm were used. Crimped POFs, 30 mm in length, were also used according to ASTM D7508/D7508M standard. whose physical properties are shown in Tabel. 2.

## 2.2 Mix Design

Six mix designs according to ACI 211.1-89 standard, one as ordinary concrete (OPCNS0PO0) and five with different NS and polyolefin fiber percentages, were considered in the study. The GPC specimens were divided into two major groups. The first group had no POFs and 0-8% NS. The second group contained 8% NS (GPCNS0PO0, GPCNS4PO0 and GPCNS8PO0) and 1% or 2% POFs (GPCNS8PO1 and GPCNS8PO2). A superplasticizer was used to achieve the same workability in all mix designs with a slump of  $100 \pm 20$  mm. Moreover,  $202.5 \text{ kg/m}^3$  Alkia alkaline solution was added to the geopolymer specimens. The used alkaline solution is a combination of NaOH and  $\text{Na}_2\text{SiO}_3$  with the weight ratio of 2.5, utilized with the mixture specific weight of  $1483 \text{ kg/m}^3$  and the concentration of 12 M. The conducted studies indicate that due to the significant level of C-S-H formation when utilizing  $\text{Na}_2\text{SiO}_3$ , using a combination of NaOH and  $\text{Na}_2\text{SiO}_3$  increases the compressive strength compared to single employment of CaOH [15]. Table 3 lists the mix designs of the specimens.

Table 3  
Details of The Mix Designs

Mix ID	Cement	GBFS	Water	Alkaline Solution	NS	Coarse Aggregates	Fine Aggregates	Polyolefin Fibers	Super Plasticizer
(Kg/m <sup>3</sup> )									
OPCNS0PO0	450	0	202.5	0	0	1000	761	0	9
GPCNS0PO0	0	450	0	202.5	0	1000	816	0	9
GPCNS4PO0	0	432	0	202.5	18	1000	767	0	10
GPCNS8PO0	0	414	0	202.5	36	1000	718	0	11
GPCNS8PO1	0	432	0	202.5	36	1000	672	24	11
GPCNS8PO2	0	432	0	202.5	36	1000	646	48	11

## 2.3 Test Methods

After fabricating the samples, for better curing and increasing the resistance properties, the samples were placed in an oven at  $60^\circ\text{C}$  with a thermal rate of  $4.4^\circ\text{C/min}$  for 48 h. In this study, the compressive strength tests were performed on  $100\text{-mm}^3$  cubic specimens based on BS EN 12390 [16]. Furthermore, to determine the tensile strength of the cylindrical specimens (15 cm in diameter and 30 cm in length),

Table1

Chemical Compositions of Materials

Component	GBFS (%)	Portland cement (%)
$\text{SiO}_2$ (%)	29.2	21.3
$\text{Al}_2\text{O}_3$ (%)	19.4	4.7
$\text{Fe}_2\text{O}_3$ (%)	5.8	4.3
CaO (%)	38.6	62.7
MgO (%)	2.8	2.1
$\text{SO}_3$ (%)	2.6	2
$\text{K}_2\text{O}$ (%)	0.1	0.65
$\text{Na}_2\text{O}$ (%)	0.2	0.18
$\text{TiO}_2$ (%)	0.6	-
Free Cao (%)	-	1.12
LOI (%)	0.3	1.84
Blaine ( $\text{cm}^2/\text{g}$ )	2200	3200

Table 2

Physical Properties of The Fiber Steel (FS)

Tensile Strength ( $\text{N/mm}^2$ )
Length (mm)
Diameter (mm)
Elasticity Modulus (G.Pa)
Bulk Density ( $\text{g/cm}^3$ )

the splitting tests were conducted based on ASTM C496 [17]. The test of modulus of elasticity of concrete under the standard ASTM C469 [18] was carried out on concrete samples (15 cm in diameter and 30 cm in length). The UPV tests [19] were conducted according to ASTM C597 using a non-destructive ultrasonic electronic apparatus, PUNDIT MODEL PC1012, with an accuracy of  $\pm 0.1 \mu\text{s}$  for a transformer with a vibrational frequency of 55 kHz and a movement time accuracy of  $\pm 2\%$  for the

distance. The concrete's resistance to dynamic loads (impacts) was measured using the drop weight hammer test according to the report by the ACI 544-2R committee [20]. This test was conducted with repeating impacts on disks with a diameter of 15 cm and a height of 63.5 cm. It should be noted that 264 concrete samples were made in this research. So that for compressive strength (54 samples), tensile strength (54 samples), modulus of elasticity (54 samples), UPV (54 samples) and impact test (36 samples) the results of each stage, the average obtained from performing the test on three laboratory samples is. In the SEM (6 samples) and XRD (6 samples) tests, the results are based on one sample.

### 3. Results and Discussion

#### 3.1 Results of The Compressive Strength, Tensile Strength and Elastic Modulus Tests

As shown in Fig. 1 and Fig. 2, with the rise in the POFs content, the compressive strength reduced by 20-22%. The reason for the reduction in the compressive strength of specimens containing POFs can be the micro internal defects in the geopolymer matrix caused by the additional fibers [21], and by adding 1% and 2% fibers, the tensile strength grew by 4% and 8%, respectively. Moreover, the addition of 4% and 8% NS increased the compressive strength by 10% and 22%, and the tensile strength by 11% and 15%, respectively. The standard deviation in the compressive strength test at the ages curing of 7, 28 and 90 days was obtained as 9.08, 8.22 and 7.74, respectively. and the standard deviation in the tensile strength test at the ages curing of 7, 28 and 90 days was obtained as 0.46, 0.48 and 0.37, respectively. The smallness of the standard deviation shows that the data are close to the average and the data has less dispersion. The influence of the NS in improving the strength can be attributed to the following multi-stage mechanism that improves the concrete's microstructures and thus, increases the mechanical properties.

1. The rise in the pozzolanic reaction [5]. The presence of NS in the GPC accelerates the pozzolanic reaction.

2. The filling effect of NS particles [22, 23]. First, the distribution of NS particles besides the other concrete particles results in a denser matrix. Second, the NS's reaction in the geopolymerization procedure produces a larger amount of aluminosilicate gel, along with the reaction products of the main materials. The reaction by-product is likely to deposit in the structure of the existing pores. The rise in  $\text{SiO}_2$  increases the matrix density [24]. Therefore, the filling effect of NS is improved by the particle packing, and the by-product produces a denser matrix, reducing the porosity and increasing the strength.

3. It acts as a nucleus [25, 26]. In the C-S-H gel structure, nanoparticles can act as a nucleus and form strong bonds with the C-S particles of the gel. Thus, during the hydration, the products' stability increases, and the durability and mechanical products are expected to improve.

The elastic moduli of specimens are plotted in Fig. 3. The rise in the elastic modulus caused by the addition of 1% and 2% fibers to the specimens was 1.5% and 7%, respectively. Moreover, adding 4% and 8% NS increased the elastic modulus by 12% and 13%, respectively, compared to the specimens without NS. The addition of NS to the fiber-reinforced concrete has two results. First, the concrete density increases, leading to a rise in the elastic modulus. Second, as long as the pores of the concrete are not filled, increasing the NS raises the elastic modulus. However, the excessive increase in the amount of NS results in a lower dynamic elastic modulus.

The standard deviation in the elastic moduli test at the ages curing of 7, 28 and 90 days was obtained as 3.46, 4.32 and 3.73, respectively.

According to the drawing of the standard deviation for the ages curing of 7, 28, 90 days in each three chart, it can be seen that the results in OPC compared to GPC have a big difference with the standard deviation. This is due to the superior mechanical properties of GPC compared to OPC. With the increase of curing age in the samples, the standard deviation values have decreased and this is due to the completion of the hydration process (in OPC) and geopolymerization (in GPC) in concrete.

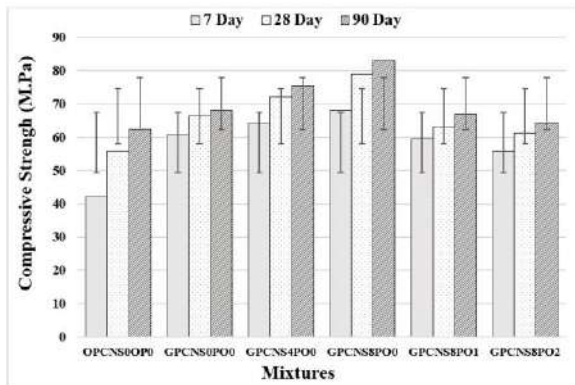


Fig. 1. The Compressive Strengths of The Specimens

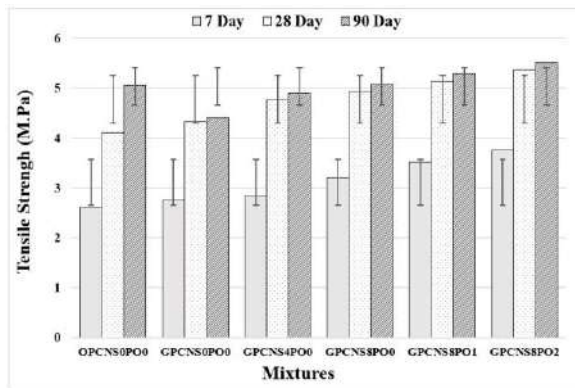


Fig. 2. The Tensile Strengths of The Specimens

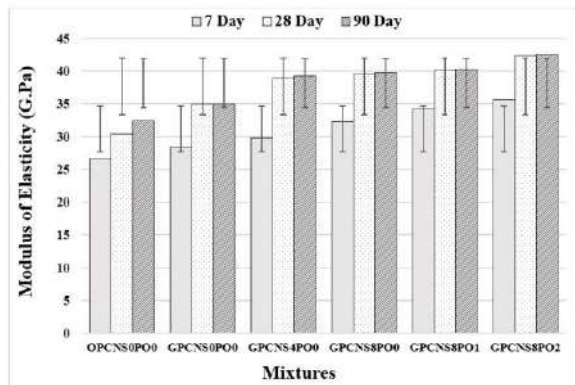


Fig. 3. Elastic Modulus Variations of The Specimens

### 3.2 Relationship Between The Compressive Strength With Tensile Strength and Elastic Modulus

Table 4 lists the relationships between the compressive and tensile strength (splitting) proposed by various researchers. These relationships are obtained based on the output of the excel chart of compressive strength and tensile strength. In this table Eq. 1 is obtained for ordinary concrete, while Eq. 2 is provided for GPC cured at a temperature of 60 °C in an oven. Eq. 3 is the relationship between the strengths in the GPC cured at the ambient temperature. Eq. 4 is the equation on GPC and OPC obtained in the current study. According to the software information, the difference between relation 1 and relation 4 is 12%, also the error rate in relation 2 is about 8%, the amount of this difference compared to relation 3 is 37%.

Table 5 demonstrates the elastic modulus variations against the changes in the compressive strength. These relationships are obtained based on the output of the excel chart of compressive strength and elastic modulus. The elastic modulus increases with the compressive strength. The predictions of the elastic moduli of the specimens are presented with respect to the compressive strength obtained in the current study using the relationships provided in Table 5. In this table Eq. 5 is for the OPC, and Eqs. 6 and 7 are for the GPC. Eq. 8 is the equation on GPC and OPC obtained in the current study. Relationship number 5 is in good agreement with the relationship obtained from OPC and GPC in this research. The average error value in relation 5, 6 and 7 compared to the laboratory results in this research is about 7, 6 and 28%, respectively, and the large difference of this value in relation 7 is due to the importance of curing at ambient temperature and 60 °C for concrete. It is in relationships 7 and 8.

Table 4

Relationships Predicting the Tensile Strength Based on The Compressive Strength

Eq. Number	Equation	Reference
1	$f_t = 0.59\sqrt{f_c}$	ACI363R-92 [27]
2	$f_t = 0.93(f_c)^{0.5}$	Nath [28]
3	$f_t = 0.69(f_c)^{0.5}$	Diaz [29]
4	$f_t = 0.2172(f_c)^{0.7158}$	Present Eq

Table 5  
Relationship Between the Elastic Modulus and Compressive Strength of Specimens

Eq. Number	Equation	Reference
5	$E_c = 3320(f'_c)^{0.5} + 6900$	ACI 363 [30]
6	$E_c = 0.037 \times \rho^{1.5} (f'_c)^{0.5}$	Diaz-Loya et al (GPC) [31]
7	$E_c = 3510(f'_c)^{0.5}$	Pradip and Sarker (GPC) [28]
8	$E_c = 2.3923(f'_c)^{0.6397}$	Present Eq

### 3.3 The Results of The Ultrasonic Pulse Velocity (UPV) Test

The velocities of the ultrasonic pulses passing through the specimens are shown in Fig. 4. The speed quality of ultrasonic waves based on IS 13311-1 [32] standard in four levels as follows: Doubtful with a speed below 3000 m/s, Moderate with a speed of 3000 to 3500 m/s, Good with a speed of 3500 to 4500 m/s and Excellent with a speed of More than 4500 m/s is divided. UPV method is used to estimate the concrete quality using the regression analysis between the compressive strength and the UPV[19]. The results indicated that the addition of fibers reduced the ultrasonic pulse velocity. This reduction was not significant being in the range lower than 12.5%. The small effect of fibers on the pulse velocity was also reported by Sahmaran et al. They attributed the negligible changes in the pulse velocity to the uniformity of the concrete matrix in all mixtures [33]. According to the obtained results, the whole 28-day and 90-day mix designs were considered in the "Excellent" range [34]. As long as the UPV values are classified as "Excellent", the concrete has no large cracks or pores that can affect the integrity of the specimen structure [35]. On the other hand, the obtained results revealed that the addition of NS increased the pulse velocity by filling the pores and densifying and integrating the concrete. Due to the curing in the dry environment of the oven, some fine cracks and pores were formed in the GPC preventing its full integrity, which allows for the

transmission of ultrasonic pulses with higher velocities. Therefore, the obtained velocities were slightly lower than those of ordinary concrete. Nevertheless, these cracks had very fine dimensions and could only influence the UPV having no remarkable effect on the compressive strength of the specimens [36]. lack of fibers and presence of more NS in mix design 4 (GPCNS8PO0) was very effective in making the velocity of the passing pulses close to those of the ordinary concrete. The amount of standard deviation in this test at the curing ages of 7, 28 and 90 days was obtained as 302, 306 and 426, respectively. The higher difference of the results in OPC compared to the standard deviation is due to the lower results in GPC in line with the heat curing in this type of concrete, which has led to the occurrence of micro cracks and the drop in results.

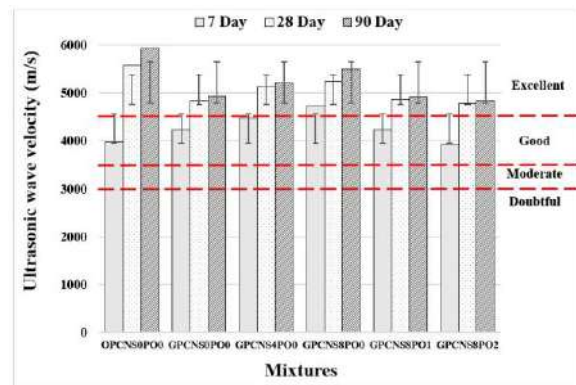


Fig. 4. The Variations in The Ultrasonic Pulse Velocities of The Specimens

### 3.4. Results of The Impact Resistance Tests

Table 6 shows the results of the impact resistance test. According to Eq. 9, the impact energy ( $E_n$ ,  $E_1$  for initial cracking and  $E_2$  for final fracture the sample) and the energy absorbed ( $E_2 - E_1$ ) in 90 days by different specimens are shown in Figs. 5 and 6, respectively. In all groups, with the rise in the polyolefin fiber percentage to 1% and 2%, the number of impacts required for both initial crack ( $N_1$ ) and the final fracture ( $N_2$ ) increased, i.e., the energy absorption capacity increased with the addition of fibers to the geopolymer concrete. The POFs



effectively resisted the crack initiation and propagation during the fracture of the concrete structure. They also relieved the stress concentration in the tips of the cracks and delayed their damage process under impact loads. With the rise in the loading, the cracks developed near the fibers until the separation could be observed in the surface of fibers in the matrix. Due to the tensile stress formed in the predicted path of cracks, when they reached the surface of fibers, the stress concentration in their tips was reduced, and their path deviated. These conditions prevented further crack propagation. This effect describes the bridging or capacity in limiting the cracks in the fiber-reinforced concrete. The results indicated a much greater effect of POFs on the impact resistance compared to the NS. In the current study, with the addition of 1% and 2% fibers to the specimens, the impact energy caused by the formation of the first crack ( $E_1$ ) increased by 13% and 30%, respectively. Moreover, the impact energy against full failure ( $E_2$ ) grew by 213% and 345%, respectively. As the results showed, the addition of fibers was more effective in the full failure compared to the first crack. By considering a ratio  $E_2/E_1$  as flexibility index of concrete, this in fact indicates the imposition of more blows for failure after the initial crack. Therefore, the addition of 1% and 2% fibers increased the flexibility index ( $E_2/E_1$ ) 2.8 and 3.4 times, respectively. With the addition of 1% and 2% fibers, the amount of absorbed energy ( $E_2 - E_1$ ) became 6.2 and 9.3 times larger, indicating the good ability of fibers in absorbing the impact energy. Adding 4% and 8% NS increased the energy required for the formation of the first crack ( $E_1$ ) by 62% and 77%, and the energy needed for full failure ( $E_2$ ) by 46% and 58%, respectively. Compared to the ordinary concrete, the GPC required 44% and 14% higher energy for the first crack ( $E_1$ ) and the full failure ( $E_2$ ), respectively.

In figure 5, the amount of standard deviation for  $E_1$ ,  $E_2$  and  $E_2/E_1$  is 161, 1252 and 1122 respectively. and in Figure 6, the amount of standard deviation for  $E_2 - E_1$

$E_1$  is equal to 1122. The large number of standard deviation is due to the dispersion of the results, as it can be seen that the results in GPC containing POFs are much more than other concretes. In this regard GPC containing 2% POFs has the highest dispersion of results.

$$E_n = N \times W \times H \quad (\text{Eq. 9})$$

$E_n$ : Impact Energy

N: Number of Impacts

W: hammer weight (According to ACI 544.2R = 4.54 kg)

H: Weight throw height (According to ACI 544.2R = 45.7 cm)

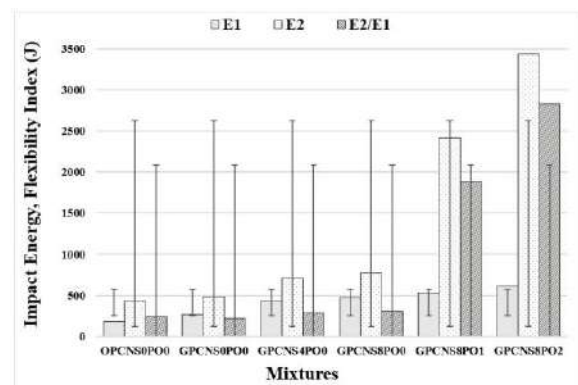


Fig. 5. The Impact Energy and The Flexibility Index of The Specimens

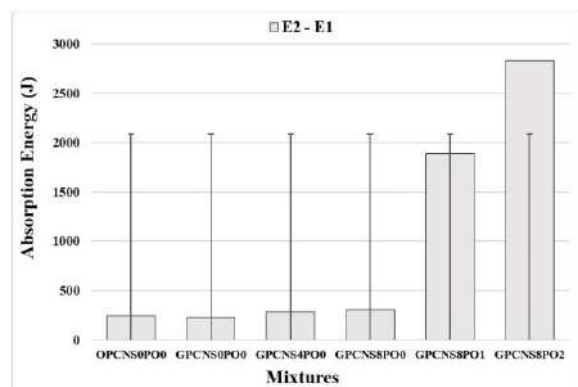


Fig. 6. Absorbed Energy of The Specimens

Table 6  
Results of The Impact Resistance Tests

Mix ID	N <sub>1</sub>	N <sub>2</sub>	N <sub>2</sub> -N <sub>1</sub>	E <sub>1</sub> (J)	E <sub>2</sub> (J)	E <sub>2</sub> -E <sub>1</sub> (J)	E <sub>2</sub> /E <sub>1</sub> (J)
OPCNS0PO0	9	21	12	183	427	244	2.33
GPCNS0PO0	13	24	11	264	488	223	1.58
GPCNS4PO0	21	35	14	427	712	284	1.67
GPCNS8PO0	23	38	15	268	773	305	1.65
GPCNS8PO1	26	119	93	529	2422	1892	4.58
GPCNS8PO2	30	169	139	610	3439	2829	5.63

#### 4. Results of the XRD, XRF and SEM Tests

The results obtained from the electron microscope can greatly help in identifying the structure and behavior of concrete. The mechanical and physical properties of the concrete matrix are considerably dependent on its microstructure. This section discusses the effect of NS and POFs on the microstructure of concrete paste using the SEM analysis.

Figure 7 shows the SEM of GPC containing NS reinforced with POFs (GPCNS8PO2). The role of bridging in cracks and keeping concrete integrated by adding fibers can be seen in SEM image ((b) GPCNS8PO2), which has a great effect on increasing tensile strength and impact resistance. Although the fibers change the direction of the cracks or prevent many cracks, but its lack of chemical composition with the materials in GPC has reduced the strength and previous research on concrete shows a decrease in compressive strength of concretes containing poly olefin fiber. The addition of NS reduces this reduction and creates better adhesion between the fibers and the concrete paste [5].

Figure 8 shows the difference between SEM Portland cement and GBFS geopolymer. Research by others has shown that in Portland cement, C-S-H gels contain silicon groups organized in finite linear chains of the "dreierketten" structure, so they are mainly SiO<sub>1</sub> and SiO<sub>2</sub> species. Geopolymer is characterized by high polymerization materials with aluminosilicate structure, which is mainly composed

of three cross-linked unit dimensions, including (SiO<sub>4</sub> (2Al) and SiO<sub>4</sub> (3A) [37]. Figure 9 shows the SEM of GBFS-based GPC containing NS. Obviously, NS-containing geopolymers show higher density and less porosity. This improvement can be attributed to two reasons. First, the nanoparticles fill the pores of the matrices, which reduces the porosity of the geopolymer nanocomposites, resulting in uniformity, less pores, and a more compact geopolymer matrix [5]. Second, the active silica particles improve the geopolymer reaction. In fact, the pozzolanic reaction condenses and homogenizes the microstructures by converting C-H to C-S-H [37], thus creating more geopolymer gel and a denser matrix [37]. However, further increase in NS content causes insufficient dispersion and accumulation of NS particles, which slightly reduces matrix density [39].

The key difference between NS-containing and non-silica microstructures is that NS-containing microstructures are denser with fewer unreacted particles, resulting in a softer, more integrated structure. In the sample containing NS, very few fine cracks are observed, in which NS acts as a filler to fill the spaces inside the hardened microstructure skeleton of the geopolymer paste and increase its compaction [6, 40]. NS geopolymer matrices appear to be composed of a larger amount of amorphous crystalline compound.

Fig. 10 demonstrates the XRD results with a radiation intensity of Ka  $\lambda=1.54060$  Å-Cu. In order to perform this test, the central parts of the specimens were turned into a uniform homogeneous powder. The XRD analysis showed that most peaks in the GPC occurred in zones 15 to 35. However, for the ordinary

concrete, the zones of the peaks were larger, being from 15 to 50. Moreover, 60 peaks were observed due to the arrangement and atomic structure of the specimens. Therefore, by evaluating the formation angles of the peaks and their relative intensities, the types of the materials and peak phases of the XRD could be identified. In the ordinary concrete, aluminum phosphate ( $\text{AlPO}_4$ ), calcium carbonate ( $\text{CaCO}_3$ ), and calcium manganese carbonate ( $\text{CaMn}_2\text{C}_2\text{O}_6$ ) had the highest dispersion, respectively. The largest peaks in the range of 25, 27, 29 and 60 angles are 3000, 22000, 2200 and 3000  $\text{cm}^{-1}$ . In the GPC without NS, sodium aluminum silicate ( $\text{NaAlSi}_3\text{O}_8$ ) and quartz ( $\text{SiO}_2$ ) were dispersed due to the presence of GBFS and pozzolanic reactions. In the specimen containing 8% NS,  $\text{BiPO}_4\text{OOH}$  and  $\text{Mg}_{16}\text{Si}_{16}\text{O}_{48}$  were dispersed, and the percentage of the total silica increased. The range of peaks in geopolymer is between 27, 28 and 29.5 and the value of the largest peak for non-nano GPC is 1400, 850 and 2000  $\text{cm}^{-1}$  and for sample 8% NS 1900, 4500 and 2100  $\text{cm}^{-1}$ . The addition of NS increased the geopolymerization reaction. Therefore, a greater amount of amorphous geopolymer gel was created in the matrixes. In turn, this showed that the nanoparticles prevented the reduction in the geopolymer strength [5]. In general, the addition of amorphous NS to geopolymer pastes has resulted in minor changes in crystallinity and amorphous. With the addition of NS, the amorphous content mainly increases, which reduces the crystalline phase content. Because NS is amorphous, the increase in amorphous material in nanocomposite samples is usually attributed to the additional NS loaded in the pastes at the nan fill capacity [38, 41]. Strong peaks at 2200 and 1800  $\text{cm}^{-1}$  are an Al-O-Si overlap and are interpreted asymmetric Si-O-Si tensile vibrations. It is widely known as the definitive peak and fingerprint of geopolymers (GBFS-based) [42] and the 4500 peak is due to the addition of NS, which is positioned 29 degrees. In XRD analysis, crystalline quartz is easily detected in the range  $2\theta=26-32$ . Which may be due to the formation of crystalline composition in the geopolymer matrix and it can be concluded that the strength of the sample (with NS) is

higher than (without NS) due to the presence of more crystalline composition in the geopolymer matrix. The intensity of quartz, molite and hematite is higher due to the presence of additional materials in the sample matrix containing NS. Some additional peaks in NS-modified GPC indicate the formation of new phases of quartz ( $\text{SiO}_2$ ), calcium carbonate, aluminum phosphate, compared to other samples, which confirms the presence of a crystalline phase in the geopolymer concrete. The chemical analysis of the GBFS-based GPC according to standard ASTM C989 [43] are provided in the following table.7 As shown in the XRF results in Table 6, By comparing GPC with ordinary concrete, In GPC the amount of  $\text{SiO}_2$  and  $\text{CaO}$  reduced by 38%, while the amount of  $\text{Na}_2\text{O}$  and  $\text{MgO}$  significantly increased. With the addition of 8% NS, the amount of  $\text{SiO}_2$  grew by 85%.

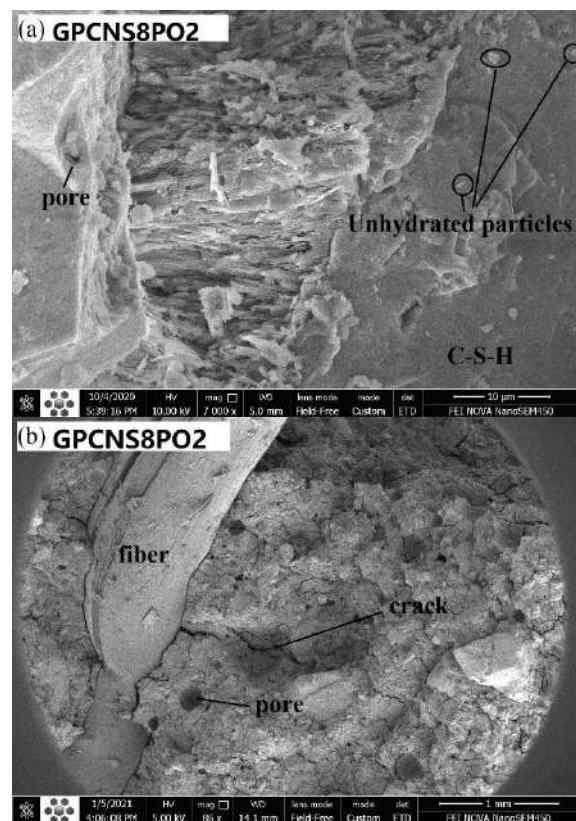


Fig. 7. Microstructure Image (SEM) of Geopolymer Concrete Reinforced with Polyolefin Fibers

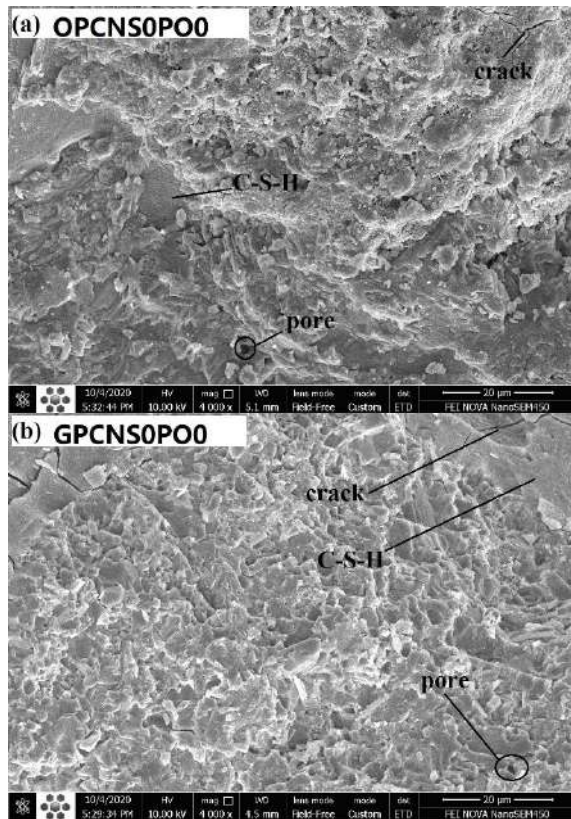


Fig. 8. Microstructure Image (SEM) of Geopolymer Concrete and Portland Cement Concrete

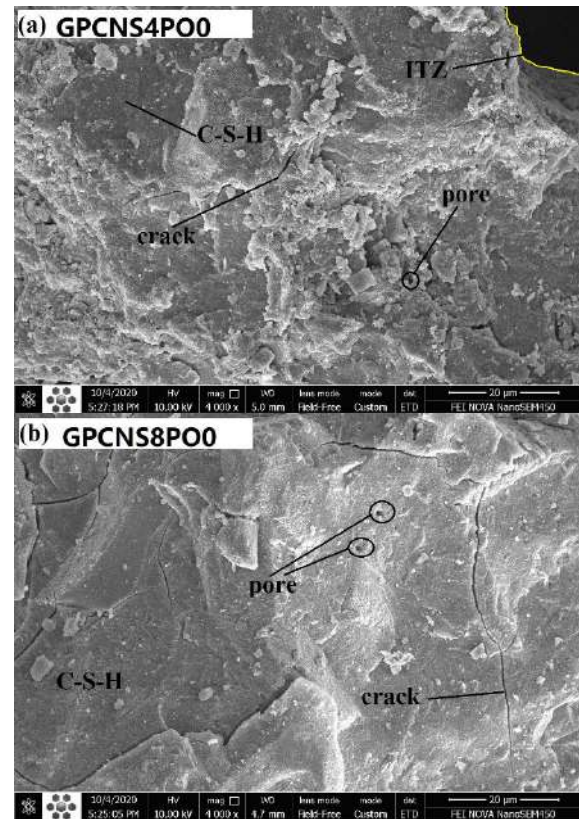


Fig. 9. Microstructure Image (SEM) of Geopolymer Concrete Containing NS

Table 7  
XRF Test Values for Samples

Mix ID	SiO <sub>2</sub>	Al <sub>2</sub> O <sub>3</sub>	CaO	MgO	K <sub>2</sub> O	Na <sub>2</sub> O	Fe <sub>2</sub> O <sub>3</sub>	LOI	TiO <sub>2</sub>	SO <sub>3</sub>
OPCNS0PO0	27.12	5.63	37.16	2.11	0.91	1.1	7.2	16.4	0.47	1.59
GPCNS0PO0	19.57	8.07	26.81	5.05	1.01	15.1	5.64	16.04	0.961	1.16
GPCNS4PO0	32.03	6.72	23.61	4.01	1.02	9.02	3.94	15.9	1.09	1.87
GPCNS8PO0	36.33	7.01	15.2	3.01	1.05	12.87	3.94	15.7	1.17	2.8



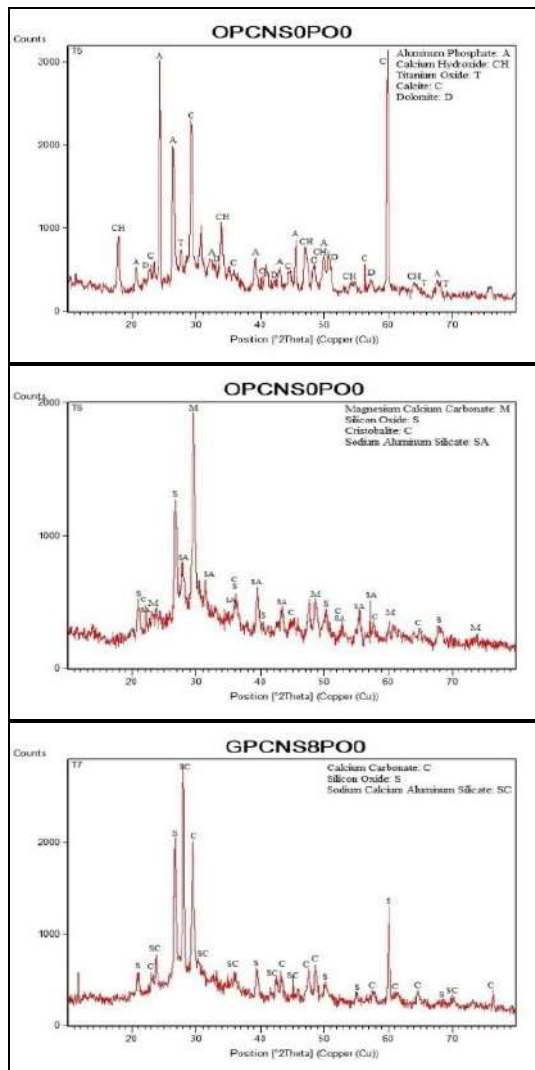


Fig. 10. XRD Patterns for Various Specimens

## 5. Conclusions

This study has evaluated the mechanical and microstructural properties of GBFS-based GPC containing POFs (0 to 2%) and NS (0 to 8%). The obtained results revealed that the addition of NS improved the mechanical and microstructural properties of the concrete. Furthermore, adding POFs remarkably affected the tensile strength and impact resistance.

1. The addition of NS to the GBFS-based GPC increased the compressive strength by 20% from 68

MPa to 82 MPa. The addition of fibers reduced the compressive strength of the specimens.

2. The fibers also improved the tensile strength due to the role of fibers in connection the cracks, brittle rupture and crushing of the specimen are prevented. It was found that the addition of NS increased the tensile strength by 11% to 15%.

3. The elastic modulus tests revealed that the elastic modulus increased by adding fibers and NS and replacing the ordinary concrete with GPC.

4. The impact resistance results indicated the marked effect of POFs on the number of impacts required for the creation of the first crack and full failure, increasing them by 13-30% and 213-345%, respectively. It was also found that the addition of NS increased the absorbed energy by 62% to 77%.

5. The results of the UPV tests indicated the excellent quality of all specimens at the ages of 28 and 90 days. Filling the pores and integrating the concrete, NS increased the velocity of the passing pulses.

6. The results of SEM, XRD and XRF tests were in coordination with the results of all tests performed in this study and well demonstrated the filling of the pores by the nanoparticles and densification of the concrete.

## References

- [1] Siddique, R. and D. Kaur, *Properties of concrete containing ground granulated blast furnace slag (GGBFS) at elevated temperatures*. Journal of Advanced Research, 2012. 3(1): p. 45-51.
- [2] Yüksel, İ., R. Siddique, and Ö. Özkan, *Influence of high temperature on the properties of concretes made with industrial by-products as fine aggregate replacement*. Construction and building materials, 2011. 25(2): p. 967-972.
- [3] McNulty, E., *Geopolymers: an environmental alternative to carbon dioxide producing ordinary Portland cement*. Department of Chemistry, The Catholic University of America, 2009.
- [4] Aslani, F., *Thermal performance modeling of geopolymer concrete*. Journal of Materials in Civil Engineering, 2016. 28(1): p. 04015062.

- [5] Assaedi, H., et al., *Influence of nano silica particles on durability of flax fabric reinforced geopolymer composites*. Materials, 2019. 12(9): p. 1459.
- [6] Deb, P.S., P.K. Sarker, and S. Barbhuiya, *Effects of nano-silica on the strength development of geopolymer cured at room temperature*. Construction and building materials, 2015. 101: p. 675-683.
- [7] Adak, D., M. Sarkar, and S. Mandal, *Structural performance of nano-silica modified fly-ash based geopolymer concrete*. Construction and Building Materials, 2017. 135: p. 430-439.
- [8] Ekinci, E., et al., *The improvement of mechanical, physical and durability characteristics of volcanic tuff based geopolymer concrete by using nano silica, micro silica and Styrene-Butadiene Latex additives at different ratios*. Construction and Building Materials, 2019. 201: p. 257-267.
- [9] Yousefvand, M., Y. Sharifi, and S. Yousefvand, *An Analysis of the Shear Strength and Rupture Modulus of Polyolefin-Fiber Reinforced Concrete at Different Temperatures*. Journal of civil Engineering and Materials Application, 2019. 3(4): p. 238-254.
- [10] Rashad, A.M., *The effect of polypropylene, polyvinyl-alcohol, carbon and glass fibres on geopolymers properties*. Materials Science and Technology, 2019. 35(2): p. 127-146.
- [11] Chellapandian, M., A. Mani, and S.S. Prakash, *Effect of macro-synthetic structural fibers on the flexural behavior of concrete beams reinforced with different ratios of GFRP bars*. Composite Structures, 2020. 254: p. 112790.
- [12] Adhikary, S.K., et al., *Investigation on the mechanical properties and post-cracking behavior of polyolefin fiber reinforced concrete*. Fibers, 2019. 7(1): p. 8.
- [13] Noushini, A., A. Castel, and R.I. Gilbert, *Creep and shrinkage of synthetic fibre-reinforced geopolymer concrete*. Magazine of Concrete Research, 2019. 71(20): p. 1070-1082.
- [14] Noushini, A., et al., *Mechanical and flexural performance of synthetic fibre reinforced geopolymer concrete*. Construction and Building Materials, 2018. 186: p. 454-475.
- [15] Pilehvar, S., et al., *Physical and mechanical properties of fly ash and slag geopolymer concrete containing different types of micro-encapsulated phase change materials*. Construction and Building Materials, 2018. 173: p. 28-39.
- [16] EN, B., *Testing hardened concrete. Method of determination of compressive strength of concrete cubes*. BS EN 12390 Part, 2000. 3.
- [17] ASTM, C.-. *Standard Test Method for Splitting Tensile Strength of Cylindrical Concrete Specimens*.
- [18] ASTM C469 / C469M-14, *Standard Test Method for Static Modulus of Elasticity and Poisson's Ratio of Concrete in Compression*, ASTM International, West Conshohocken, PA, 2014.
- [19] Galan, A. *Estimate of concrete strength by ultrasonic pulse velocity and damping constant*. in *Journal Proceedings*. 1967.
- [20] 544-2R-89, A., *'Measurement of properties of fiber reinforced concrete'*. Reported by ACI Committee, 1999. 544.
- [21] Wang, K., S.P. Shah, and P. Phuaksuk, *Plastic shrinkage cracking in concrete materials-Influence of fly ash and fibers*. ACI Materials Journal, 2002. 99(5): p. 512-513.
- [22] Beigi, M.H., et al., *An experimental survey on combined effects of fibers and nanosilica on the mechanical, rheological, and durability properties of self-compacting concrete*. Materials & Design, 2013. 50: p. 1019-1029.
- [23] Deb, P.S., P.K. Sarker, and S. Barbhuiya, *Sorptivity and acid resistance of ambient-cured geopolymer mortars containing nano-silica*. Cement and Concrete Composites, 2016. 72: p. 235-245.
- [24] Law, D.W., et al., *Long term durability properties of class F fly ash geopolymer concrete*. Materials and Structures, 2015. 48(3): p. 721-731.
- [25] Bahadori, H. and P. Hosseini, *Reduction of cement consumption by the aid of silica nano-*

- particles (investigation on concrete properties). *Journal of Civil Engineering and Management*, 2012. 18(3): p. 416-425.
- [26] Bosiljkov, V.B., *SCC mixes with poorly graded aggregate and high volume of limestone filler*. *Cement and Concrete Research*, 2003. 33(9): p. 1279-1286.
- [27] 363, A.C. *State-of-the-art Report on High-strength Concrete (ACI 363R-84)*. 1984. American Concrete Institute.
- [28] Nath, P. and P.K. Sarker, *Flexural strength and elastic modulus of ambient-cured blended low-calcium fly ash geopolymer concrete*. *Construction and Building Materials*, 2017. 130: p. 22-31.
- [29] Diaz-Loya, E.I., E.N. Allouche, and S. Vaidya, *Mechanical properties of fly-ash-based geopolymer concrete*. *ACI materials journal*, 2011. 108(3): p. 300.
- [30] 363, A.C., *State of the art of high strength concrete*. American Concrete Institute, (1993).
- [31] Sumajouw, D., et al., *Fly ash-based geopolymer concrete: study of slender reinforced columns*. *Journal of materials science*, 2007. 42(9): p. 3124-3130.
- [32] IS 13311-1 ): Method of Non-destructive testing of concrete, Part 1: Ultrasonic pulse velocity [CED 2: Cement and Concrete], Delhi, India, 1992.
- [33] Sahmaran, M., A. Yurtseven, and I.O. Yaman, *Workability of hybrid fiber reinforced self-compacting concrete*. *Building and Environment*, 2005. 40(12): p. 1672-1677.
- [34] Whitehurst, E.A. *Sonoscope tests concrete structures*. in *Journal Proceedings*. 1951.
- [35] Kwan, W.H., et al., *Influence of the amount of recycled coarse aggregate in concrete design and durability properties*. *Construction and Building Materials*, 2012. 26(1): p. 565-573.
- [36] Ren, W., J. Xu, and E. Bai, *Strength and ultrasonic characteristics of alkali-activated fly ash-slag geopolymer concrete after exposure to elevated temperatures*. *Journal of Materials in Civil Engineering*, 2015. 28(2): p. 04015124.
- [37] Du, H., S. Du, and X. Liu, *Durability performances of concrete with nano-silica*. *Construction and building materials*, 2014. 73: p. 705-712.
- [38] Phoo-ngernkham, T., et al., *The effect of adding nano-SiO<sub>2</sub> and nano-Al<sub>2</sub>O<sub>3</sub> on properties of high calcium fly ash geopolymer cured at ambient temperature*. *Materials & Design*, 2014. 55: p. 58-65.
- [39] Supit, S.W.M. and F.U.A. Shaikh, *Durability properties of high volume fly ash concrete containing nano-silica*. *Materials and structures*, 2015. 48(8): p. 2431-2445.
- [40] Shih, J.-Y., T.-P. Chang, and T.-C. Hsiao, *Effect of nanosilica on characterization of Portland cement composite*. *Materials Science and Engineering: A*, 2006. 424(1-2): p. 266-274.
- [41] Nazari, A. and J.G. Sanjayan, *Hybrid effects of alumina and silica nanoparticles on water absorption of geopolymers: Application of Taguchi approach*. *Measurement*, 2015. 60: p. 240-246.
- [42] Phair, J. and J. Van Deventer, *Effect of the silicate activator pH on the microstructural characteristics of waste-based geopolymers*. *International Journal of Mineral Processing*, 2002. 66(1-4): p. 121-143.
- [43] C989/C989M-18a, A., *Standard specification for slag cement for use in concrete and mortars*. 2018, ASTM International West Conshohocken, PA.



## Three-dimensional simulation of granular materials by discrete element method (DEM) by considering the fracture effect of particles

Amir Mahboob<sup>a</sup>, Omid Hassanshahi<sup>b,c,\*</sup>, Ashkan Sarabi Tabrizi<sup>d</sup>

<sup>a</sup> Department of Civil, Water and Environmental Engineering, Shahid Beheshti University, Tehran, Iran

<sup>b</sup> Department of Civil engineering, University of Minho, Campus de Azurém, 4800-058, Guimarães, Portugal

<sup>c</sup> Institute for Sustainability and Innovation in Structural Engineering, University of Minho, 4800-058, Guimarães, Portugal

<sup>d</sup> Department of Civil Engineering, Science and Culture University, Tehran, Iran

**Journals-Researchers use only:** Received date: 2023.03.20; revised date: 2023.04.15; accepted date: 2023.04.20

---

### Abstract

Coarse-grained materials, such as sand and gravel, exhibit a significant dependence on particle failure rate, which greatly influences their engineering behavior. This research focuses on the three-dimensional modeling of grain material behavior using the discrete element method (DEM) with PFC3D software and FISH programming language. The specific objective is to model the particle breakage phenomenon and its impact on resistance behavior and deformation. To accurately represent the non-spherical shape of the particles, an interconnected sphere approach was employed. The modeling of grain failure was achieved by establishing a failure criterion that considers two critical conditions: the heterogeneity of contact forces and stress within the particle. The proposed model and criteria were validated through comparison with triaxial experimental results obtained from the Purulia dam gravel. The results demonstrate that the developed model successfully captures the essential aspects of particle failure and its influence on the behavior of the granular environment. The simulations accurately represent the resistance behavior and deformation characteristics observed in the triaxial experiments. This validates the effectiveness of the proposed model in simulating the significant effects of particle failure on the behavior of coarse-grained materials. The findings of this study contribute to a deeper understanding of the complex behavior of coarse-grained materials, particularly in terms of their response to particle failure. The developed DEM model, incorporating the particle breakage phenomenon, provides a valuable tool for accurately predicting and analyzing the behavior of granular materials in various engineering applications. © 2017 Journals-Researchers. All rights reserved. (DOI: <https://doi.org/10.52547/JCER.5.2.14>)

**Keywords:** discrete component method; fracture effect; three-dimensional simulation; granular materials.

---

\* Corresponding author. Tel.: +0-351913837461; e-mail: [omid.hasanshahi@civil.uminho.pt](mailto:omid.hasanshahi@civil.uminho.pt).



## 1. Introduction

Grain environments are composed of separate particles, these particles are independent of each other and affect each other only at the points of contact. The behavior of these materials is complex and several experiments are required to determine this behavior. The behavior of granular soils such as sand is affected by the applied stress on the complex. At high stresses, soil particles can become brittle. Fracture of particles and conversion of coarse particles into smaller particles causes changes in the granulation curve and as a result change in the technical properties of granular materials. This phenomenon occurs more in tall earthen structures such as gravel dams and breakwaters, especially in the lower layers, which under the weight of the upper layers experience greater stresses. With the development of rapid computing, numerical methods are becoming more widely used to model the behavior of aggregates [1, 2]. One of these methods, which is developing more and more today, is the separate components method [3, 4].

The discrete method is a numerical method developed by Kandal to analyze rock mechanics problems [5, 6]. This method was used in 1979 by Kandal and Strack to simulate the behavior of a set of granular particles [7]. By comparing the force obtained from the numerical method and the results of the experimental photovoltaic method, they showed that the discrete component method is a valid tool for basic studies of the behavior of grain assemblies. Research has shown that the discrete component method can simulate the actual and physical behavior of grain assemblies [4]. The discrete component (DEM) method uses simple contact rules at intergranular contact points to obtain complex set of material responses. This method tries to simulate its mechanical behavior without imposing a specific behavioral law on the material. It can also consider the effect of various factors (such as grain shape, grain size and grain strength, etc.) on the mechanical behavior of the soil under study. One of the most important phenomena whose effect on the behavior of grain materials has been proven by many researchers is the phenomenon of grain failure [8, 9, 10 and 11]. Fracture of grains reduces the volume of voids and as a result the shrinkage behavior of materials, reduces

shear strength and also reduces the hydraulic conductivity of materials [10, 12].

The failure rate of particles is affected by various factors. Zhou et al. [11], by studying the three-dimensional behavior of micro and macro aggregates under different stress paths, concluded that the failure rate is strongly related to all-round stress, deflection stress and stress path. There are two ways to consider the separate nature of soils. The first method is to modify models based on continuous environment mechanics by introducing additional rules that reflect soil microstructural changes, such as texture [12], or to improve existing structural rules based on micromechanical studies on soil [14]. The second method considers the soil directly as a set of separate materials and its macroscopic and microscopic responses are collected under load, numerically, analytically or experimentally. This method has been widely used by micromechanical researchers [15 to 22].

Lim and McDoll [23] presented a model for the behavior of ballast materials used under railways using the discrete component method and with PFC3D software under edometer pressure. Munjiza et al. [24] and Munjiza [25] proposed a hybrid finite element method for simulating grains with irregular shapes. We and colleagues [26, 27] used this method to simulate the fracture of gravel particles by simulating potential fracture surfaces with adhesive joint surface elements without thickness. One of the most important researches to model the particle fracture effect by the discrete method method is the simulation of the behavior of gravel materials and the particle fracture effect using a probabilistic fracture model. Using brittle two-dimensional clusters, Delvarsh et al. Simulated the behavior of gravel materials used in earthen dams, especially considering the effect of particle refraction on deformation, and the significant effect of particle fracture on dam deformation during dewatering as well as the potential impact. The conclusion of a hand-picked block layer upstream and downstream of the dam in improving the stability of the dam [28].

McDowell et al. investigated the fracture of three-dimensional sand grains using the discrete component method to investigate the effect of size on strength. They modeled an aggregate particle into a mass of interconnected spheres and randomly removed a

number of spheres to obtain the strength and joint distribution and cracks with the desired Weibull modulus. They concluded that in composite particles where the spheres are in a hexagonal arrangement, when zero to 25% of the spheres are removed from the mass, size has almost no effect on the strength of the composite particle [29]. Using PFC3D software, Cheng et al. simulated the fracture masses by the discrete method by considering the loading speed in the triaxial test along the path of different stresses [30].

In this work, the heterogeneity approach is subsequently validated using DEM simulations of a triaxial test of a particle sample. Averaged stresses and strains are calculated in the course of the simulations resulting in stress–strain curves. Thereby, the influence of some DEM parameters on the resulting stresses and strains are analyzed. Therefore, the elastic and plastic parameters are fitted to the stress–strain curves of the triaxial tests. The most significant contribution of this paper is that we developed a practical breakage modeling technique in the context of DEM, which has the potential to capture the complex physical behavior of breakable granular materials.

## 2. Model used for gravel materials

In order to simulate particle fracture in a model, we make the separate components of the particles that make up the particle set from composite particles [31]. A composite particle, called a cluster, consists of a number of connected spherical grains (spheres) that, after breaking the cluster, the spherical particles can be separated from the group of particles, thus simulating the breakdown and separation of particles. It becomes malleable in a composite particle. In the present simulation, three-dimensional composite particles made of spherical spheres of different sizes have been used to model the gravel grains and the possibility of modeling their fracture. We also use finer spheres attached to the clusters of the previous type to consider the angular shape of the gravel material after fracture. The connection of these tiny spheres to the larger spheres is such that the tiny spheres cannot be separated from their host spheres. The production of pebble blocks is such that first the items forming each pebble block (cluster) are produced together and the

relative position of the items forming each pebble cluster remains constant during the simulation, unless the satisfaction failure criterion in this case, the spheres forming the cluster are separated from each other, and in this way, the simulation of particle failure is performed in this method. In order to simulate failure and create this capability in PFC3D software [32, 33], the necessary subroutines in the FISH programming language (FISH) were added to the main coding software and added to it. For every 100 cycles of simulation, these subroutines are called and executed. In this way, all the gravel clusters are controlled in the defined failure criterion, and the items or sub-clusters that make up each cluster that meet the failure criterion are separated according to the failure pattern, and then the simulation they will act freely and independently. In order to prevent the occurrence of large forces during the failure of particles, during the production of a cluster, the particles do not overlap and also at the moment of failure of the cluster, in a few steps or zero particle velocity to reduce kinetic energy and unbalance the spheres by coding Properly done.

### 2.1. Arrangement of clusters

In this study, two groups of clusters have been used to simulate gravel blocks. The clusters of the first group have no peripheral spheres and the clusters of the second group have tiny peripheral spheres. The first group of pebble clusters consisting of 4, 5, 6 and 8 spheres in three directions x, y and z are shown in Figures 1 to 4, respectively. In the first group, there are clusters of 4 spheres, 2 types of spheres with radii of 0.75 and 0.5 cm (Figure 1), which are surrounded by a hypothetical sphere with a diameter of 3 cm (similar to - Construction of gravel block with a diameter of 3 cm).

For clusters of 5 spheres (Figure 2), all the spheres that make up the cluster are the same (approximately 1.16 cm in radius). The cluster is enclosed in a hypothetical sphere 5 cm in diameter (simulation of a 5 cm diameter gravel block). Also, for clusters consisting of 6 spheres, there is a type of sphere with equal radius (approximately 0.828 cm). The cluster is enclosed in a hypothetical sphere 4 cm in diameter (simulation of a 4 cm diameter gravel block).

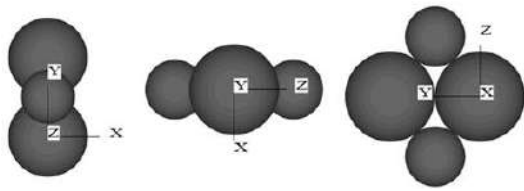


Figure 1: Cluster of the first group - the first type, consisting of 4 spheres.

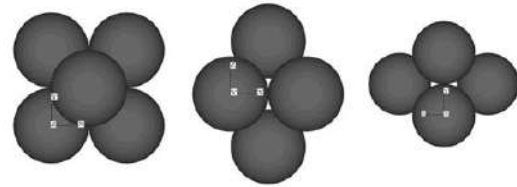


Figure 3: Cluster of the first group - the third type, consisting of 6 spheres.

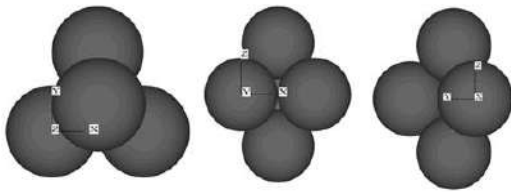


Figure 2: Cluster of the first group - the second type, consisting of 5 spheres.

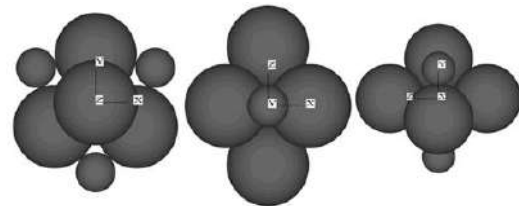


Figure 4: Cluster of the first group – the fourth type, consisting of 8 spheres.

Finally, for clusters of 8 spheres, there are two types of spheres. In order for the cluster to be enclosed inside a hypothetical sphere with a diameter of 6 cm (simulation of a pebble block with a diameter of 6 cm), the radii of the larger and smaller spheres are approximately equal to 1.39 and 0.9 cm, respectively. Also, for clusters consisting of 6 spheres, there is a type of sphere with equal radius (approximately 0.828 cm). The cluster is enclosed in a hypothetical sphere 4 cm in diameter (simulation of a 4 cm diameter gravel block).

Finally, for clusters of 8 spheres, there are two types of spheres. In order for a cluster to be enclosed within a hypothetical sphere 6 cm in diameter (simulation of a 6 cm diameter pebble block), the radii of the larger and smaller spheres are approximately equal to 1.39 and 0.39 cm, respectively.

The following clusters of the second group consisting of 4, 5, 6 and 8 spheres, in 3 directions x, y and z, are shown in Figures 5 to 8, respectively. As mentioned earlier, the clusters of the second group are similar to the clusters of the first group, except that they contain a number of tiny spheres whose radius is equal to one-eighth of the spheres attached to it in each cluster. There are two types of spheres, the corresponding sphere radius is considered (Figure 8).

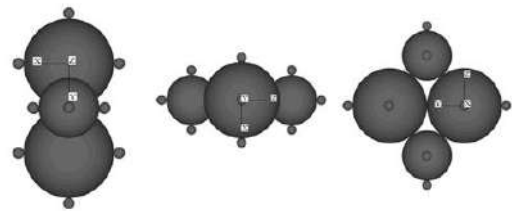


Figure 5: Cluster of the second group - the first type, consisting of 16 spheres.

A similar failure criterion has been used in previous studies [8, 34]. The blocks of the first group will be decomposed after breaking into their constituent spheres; The blocks of the second group, after failure, will be decomposed into their constituent clusters, which themselves contain several spheres. These sub-clusters can no longer be broken after the failure of the original cluster. The advantage of this type of cluster is that the particles left over from the fracture are angular, unlike the first group, where the particles from the fracture are completely round and spherical.

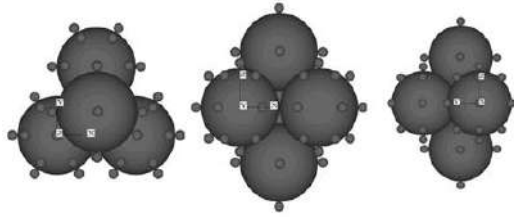


Figure 6: Cluster of the second group – the second type, consisting of 57 spheres.

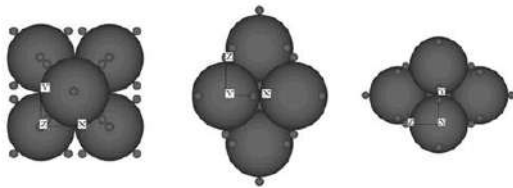


Figure 7: Cluster of the second group - the third type, consisting of 42 spheres.

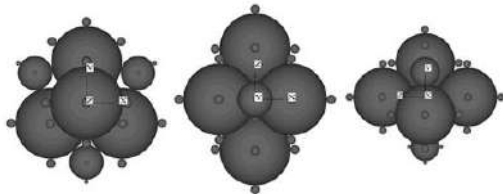


Figure 8: Cluster of the second group - the fourth type, consisting of 41 balls.

## 2.2. Failure criteria

In this study, in order to break a composite particle (cluster), it is necessary to fulfill two conditions simultaneously regarding the confinement of the cluster (inhomogeneity of the contact forces acting on a cluster) and the stress on the cluster:

The first condition: cluster confinement, in this research, the confinement failure condition related to confinement is measured using the contact force heterogeneity factor. If the coefficient of dissimilarity of the contact forces exceeds 0.25 (or in fact the confinement is less than a certain limit), one of the failure conditions is met.

The Second condition: the stress on the cluster is more than the defined failure resistance of each cluster.

## 2.3. Heterogeneity of contact forces for a cluster

For each cluster (pebble block), and for each angle  $\theta$ , the ratio of the algebraic sum of all the contact forces in the  $\theta$  direction to the total contact forces applied to that cluster is defined as the contact force orientation inequality. In order to enter the effect of contact force heterogeneity in the failure criterion, first condition is calculating the sum of contact forces for each cluster in the intervals  $\Delta\varphi$ ,  $\Delta\theta$  and  $\Delta\psi$  ( $\varphi$ ,  $\theta$  and  $\psi$  are the angles of each point of contact in a cluster with three coordinate axes).

In this study, for the simplicity of the failure criterion and the computational volume, the forces will be calculated for the intervals  $\Delta\theta=\Delta\varphi=\Delta\psi=20^\circ$ . This means that space is divided into three directions x, y and z in the range of  $20^\circ$  and each is assigned an identification number. For this purpose, all the space around each cluster is searched by writing three overlapping rings and examines all the contacts of a sphere forming a cluster and records the force applied based on the angle range inside it. This information is stored in a three-dimensional array that has 18 members in each dimension and is coded and added in the main software. This process is repeated for all contacts of other items in a cluster and then for all other clusters).

Then the largest element of this matrix is searched and it is represented by  $(f_\theta)_{\max}$ . The algebraic sum entered on a cluster is also calculated, which is denoted by  $\sum f_\theta$ . Finally, the heterogeneity factor of the spectator  $U_f$ , the correspondence of Equation (1) is calculated:

$$U_f = \frac{(f_\theta)_{\max}}{\sum f_\theta} \quad (1)$$

The value of  $U_f$  varies from zero to 0.5 (for point load testing).

#### 2.4. Tension created in a cluster

To introduce the second condition of failure (related to failure resistance), it is first necessary to determine the stress created in the cluster due to contact forces. The maximum tensile stress created in the stone blocks under indirect tensile test is calculated according to the following equation [35]:

$$\sigma = \frac{F}{\bar{d}^2} \quad (2)$$

Where:  $F$  is the force exerted on the rock by the test plates and  $\bar{d}$  is the distance between the test plates at the beginning of the test. Therefore, in the present model, assuming that the fracture mechanism of pebble blocks in a block set is similar to the fracture mechanism in the Brazilian experiment, the maximum tensile stress created in a cluster is calculated using the following equation:

$$\sigma_t = \frac{(f_\theta)_{\max}}{\bar{d}^2} \quad (3)$$

$(f_\theta)_{\max}$  is calculated as mentioned before in section 2.3.

#### 2.5. Fracture resistance

The fracture ability of gravel grains depends on the type of rock and its constituent minerals as well as the physical characteristics of the material such as size, shape and internal porosity of the grains. McDowell et al. [36] considered the concept of probability in the study of grain failure behavior. The probability of survival (non-breaking) of a grain ( $P_{sc}$ ) under  $\sigma_c$  stress applied in the failure test was defined as follows:

$$P_{sc} = (\sigma \geq \sigma_c) / t_n \quad (4)$$

Where,  $\sigma$  is the maximum stress created in the rock block in the indirect tensile test and  $t_n$  total number of test particles.

They also stated that Weibull distribution could model changes in the strength of granular materials. Studies have shown that the fracture toughness of granular materials follows Weibull's law [37]. In order to achieve a regular pattern for the distribution of strength of granular materials, they defined the

probability of survival of a grain under tensile stress as a function of the ratio  $\sigma / \sigma_0$  (normalized stress) [36]:

$$P_s = \exp [-(\sigma/\sigma_0)^m] \quad (5)$$

In this regard,  $P_s$  is the probability of survival of a grain under tensile stress and  $\sigma_0$  is the characteristic stress under which 37% of ( $\exp(-1)$ ) grains remain unscathed.  $m$  is the Weibull modulus that determines how the probability of survival changes with changes in stress and decreases with increasing resistance.

Marsal presented a study on the fracture toughness of stone blocks as the mean  $F_b$  resistance (mean fracture toughness obtained from three experiments performed on a fixed type of material) [9]. He then proposed a relation for obtaining  $F_b$  from the diameter of the stone block:

$$F_b = \eta (d/d_0)^\lambda \quad (6)$$

In this regard,  $F_b$  is in terms of kilograms and  $\eta$  and  $\lambda$  are characteristic of the material and  $d_0$  is the characteristic size. Marcel first assumed that the parameter  $\lambda$  for pebbles was equal to 1.5. His additional studies showed that this assumption was not far from reality and for different pebble materials tested, the  $\lambda$  parameter was obtained between 1.2-1.8. Subsequent studies showed that there is a direct relationship between the Weibull modulus and the  $\lambda$  parameter [28]:

$$\lambda = 2-(3/m) \quad (7)$$

Therefore, by placing 1.5 instead of the parameter  $\lambda$  in the above equation, the value 6 is obtained for the Weibull modulus of the gravel material.

Thus, by obtaining  $m$  for these gravel materials, the probability-based resistance distribution can be obtained. In this study, for conducting experiments and simulations, the pebble characteristics provided by Varadarajan et al. [38]. In the results of their experiments, they did not mention the distribution based on the probability of gravel resistance and used the concept of failure value (percentage change through sieve) to investigate grain failure. Therefore, according to the studies performed on stone blocks by Marsal and according to the type of stone materials tested by Varadajan et al., The appropriate failure resistance for this problem is extracted. Table 1 shows the specifications of different materials tested by Varadarajan et al. [38]. Thus, by having the material properties of  $\eta$  and  $\lambda$ , we can obtain  $F_b$  and according

Table 1.

Specifications of stone materials tested by Varadarajan et al. [38].

Specimen	Type of materials	$\lambda$	$\eta$ (N)	$F_b$ (N)	$d_{avg}$ (m)
Various stone materials tested by Marsal	Quartz	1/6	2218850	10900	0/04
	Diorite	1/2	351660	7030	0/042
	Basalt	1/4	883340	11400	0/043
	Granite	1/6	1315460	6030	0/04
Granular materials	Includes quartz, biotite and feldspar	1/5	1400000	11200	0/04

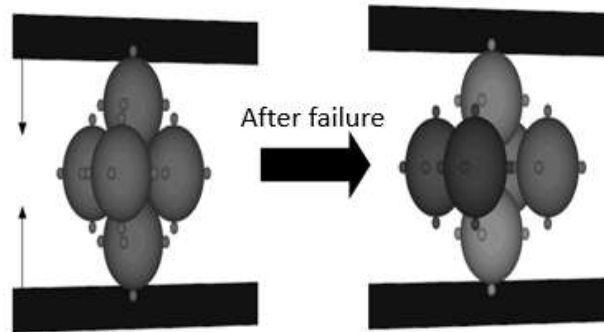


Figure 9. Indirect tensile test on the second group gravel block with 6 sub-clusters.

to equation (6), the resistance of the block with any diameter size.

In order to conform to the statistical distribution of Weibull with a modulus ( $m$ ) equal to 6, the possible coefficients of resistance changes on the characteristic resistance ( $\sigma_0$ ) have been applied. By extending Equation (5), the range of changes of the  $\sigma/\sigma_0$  ratio from 0.0465 (for 99% survival probability) to 1.29 (for 1% survival probability) is obtained. Considering the fracture toughness ( $\sigma_{max}$ ) equal to  $\sigma_0$ , the characteristic stress of the desired distribution ( $\sigma_0$ ) will be equal to ( $\sigma_{max}$ ) and the range of changes of the maximum tolerable stress of materials ( $\sigma_{max}$ ) in the range ( $0.465\sigma_0$ - $1.29\sigma_0$ ) is obtained. PFC<sup>3D</sup> software does not have the ability to generate such a distribution directly, so a suitable subroutine was added to the software.

### 3. Numerical failure tests on gravel blocks

In total, two types of indirect tensile numerical tests and triaxial tests have been simulated on samples made of different types of gravel blocks in different conditions. First, to extract the probability distribution of survival and validation of the failure model, the indirect tensile numerical test is simulated on the types of gravel blocks produced. In the following, various triaxial experiments have been performed and validated.

#### 3.1. Fracture resistance

To extract the survival probability distribution of the modeled clusters, the clusters of the second group with 6 sub-clusters and 30 pebble blocks with the same diameter (4.4 cm) between two rigid walls, under

controlled strain conditions, were tested and experienced failure (Figure 9). The clusters produced in the second group are already shown in Figures (5) to (8). In this test, the walls approach each other at a uniform speed, and as mentioned in Section 2, the gravel block is checked once every 100 cycles for failure. If the failure criterion is true, the sub-clusters that make up the cluster will be separated. An example of a stress diagram applied to a cluster versus computational cycles is given in Figure 10. The declared stresses, using Equation (6) for the cluster are of unit thickness. The normal and tangential stiffnesses of the disks are equal to  $1.5 \times 10^8$  N/m and the internal coefficient of friction is 0.7.

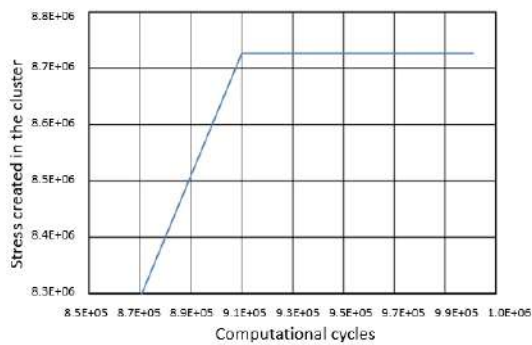


Figure 10: Stress created in the cluster (in Pa) against computational cycles.

Due to the scattering applied to the strength of the blocks, different maximum stresses were obtained from these experiments. Figure 11 shows the probability survival curve for Weibull distribution as well as the results of uniaxial experiments. In this form, the agreement between the numerical results and the Weibull distribution is clear.

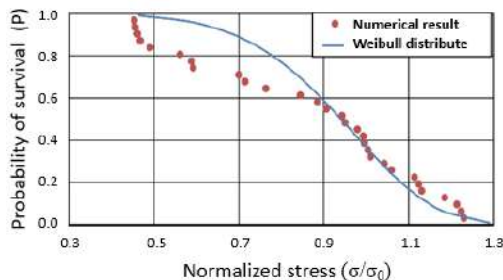


Figure 11. Probability of survival curve against normalized stress  $\sigma/\sigma_0$ .

After the experiments, a value of 8.389 MPa was obtained for  $\sigma_0$ , which, as mentioned, can be considered as the fracture toughness of the material. Therefore, the fracture toughness of materials with a diameter of 4.4 cm is 389.8 MPa. This value is obtained according to the simulation performed; In the real case, considering the relations (2) and (6) and holding the diameter of the block, the real resistance can be obtained. This value is 6.67 MPa for a block with a diameter of 0.044 m, which indicates a good agreement between the actual results and the simulation. Equation (5) can be rewritten as follows, and used to determine the Weibull modulus.

$$\ln(\ln(1/P_s)) = m \times \ln(\sigma/\sigma_0) \quad (8)$$

#### 4. Triaxial tests

In the present study, in order to validate the model, triaxial experiments performed by Varadarajan et al. On the pebble materials of Prolia Dam have been considered [37].

In Figure 12, both the Weibull distribution results and the numerical results give approximately the same value of  $m$ . In this figure, the slope of the curve, according to Equation 7 and the coordinate axes, is  $m$ .

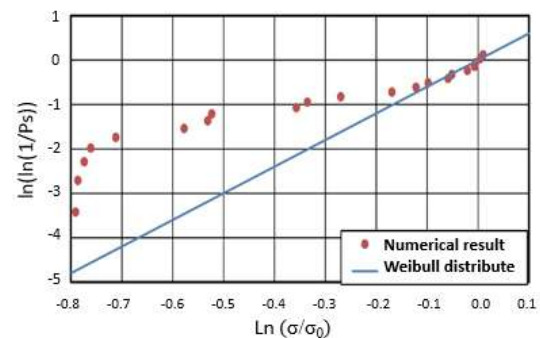


Figure 12. Modulus  $m$ , for Weibull distribution and performed tests.

##### 4.1. How to perform triaxial experiments on the sample of gravel blocks

To simulate the triaxial experiment, a set of pebble blocks within six walls are considered as boundary

Table 2.

Sample characteristics in triaxial numerical simulations

Composition of clusters	Group type	Cluster diameter (cm)	Number of modeled spheres	Number of modeled clusters	Vertical and shear stiffness (N/m)	Density	Coefficient of wall friction with particles	Coefficient of friction between particles	Vacuum sign
First group	First	3	10900	2100	$1 \times 10^8$	2680	0/7	0/25	0/66
	Second	5							
	Third	4							
	Fourth	6							
Second group	First	3.27	31316	1100	$1 \times 10^8$	2680	0/7	0/25	0/7
	Second	5.58							
	Third	4.4							
	Fourth	6.7							

elements to apply boundary conditions. Horizontal walls are used as rigid plates to introduce vertical force and vertical walls are used to apply all-round stress. The normal and tangential stiffnesses of horizontal walls are equal to the stiffness of the clusters, but the stiffness of the vertical walls relative to 0.1 stiffness of the clusters is considered to simulate the conditions of soft confinement [30]. Dumping was equal to 0.7 (software default) and time step was  $2E-6$ .

To prepare the test sample, a precipitation process was used to prevent distortion of the initial conditions of the sample. In general, triaxial experiments consist of three stages:

1. The first stage of making a sample with the desired porosity (which includes the process of falling clusters and moving the walls together).
2. The second stage of applying all-inclusive tension to the desired tension.
3. The third stage is the application of deviant stress with constant all-round stress.

It should be noted that in the first stage (sample making) the clusters are not allowed to fail, but in the second and third stages this is possible and the clusters are examined during the process specified in the failure criterion.

In the deflection stress application stage for cutting, the upper and lower horizontal walls of the specimen approach each other at a predetermined speed. This speed is low in the early stages and then increases in the later stages to reach the final speed (0.04 m/s).

The number of these steps is 80; in the first stage, the speed of the walls is 1.80, the final speed, at the

end of the stage it reaches our final speed. Table 2 shows the specifications of the simulations.

#### 4.2. Sample preparation steps

First, six walls were built at regular intervals to form a rectangular cube with dimensions of  $2.6 \times 1.1 \times 1.1$  meters, as shown in Figure 13. In this space, 2100 spheres with a varying radius of 3 to 6 cm are created at random, followed by 200 octagonal clusters (containing eight spheres), 500 5clusters, 600 6clusters, and 800 4clusters. Some of the original pieces are replaced (Figure 13-a). Then, by applying gravity to the bottom of the sample (negative acceleration) and by applying several cycles, the particles are precipitated. In this way, the sample is prepared for compaction to the desired porosity (Figure 13-b). Finally, we bring the walls closer together at a suitable speed to achieve the desired minimum porosity ratio (shown in Table 2) (Figure 13-c). For the clusters of the second group, we repeat exactly the same procedure to make a sample of particles with more angularity.

The final dimensions of the sample are  $0.28 \times 0.48 \times 0.28$  that the ratio of the smallest dimension of the sample to the size of the largest aggregate for the sample of the first and second groups is 4.76 and 4.17, respectively.



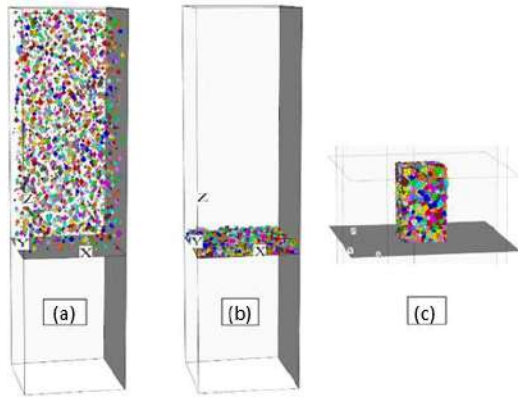


Figure 13. Sample preparation steps. a) Production of clusters b) Sedimentation of clusters, c) Movement of walls and compaction.

#### 4.3. Applying all-round tension and deviant tension

Three-axis experiments are performed at various all-round pressures. To keep the overall stresses constant during the test, a lateral stress control mechanism was added to the software by coding. In this way, first the walls are approached to reach the desired stress, then by considering a small tolerance (for example,  $\pm 0.005$  Pascal) the existing stress is compared with the all-round stress of the target and based on that the speed of the side walls is adjusted. Turns.

In PFC<sup>3D</sup> software, we use movement and acceleration to the walls to load the sample (apply stress). In the deflection stress stage, the upper and lower walls of the specimen approach each other at a predetermined speed. This speed is low in the early stages and then increases in the later stages to reach the final speed (0.04 m/s). The number of these steps is 80; in the first stage, the speed of the walls is 1.80, and at the end of the stage, it reaches the final speed.

As mentioned, from the beginning of the all-inclusive stress phase to the end of the triaxial test, the clusters have the possibility of failure, although in the all-inclusive stress phase, only a small percentage of the clusters fail.

#### 4.4. Triaxial tests' results

The results of triaxial experiments for the two groups of clusters and for all-round pressures of 0.3, 0.7 and 1 MPa are given, and finally the results of the two are compared. Figure 14 shows the failure rates of the clusters during the triaxial cutting section for all experiments.

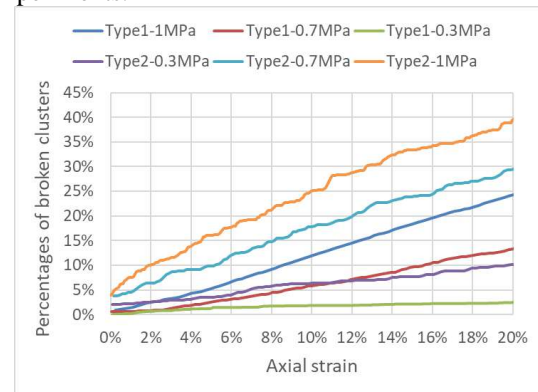


Figure 14. Percentages of broken clusters against axial strain (Clusters of the first and second groups, lateral stresses of 0.3 to 1 MPa).

The results show that the angularity of most of the simulated gravel blocks increases the failure slope of the clusters and its final percentage in strain by 20%, so that this trend for the second group cluster with all-round stress of 0.3 MPa is relatively similar to the first group cluster but with all-round stress is 0.7 MPa. For higher stresses (0.7 and 1 MPa) this difference is greater and the failure of the second group of clusters (sharp angle) is steeper. Table 3 shows the failure rate of clusters at 20% strain.

Table 3.

Percentage of cluster failure at 20% strain

Failure rate of clusters (%)			
First group	Second group	All-round stress (kPa)	Failure rate (%)
4.64	18.10	300	119.4
14.29	30	700	109.9
25.57	40.18	1000	57.1

#### 4.4.1 Comparison of stress and strain diagrams for each cluster group

Figures 15 to 18 show the diagrams of the deflection stress versus strain and volumetric behavior of the specimens during the triaxial test in all three all-round stresses for both groups of clusters, respectively.

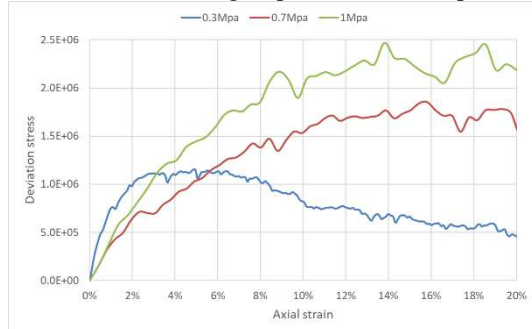


Figure 15. Deviation stress versus axial strain (first group cluster, all-inclusive stress of 0.3, 0.7 and 1 MPa).

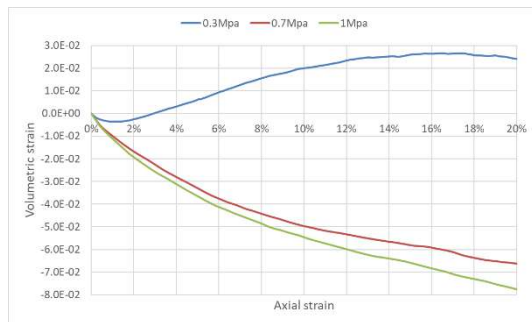


Figure 16. Volumetric strain of the first group cluster in all-round stress of 0.3, 0.7 and 1 MPa.

As mentioned earlier, for the clusters of the first group, in the all-round stress of 0.3 MPa, the sample behavior is different and has a peak, has a higher initial stiffness, but the amount of deflection stress in the strain is 20% less. There is also a difference between volumetric and axial strain behavior. According to Figure (16), only the sample under 0.3 all-inclusive stress showed diphtheria behavior, while the behavior of 0.7 and 1 MPa all-inclusive stress samples is completely contractile and decreases in volume.

The behavior is different for the clusters of the second group as shown in Figure (17). The sample from the all-inclusive stress of 0.3 MPa to 0.7 MPa experienced more deviation stress at constant strain,

while the behavior of the samples with the all-inclusive stress of 0.7 and 1 MPa did not differ as much. In addition, as shown in Figure (18), the greater the overall stress, the higher the contractile behavior of the specimens.

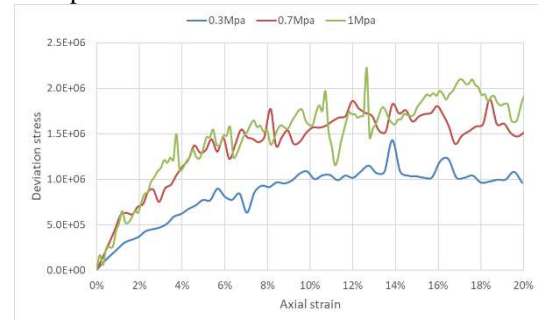


Figure 17. Deviation stress versus axial strain (second group cluster in all-round stress of 0.3, 0.7 and 1 MPa).

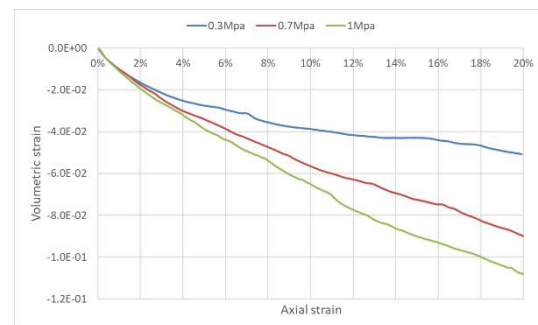


Figure 18. Volumetric strain versus axial strain (second group cluster in all-round stress of 0.3, 0.7 and 1 MPa).

#### 4.4.2 Comparison of stress and strain diagrams for each all-round stress

In this section, the behavior of the samples at different all-round stresses for the two groups of clusters is presented separately to determine more precisely the effect of roundness or sharpness of the gravel blocks. In the 0.3 MPa all-round stress, the round specimen (first group) has a peak, while the sharp specimen (second group) has a fixed concavity direction with a certain amount of stress (Figure 19).

Also, the round specimen (first group) has a contractile and dilated behavior, while the sharp specimen (second group) is completely contractile (Figure 20), which is a function of the greater failure

of the second group of gravel particles. Fracture of the pebble and production of smaller particles causes more contractile behavior.

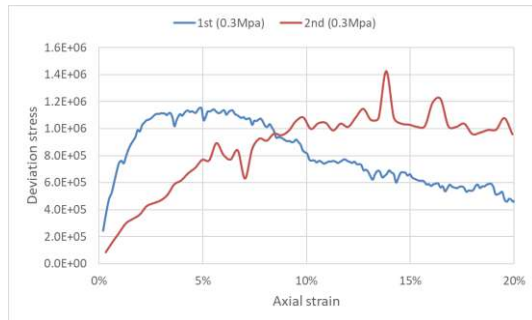


Figure 19. Deviation stress versus axial strain (first and second group clusters, all-round stress 0.3 MPa).

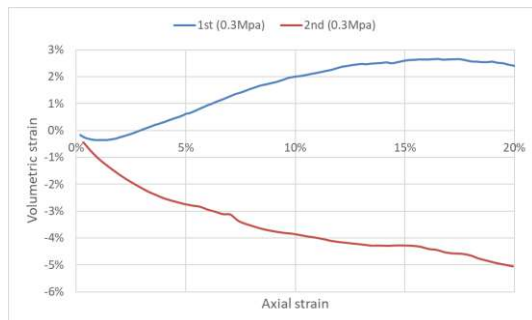


Figure 20. Axial strain versus volumetric strain (first and second group clusters, all-round stress 0.3 MPa).

At an all-round stress of 0.7 MPa, the sharp-edged specimen (second group), compared to the first group, initially establishes greater amounts of stress per strain and then almost coincides and behaves in a similar manner (see Figure 21).

Also, both round (first group) and sharp (second group) specimens have contractile behavior, which is more for the sharp corner (second group), see Figure 22.

In the 1MP all-round stress, first the diagrams of the two samples are almost identical and then the round sample (first group) shows higher values of stress per strain (Figure 23). Also, as in the experiment with all-round stress of 0.7 MPa, both specimens of round (first group) and sharp (second group) have contractile behavior, which is higher for sharp specimens (Figure 24).

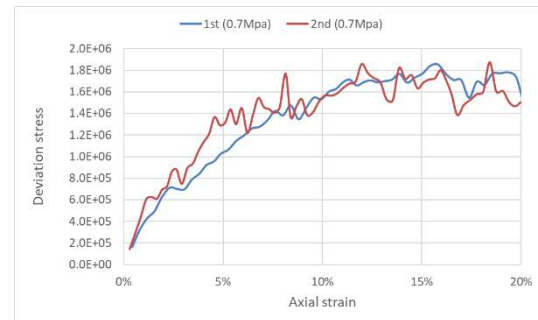


Figure 21. Deviation stress versus axial strain (first and second group clusters, all-round stress 0.7 MPa).

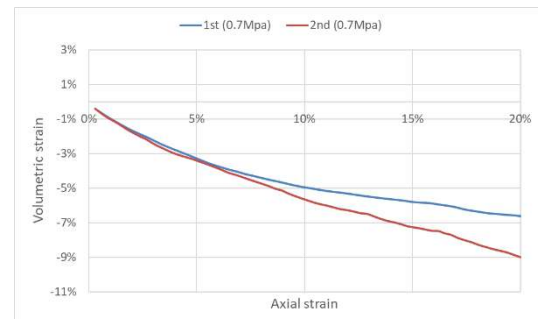


Figure 22. Axial strain versus volumetric strain (first and second group clusters, all-round stress equal to 0.7 MPa).

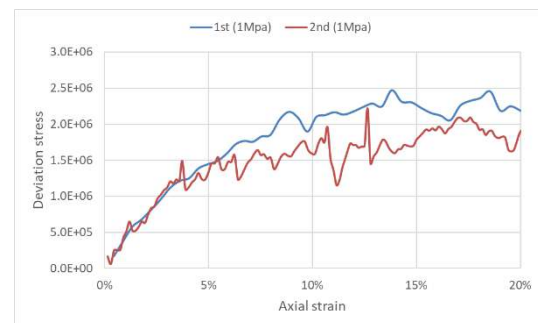


Figure 23. Deviation stress versus axial strain (clusters of the first and second groups, all-inclusive stress of 1 MPa).

#### 4.5. Granulation change due to particle failure

The granulation curves for the samples at the end of the isotropic density and the end of the experiment are shown in Figure 25. It can be seen that with increasing lateral stress, the failure in the sample increases and the changes in the grain size curve

increase. Also, with increasing particle angulation (cluster of the second group), the failure has increased and the grain size of the sample has become finer.

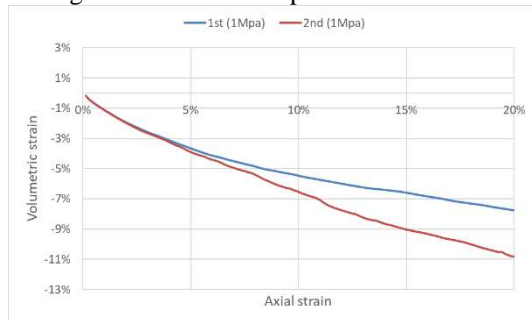


Figure 24. Axial strain versus volumetric strain (clusters of the first and second groups, all-inclusive stress of 1 MPa).

#### 4.5. Granulation change due to particle failure

The granulation curves for the samples at the end of the isotropic density and the end of the experiment are shown in Figure 25. It can be seen that with increasing lateral stress, the failure in the sample increases and the changes in the grain size curve increase. Also, with increasing particle angulation (cluster of the second group), the failure has increased and the grain size of the sample has become finer.

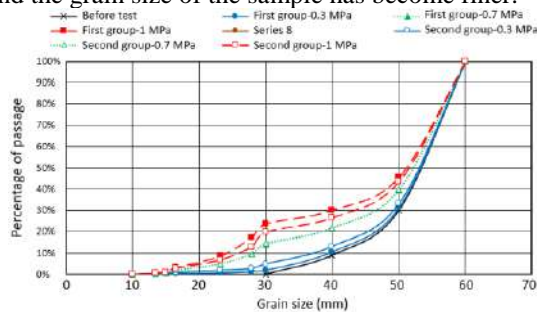


Figure 25. Grading curves of materials before and after testing.

#### 4.6. Comparison of simulation results with experimental results

The results of the experiments performed in Section (4.4) together with the data obtained from large-scale triaxial experimental experiments on dam materials (Sample B) [38] in Figures 26 and 27 and also in Table 4 are given.

Figure 26 Comparison of stress and axial strain results of simulated experiments (for the first group cluster) and reported results for experimental experiments [38] with all-round stresses of 0.3 and 0.9 MPa and also Figure 27 Volumetric strain results against axial strain for the same experiments.

In order to save time and number of simulations, three all-round pressures of 0.3, 0.7 and 1 MPa have been used for the simulations. The experimental experiments were performed in four all-round stresses of 0.3, 0.6, 0.9 and 1.2 MPa. The simulated experiments are in the middle of the experimental experiments. Due to the limitations of simulation, the initial porosity of the samples is different, so the volumetric strain of the simulated results and experimental experiments are not comparable. It should be noted that it was not possible to achieve low porosity in the three-dimensional preparation of the sample.

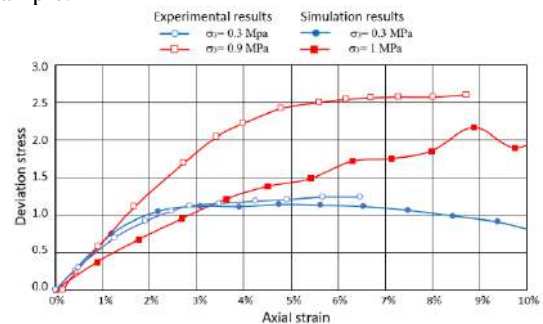


Figure 26. Comparison of axial strain versus deviation stress results for simulated samples and experimental results [38].

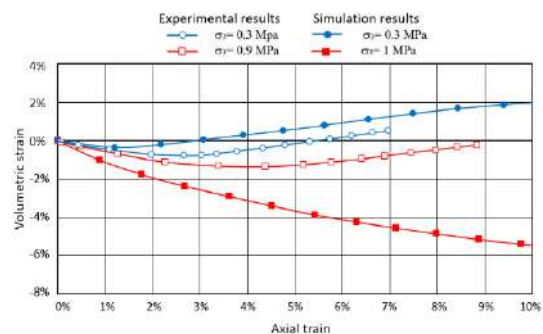


Figure 27: Comparison of axial strain versus volumetric strain results for simulated samples and experimental results [38].

Examination and comparison of the results show that the results in all-round stress of 0.3 MPa are quite

satisfactory, but with increasing all-round stress and increasing particle breakage in the numerical sample and due to the production of completely spherical particles resulting from composite particle failure, the numerical sample increases. It shows less resistance and has a more compact behavior in terms of volume.

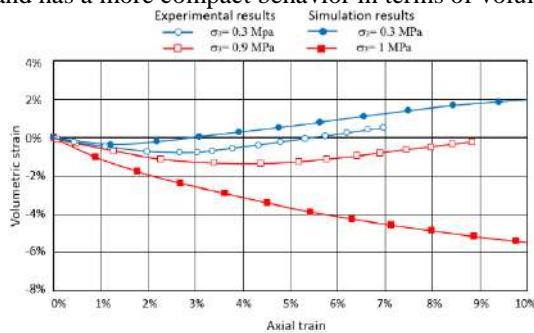


Figure 27: Comparison of axial strain versus volumetric strain results for simulated samples and experimental results [38].

Table 4.

Comparison of experimental and numerical results.

Simulation results		Experimental results	All-round stress
First group clusters	Second group clusters		
$\phi^0$ in rupture	$\phi^0$ in rupture		
41	40	43	0.3
35	33	38	0.7
28	34	36	1

Comparison of the values in Table (4) shows the high accuracy and consistency of the numerical simulation and the criteria presented with the experimental experiments. The decrease in  $\phi$  for the second group clusters is greater than the first group due to the failure that occurred in the sample.

## 5. Conclusions

In this research, the behavior of gravel materials and the phenomenon of particle fracture have been simulated and validated using a discrete component method and an efficient model. As is clear from the output of the numerical tests:

1. Increasing the all-round pressure and increasing the sharpness of the gravel blocks has increased the grain failure during cutting to the sample. Particle

breakage causes the specimens to show mostly no dilatation behavior and to act completely contractile.

2. The stress-strain behavior changes from dense (with peak) to the process of a loose sample, which all proves the high impact of the failure phenomenon on the sample behavior. The present study demonstrates the ability of the discrete component (DEM) method to consider the complex behavior of gravel materials.

3. The results obtained for simulating a real gravel show that the internal friction angle of the materials is simulated with good accuracy.

4. The following are the important characteristics and strengths of this model to simulate the behavior of gravel materials:

a) The proposed rupture criterion takes into account the resistance parameters as well as the confinement (heterogeneity of contact forces).

b) The concept of probability for the strength of blocks is included in the rupture criterion.

c) The three-dimensional model makes the results more accurate and the model more efficient.

## References

- [1] Salles, A., Salati, M. and Bragança, L., 2023. Analyzing the Feasibility of Integrating Urban Sustainability Assessment Indicators with City Information Modelling (CIM). *Applied System Innovation*, 6(2), p.45.
- [2] Abedi, M., Hassanshahi, O., Rashidell, A., Ashtari, H., Meddah, M.S., Dias, D., Arjomand, M.A. and Choong, K.K., 2023. A sustainable cementitious composite reinforced with natural fibers: An experimental and numerical study. *Construction and Building Materials*, 378, p.131093.
- [3] Oh, C.L., Choong, K.K., Nishimura, T., Kim, J.Y. and Hassanshahi, O., 2019. Shape change analysis of tensegrity models. *Latin American Journal of Solids and Structures*, 16.
- [4] O'Sullivan, C. (2011). Particle-based discrete element modeling: geomechanics perspective. *International Journal of Geomechanics*, 11(6), 449-464.
- [5] Cundall, P. A. (1971). A computer model for simulating progressive large scale movements in blocky system. In *Proc. Int. Symp. on Rock Fractures*. (pp. II-8).
- [6] Candall, P. A. (1974). A Computer model for rock-mass behavior using interactive graphics for the input and output of geometrical data. Report MDR-2-74.
- [7] Cundall, P. A., & Strack, O. D. (1979). A discrete numerical model for granular assemblies. *geotechnique*, 29(1), 47-65.
- [8] Mahboob, A., Hassanshahi, O., Hakimi, A., & Safi, M. (2023). Evaluating the Performance of Hollow Core Slabs (HCS)-Concrete and Simplifying Their Implementation. *Recent Progress in Materials*, 5(2), 1-15.



- [9] AtashBahar, M., Chenari, R. J., & e Neshaei, M. A. L. Evaluation of the Behavior of Rockfill Material Using Large-Scale Triaxial Tests.
- [10] Salati, M., Bragança, L. and Mateus, R., 2022. Sustainability Assessment on an Urban Scale: Context, Challenges, and Most Relevant Indicators. *Applied System Innovation*, 5(2), p.41.
- [11] Lade, P. V., Yamamuro, J. A., & Bopp, P. A. (1996). Significance of particle crushing in granular materials. *Journal of Geotechnical Engineering*, 122(4), 309-316.
- [12] Yousefi, A., Bunnori, N.M., Khavarian, M., Hassanshahi, O. and Majid, T.A., 2017, October. Experimental investigation on effect of multi-walled carbon nanotubes concentration on flexural properties and microstructure of cement mortar composite. In *AIP Conference Proceedings* (Vol. 1892, No. 1, p. 020032). AIP Publishing LLC.
- [13] Xu, M., Hong, J., & Song, E. (2017). DEM study on the effect of particle breakage on the macro-and micro-behavior of rockfill sheared along different stress paths. *Computers and Geotechnics*, 89, 113-127.
- [14] Wan, R. G., & Guo, P. J. (2004). Stress dilatancy and fabric dependencies on sand behavior. *Journal of Engineering Mechanics*, 130(6), 635-645.
- [15] Zhujiang, S. (1999). A granular medium model for liquefaction analysis of sands. *CHINESE JOURNAL OF GEOTECHNICAL ENGINEERING-CHINESE EDITION-*, 21(6), 742-748.
- [16] Abedi, M., Hassanshahi, O., Barros, J.A., Correia, A.G. and Figueiro, R., 2022. Three-dimensional braided composites as innovative smart structural reinforcements. *Composite Structures*, 297, p.115912.
- [17] Chang, C. S., & Liao, C. L. (1990). Constitutive relation for a particulate medium with the effect of particle rotation. *International Journal of Solids and Structures*, 26(4), 437-453.
- [18] Chang, C. S., & Ma, L. (1991). A micromechanical-based micropolar theory for deformation of granular solids. *International Journal of Solids and Structures*, 28(1), 67-86.
- [19] Hassanshahi, O., Majid, T.A., Lau, T.L., Yousefi, A. and Tahara, R.M.K., 2017, October. Seismic performance of the typical RC beam-column joint subjected to repeated earthquakes. In *AIP Conference Proceedings* (Vol. 1892, No. 1, p. 120014). AIP Publishing LLC.
- [20] Oda, M., Konishi, J., & Nemat-Nasser, S. (1982). Experimental micromechanical evaluation of strength of granular materials: effects of particle rolling. *Mechanics of materials*, 1(4), 269-283.
- [21] Chang, C. S., & Liao, C. L. (1990). Constitutive relation for a particulate medium with the effect of particle rotation. *International Journal of Solids and Structures*, 26(4), 437-453.
- [22] Chang, C. S., & Ma, L. (1991). A micromechanical-based micropolar theory for deformation of granular solids. *International Journal of Solids and Structures*, 28(1), 67-86.
- [23] Lim, W. L., & McDowell, G. R. (2005). Discrete element modelling of railway ballast. *Granular Matter*, 7, 19-29.
- [24] Munjiza, A., Owen, D. R. J., & Bicanic, N. (1995). A combined finite-discrete element method in transient dynamics of fracturing solids. *Engineering computations*.
- [25] Munjiza, A. A. (2004). The combined finite-discrete element method. John Wiley & Sons.
- [26] Ma, G., Zhou, W., & Chang, X. L. (2014). Modeling the particle breakage of rockfill materials with the cohesive crack model. *Computers and Geotechnics*, 61, 132-143.
- [27] Ma, G., Zhou, W., Chang, X. L., & Chen, M. X. (2016). A hybrid approach for modeling of breakable granular materials using combined finite-discrete element method. *Granular Matter*, 18, 1-17.
- [28] Deluzarche, R., & Cambou, B. (2006). Discrete numerical modelling of rockfill dams. *International journal for numerical and analytical methods in geomechanics*, 30(11), 1075-1096.
- [29] McDowell, G. R., & Harireche, O. (2002). Discrete element modelling of soil particle fracture. *Géotechnique*, 52(2), 131-135.
- [30] Cheng, Y. P., Nakata, Y., & Bolton, M. D. (2003). Discrete element simulation of crushable soil. *Geotechnique*, 53(7), 633-641.
- [31] Mahboob, A., Eskenati, A. R., & Moradalizadeh, S. (2021). Numerical Investigation and Cost Analysis of FRP-Concrete Unidirectional Hybrid Slabs. *International Journal of Applied Mechanics and Engineering*, 26(4), 156-166.
- [32] Itasca, C. G. I. (2005). PFC3D (Particle Flow Code in Three Dimensions). Minneapolis, Minnesota, USA.
- [33] Peen, W.Y., Keong, C.K. and Hassanshahi, O., 2019. Behaviour of hollow circular section with multiple perforations under compression, flexure and torsion. *Latin American Journal of Solids and Structures*, 16.
- [34] Abedi, M., Sanivada, U.K., Mirian, S.A., Hassanshahi, O., Al-Jabri, K., Correia, A.G., Lourenço, P.B. and Figueiro, R., 2023. A self-sensing and self-heating planar braided composite for smart civil infrastructures reinforcement. *Construction and Building Materials*, 387, p.131617.
- [35] Jaeger, J. C. (1967, April). Failure of rocks under tensile conditions. In *International Journal of Rock Mechanics and Mining Sciences & Geomechanics Abstracts* (Vol. 4, No. 2, pp. 219-227). Pergamon.
- [36] McDowell, G. R., Bolton, M. D., & Robertson, D. (1996). The fractal crushing of granular materials. *Journal of the Mechanics and Physics of Solids*, 44(12), 2079-2101.
- [37] Weibull, W. (1951). A statistical distribution function of wide applicability. *Journal of applied mechanics*.
- [38] Varadarajan, A., Sharma, K. G., Venkatachalam, K., & Gupta, A. K. (2003). Testing and modeling two rockfill materials. *Journal of geotechnical and geoenvironmental engineering*, 129(3), 206-218.
- [39] P. Audebert, P. Hapiot, J. Electroanal. Chem. 361 (1993) 177.
- [40] J. Newman, *Electrochemical Systems*, 2nd ed., Prentice-Hall, Englewood Cliffs, NJ, 1991.
- [41] A.R. Hillman, in: R.G. Linford (Ed.), *Electrochemical Science and Technology of Polymers*, vol. 1, Journals-Researchers, IRAN, 1987, Ch. 5.
- [42] B. Miller, Proc. 6<sup>th</sup> Australian Electrochem. Conf., Geelong, Vic., 19-24 Feb., 1984; J. Electroanal. Chem., 168 (1984) 91.
- [43] Jones, personal communication, 1992.



## Investigating the relationship between NDVI and EVI vegetation indices with ground surface temperature in Tehran

Amir Nazarinejad <sup>a\*</sup>, Mehrdad Nourbakhsh <sup>b</sup>

<sup>a</sup>Department of Civil Engineering and Surveying, Ramsar Branch, Islamic Azad University

<sup>b</sup> Department of Civil Engineering and Surveying, Ramsar Branch, Islamic Azad University

**Journals-Researchers use only:** Received date: 2023.04.12; revised date: 2023.05.15; accepted date: 2023.05.26

### Abstract

Cities became one of the main centers for conducting research due to the fact that they are the main places where people gather. One of the problems that plague the city today, especially the big cities, is the phenomenon of the city's heat island. Many things play a role in the spatial changes of the heat island, among them are human activities and changes in the earth's surface cover, which often lead to the reduction of green space. Several vegetation indices have been developed, and in this research, NDVI and EVI indices were investigated. Earth's surface temperature for Mordad 27, 1400 was retrieved from Landsat images using a single-channel algorithm and the mentioned indices were extracted for the above date. The results showed that most of the city surface was covered by a temperature layer of 305-310 degrees Kelvin. By comparing the indices and the temperature of the earth's surface, it was found that the temperature of the earth's surface and vegetation have an opposite relationship so that in the south and east the temperature is lower and the vegetation is more; But this issue is the opposite for the south and west. Also, the relationship between the surface temperature of the earth and the EVI index was equal to -31.23%, and its relationship with the NDVI index was about -24%; This shows that these two indicators are similar with a slight difference. © 2017 Journals-Researchers. All rights reserved. (DOI:<https://doi.org/10.52547/JCER.5.2.29>)

**Keywords:** Earth surface temperature, Tehran, single channel algorithm, EVI, LST

### 1. Introduction

The global temperature has increased continuously in recent decades, in connection with population and economic growth, and global warming has become an international challenge for the 21st century (Feng et al, 2019; Zhao et al., 2018). Urban microclimate has undergone severe changes due to land use changes and rapid urbanization and has caused global warming (Guo et al., 2020). Urban

heat island (UHI) has serious negative effects on urban ecosystems and human well-being. (Wu et al., 2019).

A recent report by the United Nations estimates that 55% of the world's population is urban and projects that the urban population will increase to 68% by 2050 (Mukherjee & Singh, 2020). Earth surface temperature (2) LST is an important parameter in investigating surface features, surface energy exchange, and surface physical and chemical processes, and it is currently widely used in soil, hydrology, biology, and urban geochemistry.

\* Corresponding author. Tel.: 989111932123; e-mail: amimazarinejad@gmail.com.

(Tomlinson et al., 2011; Hao et al., 2016; Qiao et al., 2020) Although the data from ground meteorological stations have a higher temporal resolution than remote sensing data, it is difficult to use them in large-scale research. Easy access, better spatial resolution, and more spatial coverage encourage more researchers to use remote sensing data to measure UHI.

Due to the issues of global climate change, the temperature of the earth's surface has increased, which has affected land use, land cover, vegetation areas, water resources, etc. (Solangi et al., 2019) The resulting expansion of modern cities through The change in urban land cover to artificial levels as a key factor has caused the LST of the urban environment to increase compared to its surrounding environment (Mensah et al., 2020). The most widely used spectral index in LST is the normalized differential vegetation index (3). NDVI is used in the extraction of green vegetation (Guha & Govil, 2020). Meanwhile, the first application area that most researchers have focused on is the study of the relationship between 1 ULST and the abundance of vegetation (ZHANG et al., 2009).

In this regard, several types of research have been conducted, among which some cases can be mentioned. In research, the relationship between ground surface temperature and environmental characteristics was investigated, and the results showed that the highest temperature was in bare soil and residential areas, and the lowest temperature was in garden areas. The highest and lowest values of surface temperature were related to Pabdeh-Gorpi and Asmari formations (Vali et al., 2018). A study conducted between 2003-2018 in Arsanjan City, it showed that during that period, the vegetation index decreased, but the temperature changes increased. According to the results, the highest negative correlation between crop cover and surface temperature was obtained, which was equal to -94.0 (Ebrahimi et al., 2019). In a research paper, the analysis of the spatial and temporal relationship between land surface temperature (LST) and normalized vegetation density index (NDVI), and built density index (BDI) was in Bala-Hill, Nairobi, Kenya. Land cover changes with analysis Two indices NDVI and BDI are shown. Land cover changes are shown by analyzing two indices, NDVI

and BDI. The results showed the highest temperature increase at the top of the hill up to 96.3 degrees Celsius between 2015 and 2017 (Mwangi et al., 2018). The results of another paper showed a strong negative correlation between LST and both NDVI and EVI. In general, the 3 classes of LCZ with lower vegetation cover show higher day and night LST. Building area fraction and impervious surfaces showed a positive correlation with nighttime LST and transient area fraction presented a negative correlation with nighttime LST (Ferreira & Duarte, 2019).

## 2. Area of study

As the capital of Iran, Tehran is the largest and most populous city in Iran with a population of 9 million. The population of Tehran has increased approximately 10 times since 1950. This city is located in the north of Iran and the south of the Alborz mountain range in the longitude of 51 degrees to 40 degrees and 51 minutes east and latitudes of 35 degrees and 30 minutes to 35 degrees and 51 minutes. The height of the city varies between 945 and 2244 meters above sea level (Khoshnoodmotlagh et al., 2020). Figure 1 shows the map of the studied area.

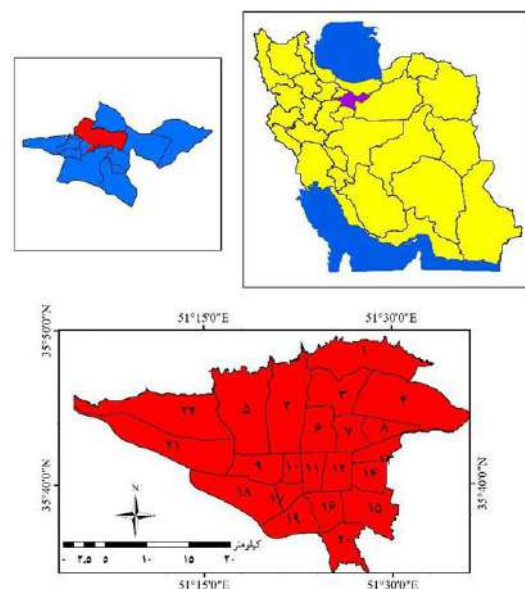


Figure (1). The study area (Mortazavi Asal et al., 1400)



### 3. Materials and methods

Landsat 8 satellite images were used to investigate the relationship between land surface temperature and vegetation indices, and the date of this image was August 27, 1400. For this purpose, the required pre-processing including geometric correction, radiometric correction, and atmospheric correction was done. The processing included vegetation indices 1NDVI and 2EVI and a single channel algorithm was used for the surface temperature.

### 4. NDVI Index

The normalized differential vegetation index is derived from equation 1. In this regard; NIR is the near-infrared band and RED is the red band (Hashemi-Darebadami et al., 2019).

$$NDVI = \frac{NIR - RED}{NIR + RED} \quad \text{Equation (1)}$$

In this equation, NIR is a reflection in the infrared band and Red is a reflection in the red band.

### 5. EVI Index

This algorithm has been developed for areas with high biomass. This algorithm improves canopy effects and reduces atmospheric effects (Maleki et al., 2018). This index is obtained using equation 2.

$$NDVI = G \frac{NIR - RED}{NIR + C1 \times RED - C2 \times Blue + L} \quad \text{Equation (2)}$$

In this equation, Blue is the reflection in the blue band,  $L=1$ ,  $C2=7.5$ ,  $C1=6$ , and  $G=2.5$ .

### 6. Earth surface temperature from single channel algorithm

The Tek algorithm was used to determine the temperature of the earth's surface. This algorithm by James-Muñoz et al., 2014, uses the thermal band of Landsat images and is calculated in the same way for all Landsat images with equation 3 (Jiménez-Muñoz et al., 2014).

$$T_s = \gamma \left[ \frac{1}{\epsilon} (\varphi_1 L_{sen} + \varphi_2) + \varphi_3 \right] \quad \text{Equation (3)}$$

In this regard,  $T_s$  is the temperature of the earth's surface,  $\epsilon$  is the radiant power of the earth's surface, and  $L_{sen}$  is the radiance on the surface.  $r$  and  $\varphi$  are calculated from the relation to 4.

$$\gamma \approx \frac{T_{sen}^2}{b_\gamma L_{sen}}; \delta \approx T_{sen} - \frac{T_{sen}^2}{b_\gamma} \quad \text{Equation (4)}$$

In this, the  $T_{sen}$  temperature of the surface brightness of the sensor,  $b$  (1324 for Landsat 8) and 1 2 3 are atmospheric functions that reach 8 according to the relation 5 for Landsat (Maleki et al., 2019).

$$\begin{bmatrix} \varphi_1 \\ \varphi_2 \\ \varphi_3 \end{bmatrix} = \begin{bmatrix} 0.04019 & 0.02916 & 1.01523 \\ -0.38333 & -1.50294 & 0.20324 \\ 0.00918 & 1.36072 & -0.27514 \end{bmatrix} \quad \text{Equation (5)}$$

In the end, the coefficient of determination was used to investigate the relationship between the surface temperature and vegetation indices.

### 7. Results

The results of this study can be examined in three parts: 1) Distribution and how the temperature classes change, 2) Spatial changes of vegetation indices, and 3) The relationship between the temperature of the earth's surface and vegetation.

Figure 2 shows the surface temperature map. According to this map, the temperature of the earth's surface was between 301 and 326 degrees Kelvin, where the temperature layer of 305-310 has the largest spatial extent and the initial and final layers have the smallest spatial extent. In another division, the eastern half of the city is cooler than the western half, and on the other hand, the north of the city has cooler conditions than the south of the city.

EVI and NDVI indices were used for vegetation, and the values obtained from them were compared in this section. Figure 3 shows the vegetation map using the EVI index. Negative values in the figure are often water areas, which are also shown in blue on the map. The dominant class in this index is values between 0.1 and 0.2. According to the information obtained from this index, the state of vegetation in the north of

the city is better than the south of the city and the eastern half is better than the western half.

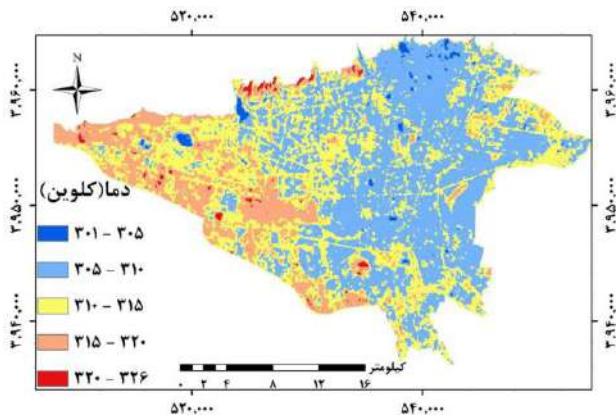


Figure (2). Earth surface temperature map

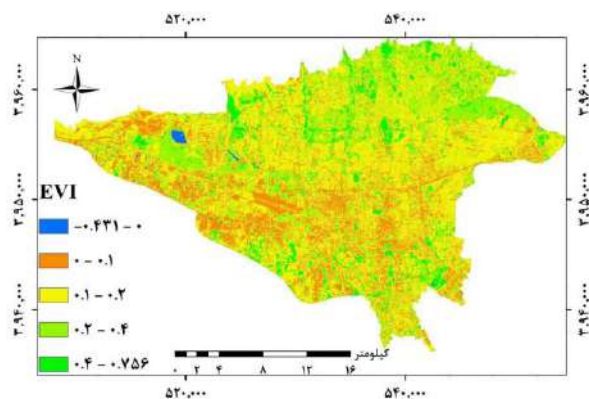


Figure (3). Vegetation map using EVI index

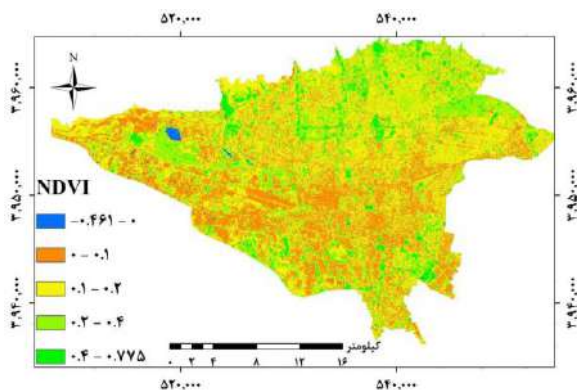


Figure (3). Vegetation map using NDVI index

Another index used was the NDVI index, the results of applying this index are presented in Figure 4. Negative numbers in this index also indicate water areas. The primary difference between this map and map 3 is that the dominant class in this map is 0-1.0. In this map, the north has better vegetation status than the south and the east than the west of the city, with the difference that the intensity of differences between the regions is less than the EVI index.

The coefficient of determination shows the explanatory power of the model. The coefficient of determination shows how many percent of the changes in the dependent variable are explained by the independent variables. It indicates the probability of correlation between two categories of data in the future. Figure 4 shows the coefficient of determination between the surface temperature and the EVI index. According to this graph, the coefficient of determination or detection for these two variables was equal to 31.23%, which indicates that to some extent the control of the surface temperature in the city of Tehran is controlled by the vegetation, but this relationship is not very strong and the temperature of the city of Tehran It is influenced by many factors.

Figure 5 shows the coefficient of determination between land surface temperature and NDVI index. According to this diagram, the coefficient of determination between NDVI index and surface temperature is about 24%. This problem makes it clear that even though the relationship between NDVI index and the surface temperature of the earth is somewhat stronger, but as mentioned, several criteria are effective in determining the temperature of the surface of the earth.

The temperature of the earth's surface, followed by the heat island of the city, is one of the issues that urban experts seek to solve as a global challenge. LST reflects the result of interactions between the surface and the atmosphere and the energy flux between the earth and the atmosphere on the earth. (Liu & Weng, 2009) Therefore, it can be said that the temperature of the earth's surface is partially influenced by the physical characteristics of the earth's surface, such as the type of land use. And on the other hand, the energy flow is also affected by atmospheric characteristics such as air pollution. Therefore, investigating the effect of different

parameters on the temperature of the earth's surface can lead to the reduction of the earth's temperature and consequently the reduction of the negative effects of the earth's surface temperature.

Vegetation is one of the land surface covers, which constitutes a small percentage of the city surface in most cities, especially cities in arid and semi-arid regions. Studies have shown that vegetation has a significant effect on reducing the temperature of the earth's surface and usually after water applications in the city, the lowest average temperature is related to vegetation (Mortazaviasal et al., 1400). Therefore, investigating the relationship between vegetation and surface temperature has become one of the most attractive research issues in planning the reduction of surface temperature and heat islands.

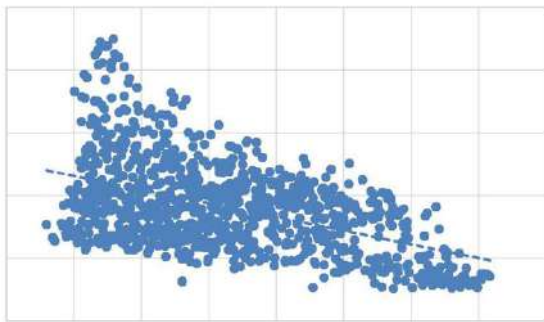


Figure 4. The graph of the coefficient of determination between the temperature of the earth's surface and the EVI index

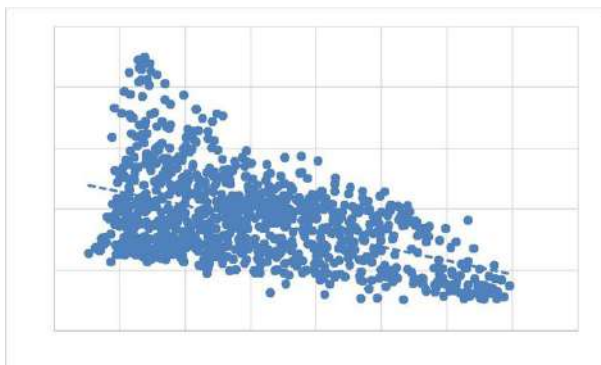


Figure (5). is the graph of the coefficient of determination between the temperature of the earth's surface and the NDVI index

A large number of vegetation indices based on the processing of satellite images have been developed, among which we can mention: normalized differential vegetation index (NDVI), soil-adjusted vegetation index (SAVI), vegetation fraction index (RVI) Improved vegetation index (EVI) and...

Each of these indicators has a unique feature. This study examined the difference in the effect of two normalized differential vegetation indices (NDVI) and improved vegetation index (EVI) on the spatial distribution of surface temperature changes. The results indicated that the spatial distribution of surface temperature in Tehran city is inversely proportional to vegetation cover so that the temperature of the surface of the earth was higher in the south than in the north and in the east was higher than in the west, which is the case for the opposite indices. The relationship between the temperature of the surface of the earth and the EVI index was equal to -31.23% and its relationship with The NDVI index was around -24%, which indicates that these two indices are similar with a slight difference.

## 8. Conclusion

The temperature of the earth's surface, followed by the heat island of the city, is one of the issues that urban experts seek to solve as a global challenge. LST reflects the result of interactions between the surface and the atmosphere and the energy flux between the earth and the atmosphere on the earth. (Liu & Weng, 2009) Therefore, it can be said that the temperature of the earth's surface is partially influenced by the physical characteristics of the earth's surface, such as the type of land use. And on the other hand, the energy flow is also affected by atmospheric characteristics such as air pollution. Therefore, investigating the effect of different parameters on the temperature of the earth's surface can lead to the reduction of the earth's temperature and consequently the reduction of the negative effects of the earth's surface temperature.

Vegetation is one of the land surface covers, which constitutes a small percentage of the city surface in most cities, especially cities in arid and semi-arid regions. Studies have shown that vegetation has a significant effect on reducing the temperature of

the earth's surface and usually after water applications in the city, the lowest average temperature is related to vegetation (Mortazaviasal et al., 1400). Therefore, investigating the relationship between vegetation and surface temperature has become one of the most attractive research issues in planning the reduction of surface temperature and heat islands.

A large number of vegetation indices based on the processing of satellite images have been developed, among which we can mention: normalized differential vegetation index (NDVI), soil-adjusted vegetation index (SAVI), vegetation fraction index (RVI) Improved vegetation index (EVI) and... Each of these indicators has a unique feature. This study examined the difference in the effect of two normalized differential vegetation indices (NDVI) and improved vegetation index (EVI) on the spatial distribution of surface temperature changes. The results indicated that the spatial distribution of surface temperature in Tehran city is inversely proportional to vegetation cover so that the temperature of the surface of the earth was higher in the south than in the north and in the east was higher than in the west, which is the case for the opposite indices. The relationship between the temperature of the surface of the earth and the EVI index was equal to -31.23% and its relationship with The NDVI index was around -24%, which indicates that these two indices are similar with a slight difference.



## 9. References

- [1] Wali, Abbas Ali, Ranjbar, Abolfazl, Makram, Marzieh and Tari Panah, Farida. (1398). Investigating the relationship between the temperature of the earth's surface, geographical and environmental characteristics and biophysical indicators using images Landsat Remote sensing and geographic information system in natural resources, 10(3), 58-35..
- [2] Ebrahimi, Ali., Motamedoziri, Bahark., Nazim Al-Sadat, Seyyed Mohammad Jafar and Ahmadi, Hassan. (1399). Investigating the relationship between the surface temperature of the earth and changes in vegetation and water area in Arsanjan City, Iran. Remote sensing and geographic information system in natural resources, 11(4), 65-86.
- [3] Mortazavi Asl, Seyed Kamiar, Saeedi Rizvani, Navid, Rezaei, and Mahmoud. (1400). The effect of land use on the spatial distribution of cool islands in Tehran. Quarterly Journal of Geographical Studies of Mountainous Regions. 2 (6), 33-50.
- [4] Liu, H., & Weng, Q. (2009). Scaling effect on the relationship between landscape pattern and land surface temperature. *Photogrammetric Engineering & Remote Sensing*, 75(3), 291-304.
- [5] Feng, Y., Wang, X., Du, W., Liu, J., & Li, Y. (2019). Spatiotemporal characteristics and driving forces of urban sprawl in China during 2003–2017. *Journal of Cleaner Production*, 241, 118061.
- [6] Ferreira, L. S., & Duarte, D. H. S. (2019). Exploring the relationship between urban form, land surface temperature and vegetation indices in a subtropical megacity. *Urban Climate*, 27, 105-123.
- [7] Guha, S., & Govil, H. (2020). Seasonal impact on the relationship between land surface temperature and normalized difference vegetation index in an urban landscape. *Geocarto International*, 1-21.
- [8] Guo, A., Yang, J., Sun, W., Xiao, X., Cecilia, J. X., Jin, C., & Li, X. (2020). Impact of urban morphology and landscape characteristics on spatiotemporal heterogeneity of land surface temperature. *Sustainable Cities and Society*, 63, 102443.
- [9] Hao, X., Li, W., & Deng, H. (2016). The oasis effect and summer temperature rise in arid regions-case study in Tarim Basin. *Scientific reports*, 6(1), 1-9.
- [10] Hashemi Darebadami, S., Darvishi Bolooriani, A., AlaviPanah, S. K., Maleki, M., & Bayat, R. (2019). Investigation of changes in surface urban heat-island (SUHI) in day and night using multi-temporal MODIS sensor data products (Case Study: Tehran metropolitan). *Journal of Applied researches in Geographical Sciences*, 19(52), 113-128.
- [11] Jiménez-Muñoz, J. C., Sobrino, J. A., Skoković, D., Mattar, C., & Cristóbal, J. (2014). Land surface temperature retrieval methods from Landsat-8 thermal infrared sensor data. *IEEE Geoscience and remote sensing letters*, 11(10), 1840-1843.
- [12] Khoshnoodmotlagh, S., Daneshi, A., Gharari, S., Verrelst, J., Mirzaei, M., & Omrani, H. (2021). Urban morphology detection and it's linking with land surface temperature: A case study for Tehran Metropolis, Iran. *Sustainable Cities and Society*, 74, 103228.
- [13] Maleki, M., Ahmadi, Z., & Dosti, R. (2019). Kermanshah land surface temperature changes in during 1393-1397 periods. *Geography and Human Relationships*, 2(3), 309-319.
- [14] MALEKI, M., TAVAKKOLI-SABOUR, S-M., & JAVAN, F. (2018). Analysis of the Effects of Dam Construction on Vegetation of Peripheral Areas in Different Heights and Slopes. Case: Sulayman Shah and Gushan Dam.
- [15] Mensah, C., Atayi, J., Kabo-Bah, A. T., Švik, M., Acheampong, D., KyereBoateng, R., ... & Marek, M. V. (2020). Impact of urban land cover change on the garden city status and land surface temperature of Kumasi. *Cogent Environmental Science*, 6(1), 1787738.
- [16] Mukherjee, F., & Singh, D. (2020). Assessing land use–land cover change and its impact on land surface temperature using LANDSAT data: A comparison of two urban areas in India. *Earth Systems and Environment*, 4(2), 385-407.
- [17] Mwangi, P. W., Karanja, F. N., & Kamau, P. K. (2018). Analysis of the relationship between land surface temperature

- and vegetation and built-up indices in upper-hill, Nairobi. *Journal of Geoscience and Environment Protection*, 6(1), 1-16.
- [18] Qiao, Z., Liu, L., Qin, Y., Xu, X., Wang, B., & Liu, Z. (2020). The impact of urban renewal on land surface temperature changes: a case study in the main city of Guangzhou, China. *Remote Sensing*, 12(5), 794.
- [19] Solangi, G. S., Siyal, A. A., & Siyal, P. (2019). Spatiotemporal dynamics of land surface temperature and its impact on the vegetation. *Civil Engineering Journal*, 5(8), 1753-1763.
- [20] Tomlinson, C. J., Chapman, L., Thornes, J. E., & Baker, C. (2011). Remote sensing land surface temperature for meteorology and climatology: A review. *Meteorological Applications*, 18(3), 296-306.
- [21] Wu, C., Li, J., Wang, C., Song, C., Chen, Y., Finka, M., & La Rosa, D. (2019). Understanding the relationship between urban blue infrastructure and land surface temperature. *Science of the Total Environment*, 694, 133742.
- [22] Zhang, X., Zhong, T., Feng, X., & Wang, K. (2009). Estimation of the relationship between vegetation patches and urban land surface temperature with remote sensing. *International Journal of Remote Sensing*, 30(8), 2105-2118.
- [23] Zhao, C., Jensen, J., Weng, Q., & Weaver, R. (2018). A geographically weighted regression analysis of the underlying factors related to the surface urban heat island phenomenon. *Remote Sensing*, 10(9), 1428.



# A review on Simulate Fracture and Ultra-Low Cycle Fatigue in Steel Structures by ABAQUS

Ali Mirzaee <sup>a\*</sup>, Ayoub Harouni Kajal <sup>b</sup>

<sup>a</sup> Department of Civil Engineering, Science and Research Branch, Islamic Azad University, Tehran, Iran

<sup>b</sup> Department of Civil Engineering, West Tehran Branch, Islamic Azad University, Tehran, Iran

**Journals-Researchers use only:** Received date: 2023.03.05; revised date: 2023.04.15; accepted date: 2023.05.20

## Abstract

In recent years, many advances have been made in fatigue and failure modeling in steel structures. The methods used to simulate failure and fatigue caused by earthquakes in steel structures are based on experimental and semi-empirical methods or conventional fracture mechanics. Semi-empirical methods cannot be generalized to a wide range of structural details, but conventional fracture mechanics can be reliably used only to simulate brittle fractures such as those observed in the Northridge and Kobe earthquakes, where large-scale yielding is absent. Similar to what is described in this paper, physics-based micromodels seek to simulate the fundamental processes of void growth and coalescence and granular shear responsible for very low-cycle fracture and fatigue in structures. These models are relatively free of assumptions about behavior and can be accurately used to simulate fracture and fatigue in a general sense under different conditions. The growth of voids or cracks can cause sudden crack propagation and deterioration of strength on a global scale of structural components. Therefore, these micromodels, relying on fundamental physics, are equally applicable to situations considered as "brittle" or "unbreakable" at the structural or component level. Examples are given to demonstrate the use of one of these models - the Cyclic Void Growth Model (CVGM) - to simulate failure through continuous finite element analyses. © 2017 Journals-Researchers. All rights reserved. (DOI: <https://doi.org/10.52547/JCER.5.2.36>)

**Keyword:** crack; fracture energy; low cyclic; fatigue; steel structure

## 1. INTRODUCTION

It confirmed the significant probability of failure in steel flexural frame joints and the sensitivity of the response to local effects that are difficult to quantify with structural engineering models and conventional

fracture mechanics. The SAC investigation [9] and related studies have mitigated the immediate problem of premature brittle fractures through the development of improved connection details that employ tougher materials, and reduced fracture toughness demands. However, even these post-Northridge connections can

\* Corresponding author. Tel.: +989120585600; e-mail: ali-mirzaee@srbiau.ac.ir.

potentially fracture, although in a ductile manner [20]. Moreover, there are many situations outside the scope of the SAC investigation where the fracture is likely to compromise the seismic safety of the system, such as brace and connection fracture in concentrically braced frames or link-column connection fractures in eccentrically braced frames [16].

Finally, as we move further into the realm of performance-based design, methods, and tools are needed to quantify fracture behavior over a range of seismic demands (hazards), as opposed to simply “qualifying” the structure to perform “adequately” for a single limit state. Given the importance of fracture, this paper addresses the issue in a wider scientific context by examining the accuracy, feasibility and validity of traditional and evolving approaches to characterize earthquake-induced fracture in steel structures. The approaches discussed in this paper encompass various scales of simulation (micro to structure scale), levels of sophistication, and computational resources required to predict fracture. Some important questions are (1) Are traditional fracture and fatigue prediction techniques accurate and general enough to be applied to a wide range of structural configurations under various loading conditions? (2) If not, are more fundamental models available to improve the assessment of fracture? (3) Is the application of these advanced models computationally feasible? (4) If so, what are the major challenges to the implementation of these models?

This paper briefly and qualitatively describes processes responsible for earthquake-induced fracture, and then reviews the state of the art of earthquake-induced fracture and fatigue prediction in steel structures.

Important limitations of the existing approaches are described and newer physics-based approaches, including the recent development of models for ULCF are introduced. Issues regarding the implementation of these approaches are discussed.

## **2. EARTHQUAKE-INDUCED FRACTURE DUE TO ULTRA LOW CYCLE FATIGUE AND**

## **REVIEW OF CONVENTIONAL APPROACHES TO PREDICT ULCF**

Widespread damage to steel-framed buildings during the 1994 Northridge earthquake confirmed the significant likelihood of fracture in steel moment frame connections and the sensitivity of response to local effects that are difficult to quantify with conventional structural engineering and fracture mechanics models. This section introduces the phenomenon of earthquake-induced ULCF from a physical standpoint and reviews various techniques that are commonly used to characterize ULCF in steel structures, before describing the micromechanics-based approach to ULCF.

Earthquake-induced fracture in structures is typically preceded by a small number of high-amplitude cyclic strain or load reversals. Thus, earthquake-induced fracture may be classified as a fatigue problem. The traditional view of fatigue encompasses crack initiation and propagation under a large number of load reversals, ranging from several hundred to a few million cycles. For example, fatigue typically occurs in bridges or mechanical components, where the amplitude of the cyclic demands is small relative to the yield stress of the material and the number of cycles to failure is large. Within this range, fatigue is commonly distinguished between low-cycle and high-cycle fatigue. In contrast to classical high or low-cycle fatigue encountered in bridges or mechanical components, steel structures subjected to earthquakes experience fatigue processes involving fewer than ten cycles with large strain amplitudes, on the order of ten or more times the yield strain. Termed Ultra Low Cycle Fatigue (ULCF), this type of fatigue/fracture occurs in modern steel structures that are designed to absorb seismic energy by sustaining large inelastic deformations under cyclic loads. Plastic hinging of beam-column connections [20] and inelastic cyclic buckling of steel braces [8] are two primary examples where ULCF fracture is the ultimate limit state. An example of ULCF fracture for a steel brace is shown in Fig. 1.



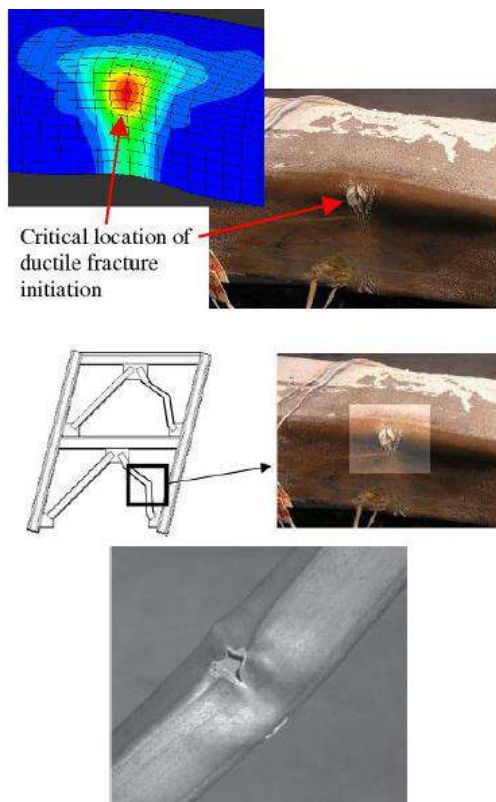


Figure 1. Ultra low cycle fatigue in a concentric steel braces [8]

While ULCF-type behavior has long been recognized in seismic design, the fundamental physical processes responsible for this type of fatigue are not well understood. As a result, earthquake engineering and other situations involving ULCF have relied on various empirical or semi-empirical approaches to evaluate and develop suitable design provisions. While these approaches work well for a given structural detail or loading history, they cannot be generalized conveniently and may be expensive.

### 3. Experiment-Based Modeling

The most popular approaches to assess the fracture susceptibility of steel structures and components are experiment-based empirical methods. These approaches involve testing structural subassemblies under pre-defined monotonic or cyclic loading protocols and then using gross measures of

deformations (inter-story drift, joint rotation) to establish performance limits, and to predict fracture or fatigue capacity.

Experiment-based modeling is attractive mainly because, for a given component, it is relatively free from assumptions except an accurate representation of boundary conditions, and incorporates all aspects of behavior and various physical phenomena like local buckling, material variability, contact, gapping, etc. Also, experiment-based modeling is often the only viable approach, mainly because reliable models may not be available to simulate the physical phenomena contributing to response.

Despite its advantages, test-based modeling cannot be easily generalized to structural details that differ significantly from the tested components in terms of geometry or material types. Due to the high cost of tests, sensitivity, and parametric studies and the use of intermittent loading histories are often not possible. Indeed, some judgment is required to generalize experimental results, which may lead to a conservative description of the adequacy of a given component, rather than an assessment of performance across the full spectrum of behavior. Finally, modeling at the component or structural scale does not provide insights into local effects that may be responsible for the fracture.

### 4. Conventional Fracture and Fatigue Mechanics

Conventional fracture mechanics (CFM) typically involves the determination of a single parameter at a crack tip that is assumed to quantify the fracture toughness demand.

Consequently, the fracture toughness capacity, too, is expressed in terms of a similar parameter. The toughness demand parameter (such as the stress intensity factor  $K_I$ , or the  $J$ -integral, or the Crack Tip Opening Displacement – CTOD), is typically determined either through analytical formulae or finite element simulations. The corresponding material toughness capacity  $K_{IC}$  or  $J_{IC}$  (critical stress intensity factor or  $J$ -integral), is typically determined from standard tests. The fracture toughness typically corresponds to the energy release rate (per unit advance of the crack front). Conventional fracture mechanics is further classified as Linear Elastic



Fracture Mechanics (LEFM – featuring KI) and Elastic-Plastic Fracture Mechanics (EPFM – featuring J and CTOD), suitable for different levels of crack-tip plasticity.

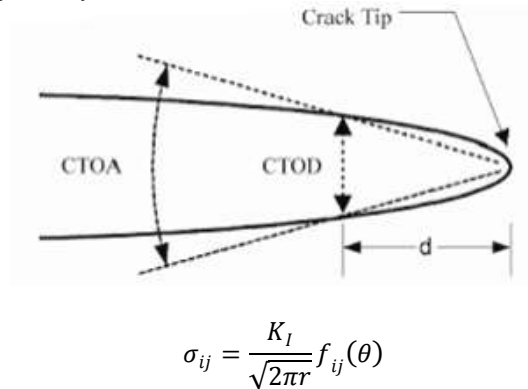


Figure 2. Conventional fracture mechanics methods (a) linear elastic fracture mechanics and (b) crack tip opening displacement – elastic plastic fracture mechanics

While CFM has been used extensively by mechanical and aerospace research and practice, efforts to apply these approaches to civil structures have been fairly recent [4], where CFM-type approaches were used to characterize the fracture susceptibility of pre- and post-Northridge beam-column connection details.

CFM methods are more general as compared to experiment-based methods, mainly because they are based on fairly local stress and strain fields, and, in concept, characterize resistance to fracture at the material level, rather than at the component level.

In fact, the Chi study demonstrated that CFM-type approaches could be used to characterize the ductility of pre-Northridge-type details.

Despite their advantages, CFM approaches have several limitations. For example, they can reliably describe the fracture process only in situations where the yielding is limited in extent, and when a sharp crack is present. They are less suited to conditions of large-scale yielding or details without sharp cracks, such as commonly encountered in post-Northridge connection details. Moreover, as discussed earlier, earthquake-induced fracture is a fracture-fatigue interaction problem, and thus CFM type approaches that do not explicitly include the effects of reversed

cyclic loading cannot be conveniently applied to situations of earthquake-induced fatigue.

In addition to the CFM approaches, traditional fatigue mechanics approaches are often adapted and used in conjunction with experimental analysis or finite element methods. These methods can be classified further into strain/stress-life approaches or damage tolerant approaches. The strain life approaches typically involve dividing the loading history at the component or strain level into equivalent cycles of fixed amplitude and then comparing the accumulated cycles to the “strain-life” determined from other experiments on similar details [6]. Such approaches have been used, for example, Liu and Goel [15], who predicted the fatigue life of bracing elements based on slenderness and width-thickness ratios. However, the Uriz and Mahin [24] study applied this approach to a fiber-based local strain history rather than the entire member. Damage-tolerant fatigue approaches [14] are less common in structural engineering, although they are less applicable as well because they rely on CFM approaches such as the J-integral or stress-intensity factor.

These conventional fatigue mechanics methods, too are somewhat difficult to adapt to ULCF type situations mainly because (1) Strain life approaches are typically difficult to generalize to various components because ULCF is caused by interactions of stress and strain histories (2) ULCF is often accompanied by large scale yielding, which may invalidate stress intensity based  $\Delta K$  or  $\Delta J$  type approaches (3) Earthquake loading histories are extremely random, with very few cycles, making them difficult to adapt to conventional cycle counting techniques such as Rainflow analysis [21] (4) Damage tolerant  $\Delta K$  type methods typically require the real or presumed presence of an initially sharp crack or flaw, which might be absent in many structural details.

These models (also referred to as “local fracture mechanics”) are applied at the continuum level (in contrast to the component or structure level), through interpretations of stress and strain histories that may be computed through detailed finite element analysis. While other approaches are sometimes used to predict fracture at the continuum level through measures such as critical fracture strains, the micromechanics-based models aim to be more sophisticated, by considering

the interactions of multiple stress and strain components that are responsible for ULCF initiation.

### 5. The Cyclic Void Growth Model to Predict Earthquake-Induced ULCF in Steel Structures

To summarize the preceding discussion, earthquake-induced fracture in structures presents a complex problem because it involves the complex interactions of material microstructure, irregular loading histories, and uncertainties in crack initiation and subsequent propagation processes. Fundamental micromechanics-based “local” models show promise in predicting fracture and fatigue under such situations, because they are based on the physical processes of void growth and coalescence responsible for ULCF, and therefore are relatively free from many assumptions that limit the applicability of other common approaches. Several such models have been used for ductile fracture conditions under monotonic loading [10, 11, 12, 17, 18]. In addition to focusing on monotonic loading only, all these studies were conducted for pressure vessels and other steels not commonly used in structural engineering. The use of such models in structural engineering has been fairly recent e.g. El-Tawil et al, [7] and Chi et al, [5]. This section discusses the recently introduced Cyclic Void Growth Model (CVGM), and then describes a procedure to apply it along with validation data obtained from a recent NEESR project [13].

For monotonic loading, ductile fracture in steel is caused by the processes of void nucleation, growth, and coalescence [2]. On the application of a triaxial stress field in steel, voids nucleate and grow around inclusions (mostly carbides in the steel material matrix) to coalesce until a macroscopic crack is formed (see Fig. 3). Previous research, Rice and Tracey [19] has shown that void growth is controlled by the equivalent plastic strain,  $\epsilon_p$ , and stress triaxiality  $T = \sigma_m / \sigma_e$ , where  $\sigma_m$  is the mean or hydrostatic stress and  $\sigma_e$  is the von Mises stress.

Equation (1) describes the critical condition of the Void Growth Model (VGM) [20]. The numerator in the equation, based on derivations by Rice and Tracey quantifies a void growth that must exceed the void growth capacity critical monotonic VGI to trigger ductile fracture. The void growth demand is based on

stress and strain evolutions at a continuum point and can be determined through detailed FEM analysis, while the void growth capacity can be determined based on tension tests of notched bar specimens [14].

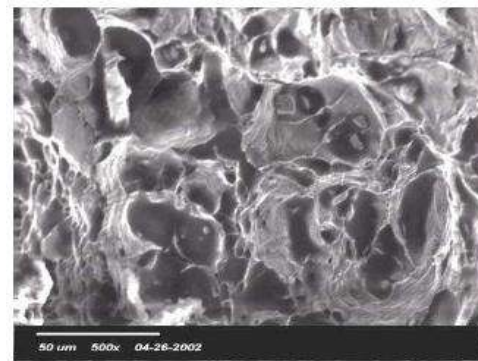
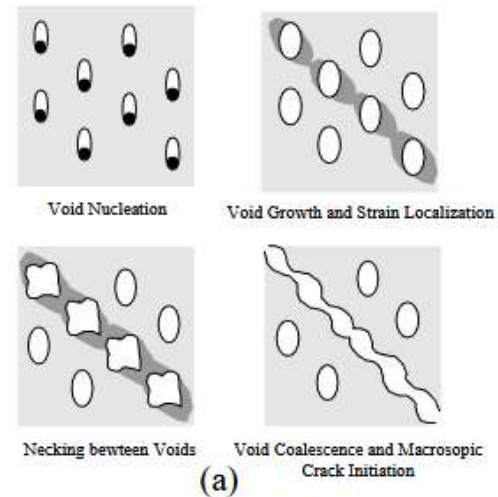


Figure 3. (a) void growth and coalescence leading to ductile fracture in steel and (b) the corresponding dimpled fracture surface [13]

$$Fracture\ Index = \frac{\int_0^{\epsilon_p} \exp(1.5T) d\epsilon_p}{VGI_{monotonic}^{critical}} \quad (1)$$

While originally proposed for steels used in pressure vessels and nuclear applications, recent studies have validated these models for a large variety of low-carbon structural steels used commonly in civil engineering construction.

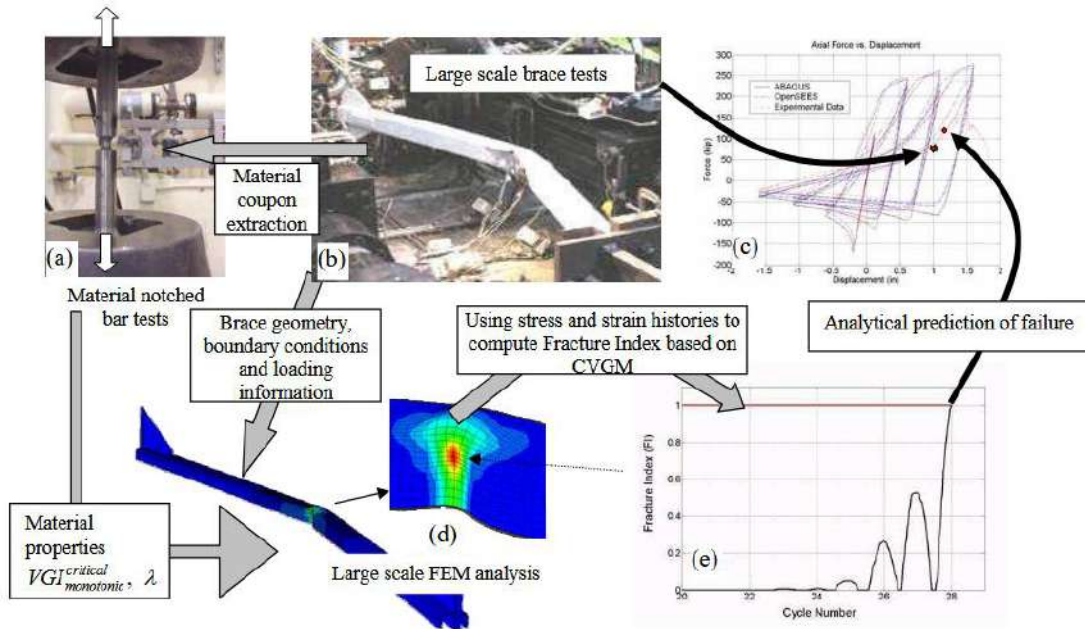


Figure 4. Prediction of ULCF in a concentric brace using the cyclic void growth model [14]

$$Fracture\ Index = \frac{\sum_{tensile-cycles} \int_{\epsilon_1}^{\epsilon_2} \exp(|1.5T|) \cdot d\epsilon_p - \sum_{compressive-cycles} \int_{\epsilon_1}^{\epsilon_2} \exp(|1.5T|) d\epsilon_p}{VG_{monotonic}^{critical} \exp(-\lambda \delta_p^{accumulated})} > 1 \quad (2)$$

For ULCF, both void growth and void collapse need to be explicitly considered, due to the reversed cyclic nature of the load. Recent research led to the development of a model that simulates the micromechanisms of void growth, collapse, and cyclic degradation that are responsible for Ultra Low Cycle Fatigue. Equation (2) describes the critical condition of the CVGM that must be attained to trigger ULCF initiation.

Similar Void Nucleation Void Growth and Strain Localization Necking between Voids Void Coalescence and Macroscopic Crack Initiation (a) (b) to (1), the numerator of the equation reflects the cyclic micromechanical void growth demand and is based on strains and stresses inferred through finite element analysis, and the denominator reflects material capacity, calibrated through convenient small scale tests, such that ULCF is assumed to initiate when the Fracture Index (FI) exceeds 1. The model contains one additional parameter  $\lambda$  (quantifying the rate of

capacity degradation) that is calibrated through multiple cyclic tests of notched bar specimens.

The CVGM model too, has been validated using fractographic studies as well as small, medium and large scale tests, most recently as part of a NEESR project. Because the CVGM and similar models simulate the fundamental physics of the ULCF process, and are applied at a continuum level, rather than the component or structural level, they can be applied in a general sense to a wide variety of structural details to improve their performance.

## 6. Procedure for predicting Ultra Low Cycle Fatigue in structural components using the Cyclic Void Growth Model

Figure 4 schematically illustrates the various steps/components of predicting ULCF based on CVGM, and their inter-relationships. As discussed

earlier, the Cyclic Void Growth Model has two material parameters ( VGI and  $\lambda$  ) that can be calibrated from small-scale tests and complementary finite element analysis of notched bar specimens such as the one shown in Fig. 4a. A detailed calibration procedure is discussed in detail in Kanvinde and Deierlein [14]. For a given steel type typically ten experiments (four monotonic and six cyclic) are required to calibrate the two parameters. These experiments usually include different notch sizes to query the effect of stress state or triaxiality (sharper notches result in higher triaxiality).

Once the parameters have been calibrated, detailed finite element analysis of large scale components can be conducted to determine the stress and strain histories at each continuum point within the component. Recently, the authors tested 19 large-scale concentric brace elements cyclically to validate the CVGM model for full scale specimens. Hollow bracing elements typically undergo inelastic cyclic buckling followed by local buckling of the cross section leading to large strain amplification, and eventually ULCF induced fracture [8].

Thus, they present an ideal test-bed to validate the CVGM model. Figure 4b shows a photograph of a representative brace specimen as it buckles, while Fig. 4c includes the axial load deformation plot for the specimen, as well as the instant during the loading history when fracture initiation was first observed (marked by a star symbol). Figure 4d shows a FEM simulation (performed on ABAQUS [1]) of this specimen (the brace is a 10-foot-long HSS 4X4X1/4 shape). The simulation considers all the relevant aspects of behavior, and features multiaxial plasticity with combined isotropic and kinematic hardening. The parameters for the plasticity model are inferred from the small scale coupon tests. To simulate the local buckling accurately, initial imperfections must be prescribed to perturb the analysis. Initial imperfections are inputted into the model by scaling the appropriate global and local buckling modes of the brace to measure the imperfections of the experimental specimen. A simulation-based load deformation plot is overlaid on the experimental plot in Fig. 4c, and the agreement between the two is very good.

To predict the location and instant of ULCF initiation, the stress and strain histories are determined from the FEM simulation over the entire plastic hinge

region as the loading progresses, and the Fracture Index (FI) is determined as per (2) at each loading step. It is important to note that FI is determined at each continuum location in the FEM model and is dependent on material parameters (VGI critical monotonic and  $\lambda$ ). Thus, the FI can be determined in a general sense for any component once the material properties have been calibrated using the small scale tests. ULCF is assumed to initiate at a given continuum location when the micromechanical cyclic void growth demand exceeds degraded void size capacity, or mathematically, FI at that location exceeds 1. Fig. 4e plots the FI at the critical location in the locally buckled cross-section profile (indicated by the arrow in Fig.4d), versus the loading time step. The instant when FI exceeds 1 for the first time is recorded as the analytical prediction of ULCF initiation. This point is shown as circle on Fig. 4c. Comparing this point to the experimental fracture instant (shown as a circle in the figure) demonstrates the accuracy of the ULCF models. Furthermore, as is evident from Fig. 4c, the instant of ductile crack initiation predicted from the analysis is very close to that observed during the experiment. Moreover, the physical location of ULCF is predicted with exact precision by the CVGM model.

As noted in Fig. 4c, the CVGM model successfully predicts the point of ULCF initiation in the experiment. A similar agreement between experimental and analytical fracture is observed for all 19 specimens. Given that the test matrix included specimens with different cross-section geometries, different steel materials, and loading histories, the good agreement between experimental and CVGM predictions of the fracture indicates that the CVGM does indeed capture fundamental physical processes and material properties that control fracture. Thus, once material properties are determined using small-scale tests, the CVGM can be applied in a general sense across a range of component geometries, materials and loading histories.

## 7. AREAS FOR REFINEMENT OF THE MICROMECHANICS BASED MODELING APPROACH

While the CVGM and similar micromechanical models provide a fairly general and accurate

framework for predicting earthquake induced fracture in steel structures, there are several issues that need to be addressed to successfully and routinely apply these models in structural simulations. Some of these issues concern the level of sophistication of the FEM simulation, while others are related to the accuracy of the micromechanics- based model itself. Some of these issues are now summarized.

Because the micromechanics-based models are applied at the continuum level, their success is contingent on an accurate characterization of the local stress and strain histories at critical locations. Thus, sophisticated modeling of various physical phenomena that affect these stresses and strains is required. For example, the brace specimens described in this paper required simulation of global and local buckling, which in turn required a detailed definition of initial member imperfections. One can envision that in other situations, various mechanisms may become critical, e.g. gapping and contact in connections including fillet welds, or the loosening of bolts in bolted connections. In addition to this, multiaxial cyclic plasticity model typically need to be calibrated and used for accurate material constitutive response.

In many situations such as welded connections (that include base and weld metal and heat affected zones) it is necessary to consider the spatial gradients and statistical variability in material properties and capacities that may affect the instant and location of ULCF initiation. The second phase of the NEESR project, uses welded column base plate details as a test-bed and investigates some of these issues.

While the model discussed in this paper addresses mainly ULCF initiation, often the fracture propagates in a ductile manner for a considerable duration of time before the component fractures completely [3]. Thus, methods are required to integrate the initiation models with analytical crack propagation capabilities to achieve more realistic estimates of performance.

Another important issue to consider with regard to the micromechanics-based models is that they typically focus on a single mechanism for failure (e.g. microvoid growth and coalescence). However, depending on stress conditions and material properties, various other mechanisms may be possible, such as intragranular cleavage (Fig. 5a) or intergranular fracture (Fig 5b). In fact, in many cases fracture may initiate as ductile microvoid growth type

fracture, and transition to brittle cleavage as the crack grows [3]. Thus, appropriate models need to be chosen for a given situation. For most ductile structural components, without sharp cracks or flaws, fracture typically initiates due to microvoid growth, and the CVGM may be appropriate for such situations.

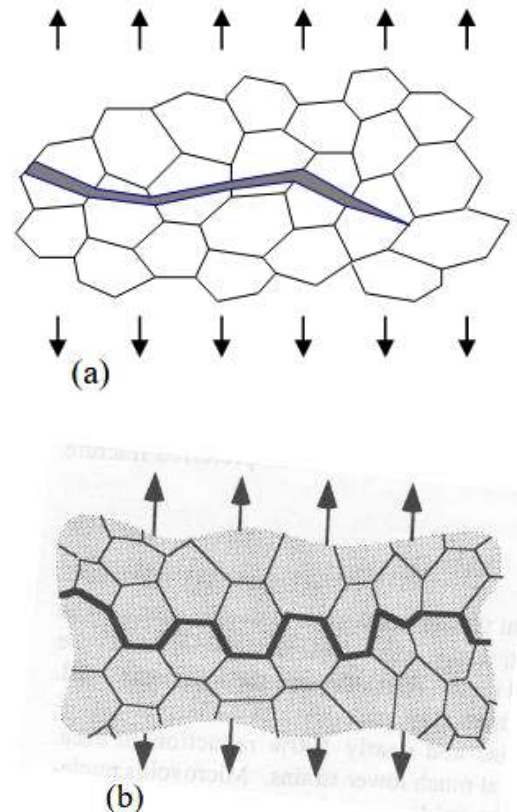


Figure 5. Other mechanisms of fracture – (a) Intragranular cleavage and (b) Intergranular fracture– adapted from Anderson 1995 [2]

Thus, while the micromechanics-based models offer an attractive and physics-based approach to predicting ULCF, they also require more sophisticated modeling of many physical phenomena and knowledge of potential micromechanisms of failure. Moreover, for sharp crack type situations, where the stress gradients are high, these methods typically require characterizing stresses and strains with a high spatial resolution, often requiring significant computational resources. However, given the cost of experimentation, and the decreasing cost of

computational technology, these approaches will likely become more widespread in the future.

## 8. SUMMARY

This paper reviews various methods to predict earthquake-induced fracture in steel structures, and presents the physics-based micromechanical approach as a general, accurate and viable approach. Earthquake-induced fracture in structures is an important limit state, often controlling the ductility of the structural system. Unlike high-cycle fatigue or low-cycle fatigue observed in bridges or mechanical components that are subjected to thousands or millions of cycles, earthquake-induced Ultra-Low Cycle Fatigue (ULCF) is characterized by a very small number ( $<10$ ) of random, high amplitude cycles. However, fundamental approaches to predict ULCF in steel structures are not well developed.

Traditional models to characterize earthquake-induced fracture have relied on experimental or empirical approaches, or on adaptation of techniques originally developed for other problems (such as high-cycle fatigue). Consequently, predictions from these models cannot be generalized to components and situations beyond those that are experimentally tested. Moreover, these costly approaches do not provide insights into local effects that are responsible for fracture. More recently, Conventional Fracture Mechanics (CFM) methods have been used to assess the fracture susceptibility of structural components. While an improvement over experiment-based methods, the CFM methods are limited by assumptions of small-scale yielding and monotonic loading that are not typical to ductile details subjected to earthquake-type ULCF.

Physics-based models that simulate the fundamental micromechanics of the fracture- ULCF process are presented as an attractive alternative to traditional methods. These are fracture criteria based on continuum stress and strain quantities, and thus can be applied to a variety of structural details once the material properties are calibrated. The Cyclic Void Growth Model (CVGM), presented in this paper is one such model that simulates the micromechanical processes of cyclic void growth, collapse and damage

to predict ULCF initiation. The application of the CVGM model requires the calibration of two material parameters. This is done through fairly economical small scale notched bar cyclic tests. A procedure for predicting ULCF initiation based on CVGM is outlined, and validation experiment results are presented which suggest that the CVGM simulates fundamental material behavior and can be applied in a general sense to a wide variety of structural components and configurations.

However, being highly dependent on the accurate characterization of local stress and strain histories, these micromechanical models require the simulation of other physical processes such as global and local buckling, contact, gapping etc. Also important are aspects such as the spatial gradients and statistical variability in material properties.

Moreover, these models are typically focused on a single micromechanism, so multiple models (e.g. addressing void growth, cleavage) may need to operate simultaneously for an accurate simulation.

It is important to note that micromechanics-based earthquake-induced fracture prediction approaches are relatively recent, and need refinement to be widely accepted.

However, given their fundamental appeal, flexibility and generality, coupled with the research community's shift towards model-based simulation, they may be a viable alternative to experimental approaches in the future.

## Acknowledgments

A true friend accepts who you are, but also helps you become who you should be. I do appreciate my wife who is my real true friend.

## References

- [1] ABAQUS, Abaqus User Manual, 1998.
- [2] Anderson, T.L, Fracture Mechanics, 2nd Ed., CRC Press, Boca Raton, FL. 1995.
- [3] Beremin, F.M. "A local criterion for cleavage fracture of a nuclear pressure vessel steel" Metallurgical Transactions A. Vol. 14, 1983, 2277–2287.



- [4] Chi. W-M. "Prediction of steel connection failure using computational fracture mechanics," Ph.D. Thesis, Stanford University, Stanford, CA. 2000.
- [5] Chi. W-M, Kanvinde, A.M., and Deierlein, G.G. "Prediction of Ductile Fracture In Welded Connections Using the SMCS Criterion," *Journal of Structural Engineering*, ASCE, Vol. 132(2), 2006, 171-181.
- [6] Coffin, L. F., Jr., "A Study of the Effects of Cyclic Thermal Stresses on a Ductile Metal," *Trans. ASME*, Vol. 76, 1954, 931-950
- [7] El-Tawil, S., Vidarsson, E., Mikesell, T., and Kunnath, K. "Inelastic behavior and design of steel panel zones," *Journal of Structural Engineering*, ASCE, Vol. 125(2). 1999. 183-193.
- [8] Fell, B.V., Kanvinde, A.M., Deierlein, G.G., Myers, A.T., and Fu, X "Buckling and fracture of concentric braces under inelastic cyclic loading," *SteelTIPS*, Technical Information and Product Service, Structural Steel Educational Council. 2006.
- [9] FEMA (2000), "Recommended Design Criteria for New Steel Moment-Frame Buildings FEMA- 350," Federal Emergency Management Agency, July 2000.
- [10] Hancock, J. W. and Mackenzie, A. C. "On the mechanics of ductile failure in high-strength steel subjected to multi-axial stress-states," *Journal of Mechanics and Physics of Solids*, Vol. 24(3), 1976, 147-169
- [11] Hancock, J.W., and Brown, D.K.. "On the role of strain and stress state in ductile failure," *Journal of The Mechanics and Physics of Solids*, Vol. 31(1), 1983, 1-24.
- [12] Johnson, G.B., Cook, W.H.. "Fracture characteristics of three metals subjected to various strains, strain rates, temperatures and pressures," *Engineering Fracture Mechanics*, Vol. 21(1). 1985. 31-48.
- [13] Kanvinde, A.M., PI, Deierlein, G.G., co-PI "Large scale testing and micromechanical simulation of ultra low cycle fatigue cracking in steel structures" NSF-NEESR award 0421492.
- [14] Kanvinde, A. M. and Deierlein, G.G. "Micromechanical Simulation of Earthquake Induced Fracture in Steel Structures," Technical Report 145, John A. Blume Earthquake Engineering Center, Stanford University, CA. 2004.
- [15] Liu, Z., and Goel, S.C. "Cyclic Load Behavior of Concrete-Filled Tubular Braces." *Journal. Of Structural Engineering*. ASCE, Vol. 114 (7), 1988, 1488-1506
- [16] Okazaki, T., Engelhardt, M., Nakashima, M., and Suita, K. "Experimental Performance of Link to Column Connections in Eccentrically Braced Frames." *Journal of Structural Engineering*, ASCE, Vol. 132(8), 2006, 1201-1211.
- [17] Panontin, T. L. and Sheppard, S. D. "The relationship between constraint and ductile fracture initiation as defined by micromechanical analyses," *Fracture Mechanics: 26th Volume. ASTM STP 1256*. 1995. 54-85.
- [18] Pineau, A. "Development of the Local Approach to Fracture over the last 25 years: Theory and Application." *International Journal of Fracture*, Vol. 138, 2005, 139-166.
- [19] Rice, J. R. and Tracey, D. M. "On the ductile enlargement of voids in triaxial stress fields," *Journal of the Mechanics and Physics of Solids*, Vol. 35. 1969. 201-217
- [20] Stojadinovic, B., Goel, S., and Lee, K.H. "Development of post-Northridge steel moment connections." *Proceedings of the 12th World Conference on Earthquake Engineering*, New Zealand, paper 1269. 2000.
- [21] Tatsuo, E., Koichi, M., Kiyohumi, T., Kakuichi, K., Masanori, M. "Damage evaluation of metals for random of varying loading – three aspects of rain flow method." *Journal of the Institution of Water Engineers and Scientists*, 1974. 371-380
- [22] Tremblay, R., Archambault, M-H, Filiatrault, A. "Seismic performance of concentrically braced steel frames made with rectangular hollow bracing members." *Journal of Structural Engineering*, ASCE, Vol. 129(120). 2003. 1626-1636.
- [23] Uang, C.M and Fan, C.C, "Cyclic Stability Criteria for Steel Moment Connections with Reduced Beam Section," *Journal of Structural Engineering*, ASCE, Vol. 127(9) 2001, 1021-1027.
- [24] Uriz, P., and Mahin, S., (2004). "Seismic Performance Assessment of Concentrically Braced Steel Frames." *Proceedings of the 13th World Conference on Earthquake Engineering*, Vancouver, Canada, 2004.





# Investigating the effectiveness of fluid viscous damper in reducing the effect of seismic sequence on steel bending frame designed on type c soil

Javad Pourali <sup>a\*</sup>

<sup>a</sup>*School of Civil Engineering, Higher Education Institute of Tabari, Babol, Iran*

**Journals-Researchers use only:** Received date: 2023.02.20; revised date: 2023.03.15; accepted date: 2023.03.20

---

## Abstract

Aftershocks can always cause the collapse of structures damaged by the main earthquake. In this article, the seismic performance of an 8-story steel bending frame designed in c-type soil was first subjected to the seismic sequence of an earthquake and an aftershock, and then the same building with the addition of a fluid viscous damper (Fluid Viscous Damper) was evaluated. The results showed that the seismic performance of the studied frame under the effect of severe aftershocks with the presence of a liquid viscous damper is very different from the case without FVD. For example, the maximum displacement of the structural floors was reduced by 60% compared to the case without a damper. It was also found that while most of the aftershocks in buildings without dampers cause a significant increase in the permanent displacement of the roof, in the presence of dampers, this amount has decreased significantly, although in general, the damage caused by the effect of aftershocks on the building is much more as it will be from a state in which the structure is only subjected to the main earthquake © 2017 Journals-Researchers. All rights reserved. (DOI: <https://doi.org/10.52547/JCER.5.2.46>)

**Keywords:** Aftershock, Mainshock; Seismic sequence; Steel moment frame; Fluid Viscous Damper

---

## 1. Introduction

The earthquake is a natural phenomenon that has repeatedly horrified man in human history and has destroyed many cities and villages along with severe human and financial casualties. Historical evidence has shown that large earthquakes are often followed by repeated aftershocks and form a sequence of

earthquakes and aftershocks. Strong aftershocks can increase the level of damage to structures with new damage and may also cause weakening or collapse of structures that were previously damaged under the main earthquake. )But, due to the short time between the occurrence of the aftershock and the main earthquake, they have not been repaired yet([1]. An example of this is the main earthquake in Chile on February 27, 2010 ( $M_w = 8.8$ ), which caused severe

---

\* Corresponding author. Tel.: +98-9116189500; e-mail: j.pourali66@gmail.com.

damage to the southern and central regions of Chile with 360 aftershocks with a magnitude of more than 5 between February 27 and April 26. Among these aftershocks were 21 magnitudes greater than 6 [10]. The first analytical study on the nonlinear behavior of single-degree-of-liberty (SDOF) systems exposed to the time-history records of the 1972 Managua Post-Earthquake was conducted by Mahin (1980). He observed that displacement demand ductility (the ratio of maximum inelastic displacement to system yield displacement) in elastoplastic SDOF systems at the end of the main aftershock increases slightly relative to the original earthquake. Mahin examined the effects of this sequence on structures by setting two records of major earthquake and aftershock. This had one major drawback; it did not take into account the effects of the system's free vibration on the distance between the main earthquake and the aftershock. In subsequent studies, a time interval between the main earthquake and the aftershock was considered and it was assumed that at this distance the system would stop moving. Later, some other researchers used a distance of 20 to 100 seconds in their research depending on the type of structures [4,5]. In fact, this time interval is considered only to end the free vibration time of the system, which by examining the behavior of the structures studied in this study, 40 seconds was found to be a suitable number. Figure 1 shows a schematic of how earthquake and aftershock acceleration maps are placed one after the other.

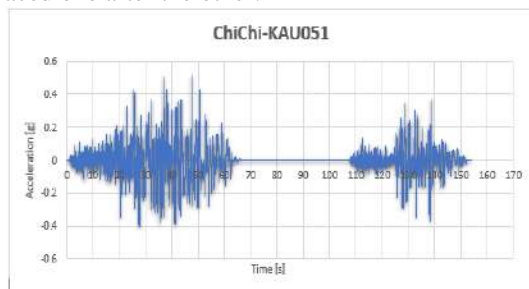


Figure 1. How to place the acceleration of earthquake and aftershock

Garcia (2012) examined the characteristics of a wide range of earthquakes and corresponding aftershocks on the seismic response of buildings and showed that the dominant period, as well as the duration of the main earthquake and aftershocks, were

statistically weakly correlated. Therefore, the production of artificial seismic sequences from the main earthquake as a basis for the production of aftershocks, even with a smaller amplitude, does not make sense because the frequency and duration of the earthquake are completely different [9]. Therefore, it can be said that it is necessary to use real data to evaluate the performance of existing structures under seismic sequences. Abdollahzadeh et al. (2017) with the help of real seismic sequences and by examining the energy distribution in buildings designed by conventional elastic methods as well as modern plastic design methods based on performance, found that aftershocks have a destructive effect on floors that suffer more damage under the main earthquake. Have seen will have [9]. Recently, several researches have been conducted in the field of seismic evaluation of structures under seismic sequences, in all of which the effect of aftershock in increasing the vulnerability of the structure has been confirmed [10,11]. However, design codes still do not explicitly consider the effects of aftershocks and the cumulative damage caused by them in the design of earthquake-resistant structures. The reason for this is probably due to the many uncertainties in the capacity of structures damaged after the main earthquake, the complexity of aftershock characteristics and the probability of their occurrence and the general lack of system fragility models to evaluate the performance of structures [2, 12].

## 2. Modeling

To evaluate the vulnerability of MDOF structures (several degrees of freedom) under the effect of earthquake and aftershock sequence, an 8-story building in Tehran of medium steel bending frame type in types (C) of soil based on LRFD method Article 10 of the National Building Code and the fourth edition of Standard 2800 [6] were designed. These structures have three openings of 5 meters in each direction and the height of the floors is 3.2 and the height of the parking lot is 2.7. First, the design of this building was done according to the residential use and located on a relatively high-risk area according to the definition of 2800 standard with the help of ETABS software. Then, for two-dimensional analysis

of the critical frame, the selection and seismic performance of this frame were evaluated using time history analyzes by applying natural earthquake and

aftershock records using OpenSees finite element software. Figure 3 shows the three-dimensional and two-dimensional views of the designed frame.

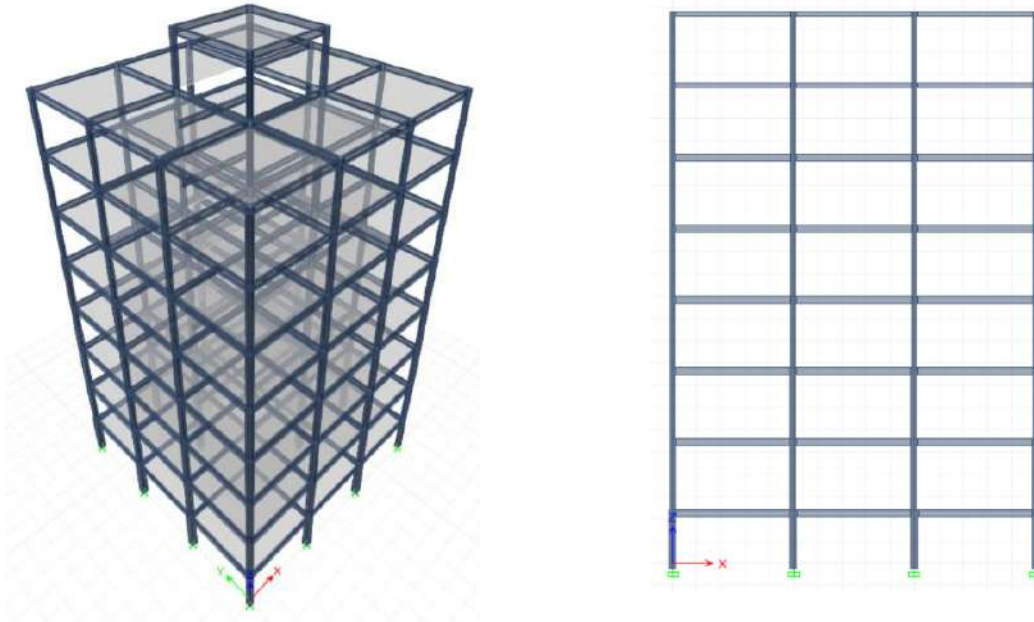


Figure 2 and 3. Three-dimensional and two-dimensional view of the designed frame

In the definition of steel, non-linear materials (steel02) in the OpenSees material library were used and the cross-section of the members was made of fiber. This command separates the cross section into smaller areas and summarizes the stress-strain response of the materials for these areas to obtain the resultant behavior. Tables 1 and 2 provide a list of sections designed in the critical frame.

Table 1

List of designed section (Type C soil)

Columns	Beams
BOX180X8	PG-W180X6-F150X8
BOX200X8	PG-W180X6-F150X15
BOX200X10	PG-W300X6-F150X10
BOX200X12	PG-W300X6-F150X12
BOX240X10	PG-W300X6-F150X15
BOX240X12	PG-W300X6-F150X20
BOX240X15	
BOX240X20	
BOX300X20	
BOX180X8	

### 2.1. Fluid viscous damper

Fluid Viscous Damper systems are hydraulic equipment that is used to dissipate kinetic energy caused by seismic vibrations or to deal with impacts between structures. These equipments are diverse and can be designed in such a way that they absorb the desired load (for example, earthquake and wind loads), but allow the structure to move freely against other conditions such as heat-induced movements. FVD typically consist of a piston head with orifices contained in a cylinder filled with a highly viscous fluid, usually a compound of silicone or a similar type of oil. Energy is dissipated in the damper by fluid orifice when the piston head moves through the fluid. The fluid in the cylinder is nearly incompressible, and when the damper is subjected to a compressive force, the fluid volume inside the cylinder is decreased as a result of the piston rod area movement. A decrease in volume results in a restoring force. This undesirable force is prevented by using an accumulator. An

accumulator works by collecting the volume of fluid that is displaced by the piston rod and storing it in the makeup area. As the rod retreats, a vacuum that has been created will draw the fluid out. A damper with an accumulator is illustrated in Fig. 4[7].

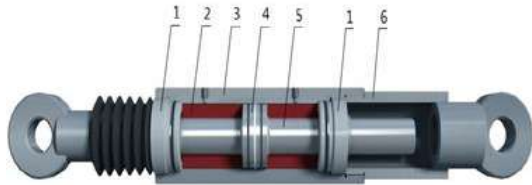


Figure 4. Fluid viscous dampers (FVD).

1-end cover; 2-damping medium; 3-cylinder block; 4-piston; 5-piston rod; 6-connector

### 2.1.1. Characteristics of fluid viscous dampers

FVD are characterised by a resistance force  $F$ . It depends on the velocity of movement, the fluid viscosity and the orifices size of the piston. The value of  $P$  is given by the relationship.

$$P = C_d (\dot{U}d)^\alpha \sin(\dot{U}d)$$

with

$$U_d(t) = U_0 \sin(\omega \cdot t)$$

Where

$U \cdot d$  is the velocity between two ends of the damper;

$C_d$  is the damping constant;

$U_0$  is the amplitude of the displacement,

$\omega$  is the loading frequency, and  $t$  is time;

$\alpha$  is an exponent which depends on the viscosity properties of the fluid and the piston.

The value of the constant  $\alpha$  may be less than or equal to 1. Figs. 5 and 6 show the force velocity and the force displacement relationships for three different types of FVD. They characterise the behaviour of the viscous damper. With  $\alpha = 1$  the device is called linear viscous damper and for  $\alpha < 1$  non-linear FVD which is effective in minimising high velocity shocks. Damper with  $\alpha > 1$  has not been seen often in practical application. The non-linear damper can give a larger damping force than the two other types (Fig. 5).

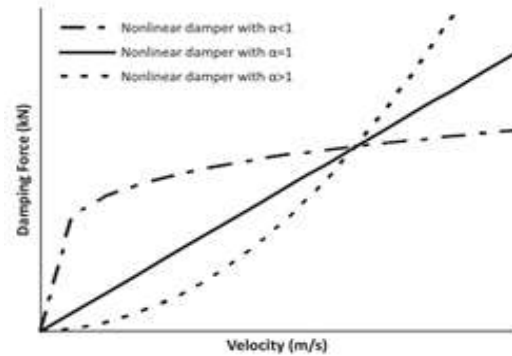


Figure 5. Force velocity relationship of FVD.

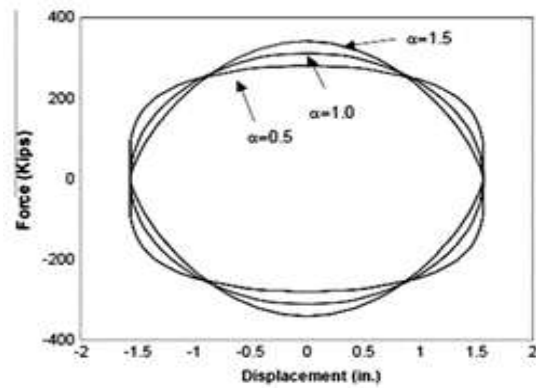


Figure 6. Force displacement relationship of FVD.

Fig. 6 shows that the plot has different shapes for the different values of  $\alpha$ . At the frequency of loading used to create the loops enclosed areas for the different damper are all equal, but the values of the damping coefficient are all different. The resisting force in the FVD,  $P$ , can be described by the following equation:

$$P = K_1 U_d + C_d \frac{dU_d}{dt}$$

Where

$K_1$  is the storage stiffness and  $C$  is the damping coefficient given by

$$C_d = \frac{K_2}{\omega}$$

Where

$K_2$  is the loss stiffness [7]. In the table below, the design specifications of several types of FVD are presented. In this study, the 500 KN model was used.

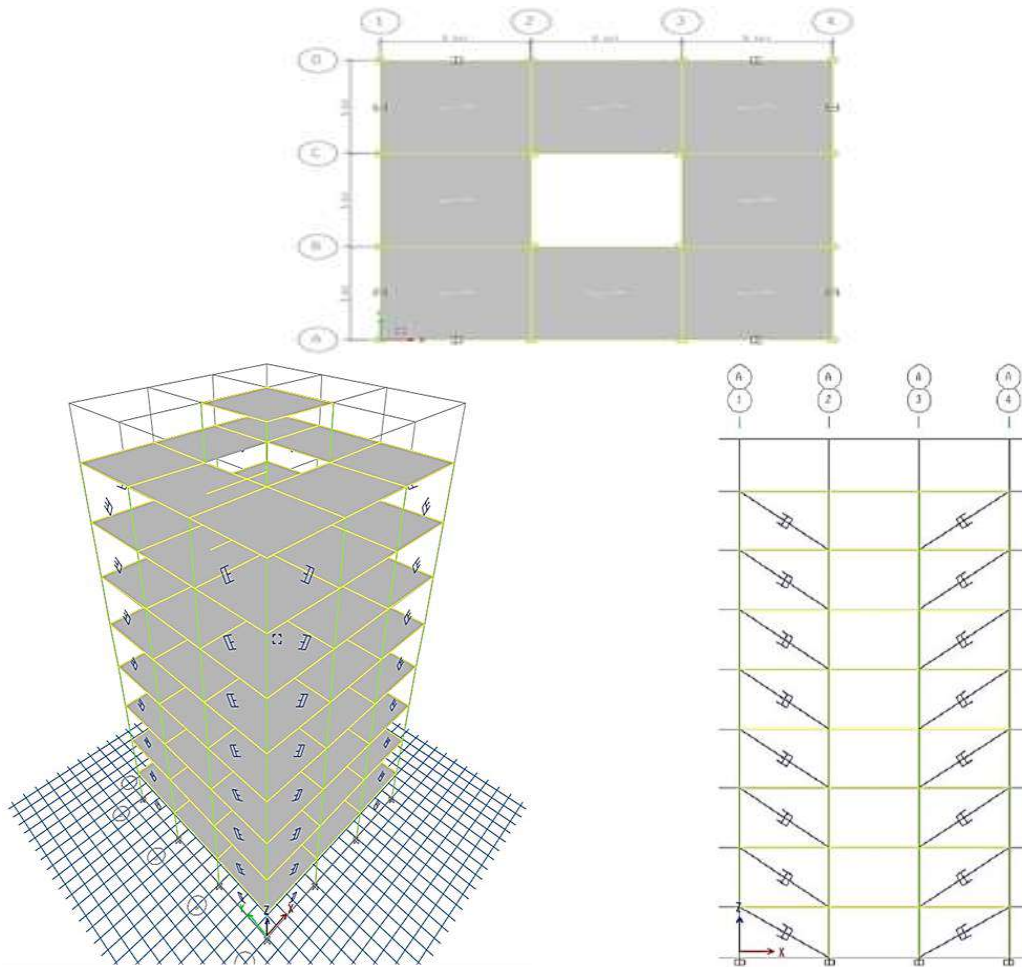


Figure 7. Three-dimensional, plan and two-dimensional view of the designed frame white FVD.

Table 3

FVD with different capacity force (kN)

Force (kN)	Taylor devices model number	Spherical bearing bore Diameter (mm)	Mid-stroke length (mm)	Stroke (mm)	Clevis Thickness (mm)	Maximum clevis width (mm)	Clevis depth (mm)	Bearing thickness (mm)	Maximum cylinder diameter (mm)	Weight (kg)
250	17120	38.10	787	$\pm 75$	43	100	83	33	114	44
500	17130	50.80	997	$\pm 100$	55	127	102	44	150	98
750	17140	57.15	1016	$\pm 100$	59	155	129	50	184	168
1000	17150	69.85	1048	$\pm 100$	71	185	150	61	210	254

Past studies have shown that records must be scaled to the desired hazard level to achieve proper seismic behavior [3]. In this study, 12 raw accelerometers were extracted from PEER site data in accordance with the

soil type and were compared and scaled according to the instructions of the fourth edition of the 2800 standard. Table 3 shows the characteristics of each of



the corresponding earthquake and aftershock accelerometers.

Table 3  
Characteristics of earthquake and aftershock acceleration

Name of earthquake	Station	Magnitude of earthquake	magnitude of the aftershock	Shear wave velocity
HOLISTER	Holister	5.6	5.5	198
Imperial Valley	Holtville	6.53	5.01	202
Northwest	Jiashi	6.1	5.8	240

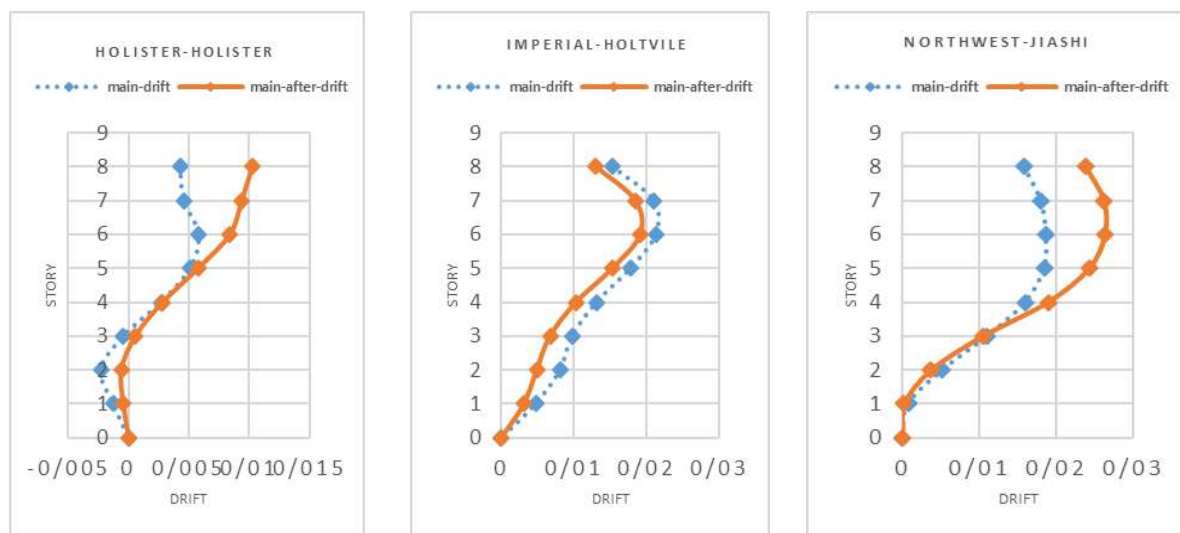
It should be noted that regarding the scale of aftershocks, the adaptation coefficient was used to maintain the PGA ratio of earthquake and aftershock. According to Table 4, the ratio of PGA aftershock to the main earthquake is:

Table 4  
Ratio of PGA aftershock to main earthquake

Name of earthquake					
Northwest-Jiashi		Holister-Holister		Imperial-Holtville	
PGA after / PGA ma	0.873402	PGA after / PGA ma	-	PGA after / PGA ma	-
			0.61133		0.44463

### 3. Comparison of floor drift distribution

The frames are exposed to the seismic sequences of the accelerometers presented in Table 3 under time history analysis, and the drift changes of the classes in height are shown in Figures 1. As can be seen from the diagrams related to the drift of the floors, the aftershock in some cases leads to a strong increase in the drift of the structure, and in some cases, the aftershock did not have much effect on the main structure, which is justified due to the very small intensity of the aftershock in the earthquake. Therefore, the main damage occurs during the main earthquake. However, according to the 2800 standard guidelines, if these three records are selected for design, maximum results should be used. Therefore, it is observed that aftershocks can have very destructive effects (increasing displacement up to more than double) that ignoring these effects in the design process can have catastrophic consequences during an earthquake. Another issue that seems to be important is the change of drift direction. This change in drift direction may cause severe damage to the structure, and it is possible that the structure will not be able to withstand such a deformation during severe earthquakes.



Graphs 1. Type C soil drift change diagrams

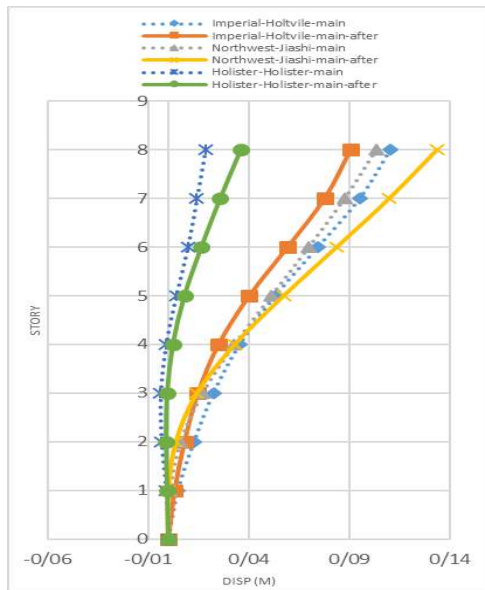


Figure 8. Permanent displacement diagrams whitout FVD.

#### 4. Comparison of permanent displacement distribution of floors

Examining the drift distribution of floors at the collapse level of the damaged structure, it was found that with the increase of damage under the main earthquake, the distribution of damage is more concentrated in the same floors damaged in the main earthquake, while the same record in a healthy structure causes the failure of another floor. Comparison of permanent displacement distribution of floors. Finally, the remaining displacement of the elements in both healthy and damaged structures is investigated. The parameter of relative displacement, which is considered as a good representative for damage to structural members, also strongly depends on the type of damage caused by the main earthquake. The drift changes of the floors in the

Table 4

Ratio of displacement ratio of the structure under the effect of the seismic sequence in comparison with the main earthquake In type C soil								
Record name	floors							
	ST8	ST7	ST6	ST5	ST4	ST3	ST2	ST1
Imperial-Holtville	0.82	0.82	0.80	0.76	0.71	0.66	0.63	0.67
Northwest-Jiashi	1.29	1.25	1.20	1.12	1.01	0.85	0.65	0.19
Holister-Holister	1.94	1.81	1.70	2.09	-1.78	0.13	0.30	0.36

primary and damaged structures in different soil types are shown in Figures 8 to 12. As can be seen from Figures 8 to 12, the permanent displacement of the roof under the effect of seismic sequence is sometimes less than the permanent displacement of the roof under the effect of the main earthquake alone. This phenomenon expresses the important issue that aftershocks do not necessarily increase the permanent displacement of the structure. In examining the permanent displacement of the roof, it should be noted that the structure may not stop at its maximum permanent displacement due to successive earthquakes and as a result have less permanent displacement, although in this case, the damage to the structure has increased.

#### 5. Conclusion

To evaluate the response of steel MDOF structures under the effects of seismic sequencing, an 8-story building with medium Steel moment system in types C of soil was designed according to version 4 of 2800 standard by LRFD method. Then the same building was designed with the addition of Fluid Viscous Damper (FVD) It was subjected to seismic sequence of earthquake and aftershock. Then, the most critical frame of each structure was selected for modeling in opensees software and finally, the performance of steel bending frames was investigated through applying natural records of an original earthquake and scaled aftershock according to standard criteria 2800 in terms of maximum relative –

Table 5

Direction	MAX Story displacement	
	EX	EY
Without FVD	265.93 mm	219.07mm
With FVD	74.371mm	73.625mm
Reduction rate%	%72	%66



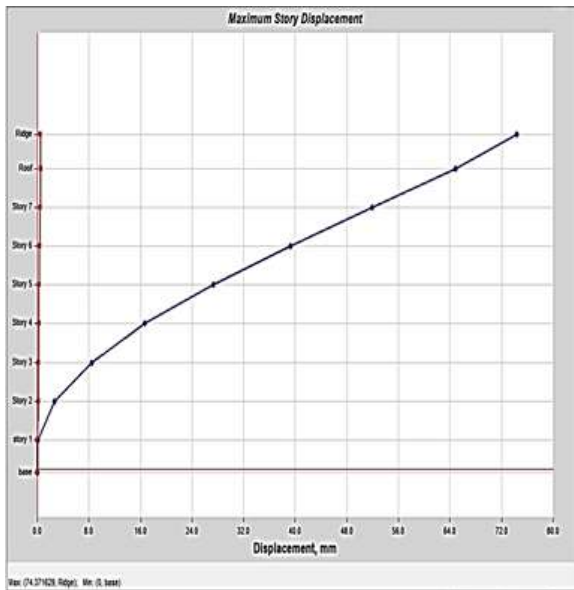


Figure 9. Max displacement whit FVD. -EX

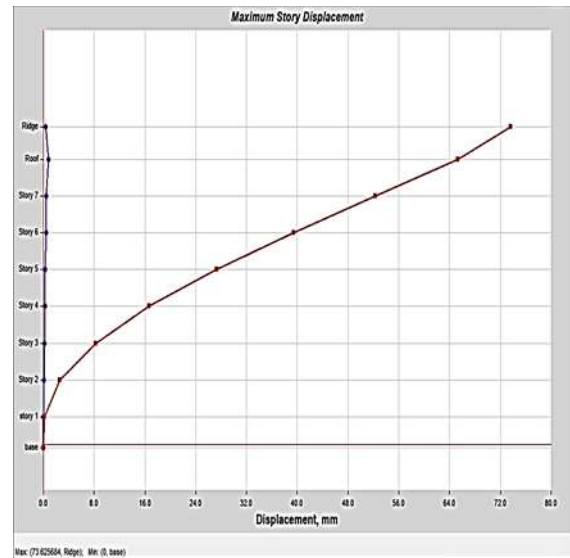


Figure 10. Max displacement whit FVD. -EY

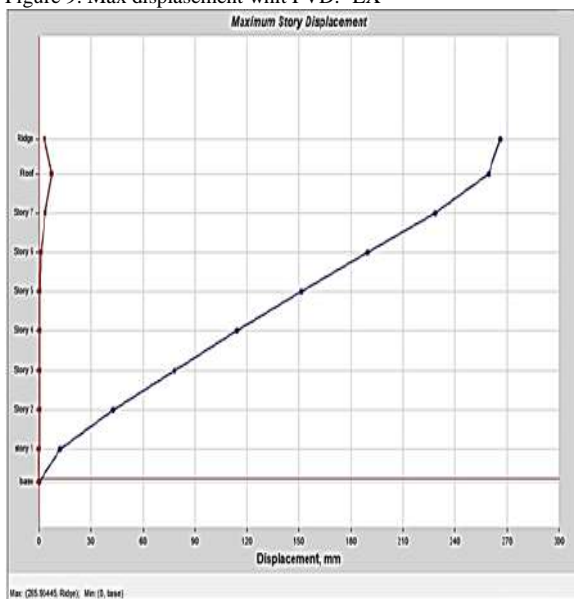


Figure 11. Max displacement whitout FVD. -EX

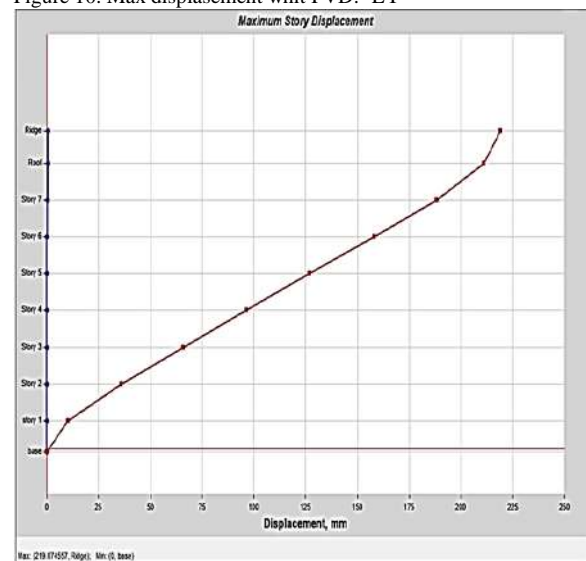


Figure 12. Max displacement whitout FVD. -EY

displacement within the floor and relatively lasting displacement which is considered as a good representative for structural organ damage and the following results were obtained.

1- The results showed that the seismic performance of the studied frame under the effect of severe aftershocks with the presence of a liquid viscous damper is very different from the case without FVD. For example, the maximum displacement of the structural floors was reduced by 60% compared to the

case without a damper. It was also found that while most of the aftershocks in buildings without dampers cause a significant increase in the permanent displacement of the roof, in the presence of dampers, this amount has decreased significantly, although in general, the damage caused by the effect of aftershocks on the building is much more as it will be from a state in which the structure is only subjected to the main earthquake.

2- Comparing the residual displacement of the elements in the two healthy and damaged structures, it was found that the residual displacement in the damaged structure is strongly dependent on the type of damage caused in the main earthquake. In fact, depending on the category of damage caused by the earthquake to the healthy structure, the focus of damage in the damaged structure has changed. This result can be seen due to the shape of the behavioral curves for structures with different percentages of damage. In some stimuli, there was no significant difference between the behavior of damaged and healthy structures.

3- By examining the drift distribution of floors in the collapse level of the damaged structure, it was found that with the increase of damage under the main earthquake, the distribution of damage is more concentrated in the same damaged floors in this earthquake, while the same record in a healthy structure causes damage in another floor.

## References

- [1] G. yeo & A. Cornell S(2005)"stochastic Characterization and Decision Bases under Time-Dependent Aftershock Risk in Performance-Based Earthquake Engineering", PEER report.
- [2] Nazari. N, De Lindt.W, Li.Y,(2015)"Quantifying Changes in Structural Design Needed to Account for Aftershock Hazard", Journal of Structural Engineering.
- [3] Kiani, J. and Khanmohammadi M. (2015). New approach for selection of real input ground motion records for incremental dynamic analysis (IDA). Journal of Earthquake Engineering 19, no. 4: 592-623.
- [4] Mahin SA. (1980) Effects of duration and aftershocks on inelastic design earthquakes. In: Proceedings of the seventh world conference on earthquake engineering. vol. 5. p. 677-9.
- [5] Fragiocomo M, Amadio C, Macorini L. (2004) Seismic response of steel frames under repeated earthquake ground motions. Eng Struct;26:2021-35.
- [6] Earthquake Design Regulations, Standard 7, Edition 4, Building and Housing Research Center, Journal No. Z-1, First Edition 2014
- [7] A. Ras, N. Boumechra, Seismic energy dissipation study of linear fluid viscous dampers in steel structure design, Alexandria Eng. J. (2016),
- [8] Ruiz-Garcia J. Mainshock-aftershock ground motion features and their influence in building's seismic response. Journal of Earthquake Engineering 2012; 16(5):719-37.
- [9] Abdollahzadeh G.R., Mohammadgholipour A., Omranian E. (2017). Seismic evaluation of steel moment frames under mainshock-aftershock sequence designed by elastic design and PBPD methods Journal of Earthquake Engineering, (accepted).
- [10] Banon, H.,J.M.Biggs, and H.M.Irvine.."seismic Damage of Reinforced Concrete Frames." Journal of the structural Division,ASCE 107 (ST9) 1713-1729-1981
- [11] Hosseinpour F., and Abdelnaby A. E. (2017). Fragility curves for RC frames under multiple earthquakes. Soil Dynamics and Earthquake Engineering 98: 222-234.
- [12] Omranian E, Abdelnaby A. E., Abdollahzadeh Gh.R, Rostamian M., Hosseinpour F., Fragility Curve Development for the Seismic Vulnerability Assessment of Retrofitted RC Bridges under mainshock-aftershock seismic sequences, Structures Congress 2018 (accepted).
- [13] Abdelnaby, A. E.(2012)"Multiple earthquake effects on degrading reinforced concrete structures." Doctoral dissertation, Univ. of Illinois, Urbana-Champaign, IL.



# Evaluation of effective operation parameter on High Efficiency Particulate Air and Ultra Low Particulate Air filters

Seyed Mohammad Hosseini<sup>a\*</sup>, Sepideh Sahebi<sup>a</sup>

<sup>a</sup> Mazandaran Science and Technology Park, Shirozhan Sq., Sarikenar St., Sari, Mazandaran, Iran

**Journals-Researchers use only:** Received date: 2023.03.29; revised date: 2023.04.15; accepted date: 2023.05.06

## Abstract

The particle penetration removal efficiency of the High Efficiency Particulate Air (HEPA) and Ultra Low Particulate Air (ULPA) filters were studied by using of mono-disperse liquid aerosols of Di-Octyl Phthalate (DOP) under vary operational conditions. The effects of different operational factors, including the particle size, the face velocity and pressure drop were investigated in this study. The results indicated that the most penetrating particle size through the ULPA and HEPA filters was approximately 0.1-0.12  $\mu\text{m}$ . Brown diffusion effect is suggested mechanism for particle size removal mechanism of 0.1  $\mu\text{m}$  and less while impaction and interception mechanisms are explained the behavior of HEPA and ULPA filters for removal of 0.12  $\mu\text{m}$  and more particle size. The penetrations of particle through both kind of filters were increased with increasing of face velocity. Additionally, the pressure drop of filter is increased versus the rising of face velocity. The cost of energy is lower in low face velocity of filters. © 2017 Journals-Researchers. All rights reserved. (DOI: <https://doi.org/10.52547/JCER.5.2.55>)

**Keywords:** HEPA; ULPA; Filtration; Efficiency

## 1. Introduction

HEPA filter is an extended-medium, dry-type filter in a rigid frame which is widely used in nuclear, microelectronic, pharmaceutical and food industries [1]. The filter is used either to treat polluted air before it is released into the environment or to admit air with very low dust concentration into a process. ULPA is a kind of super effective filter with a removal efficiency of over 99%, capable of absorbing and filtering particulates and dusts in air as smaller as 0.01  $\mu\text{m}$  [2].

The quality of filter is a function of particle collection efficiency and pressure which is defined by Equation 1, which is ratio of fractional capture per unit thickness (E) inside the filter to pressure drop over the unit thickness ( $\Delta P/t$ ) [3].

$$qf = \frac{E}{\Delta P/t} = \frac{\ln(\frac{1}{P_n})}{\Delta P} \quad (1)$$

where  $P_n$  is the penetration and t are the thickness of the filter medium.

\* Corresponding author. Tel.: +989123111147; e-mail: envhosseini@gmail.com.

The collection efficiency depends on the structure of the filters like porosity, fiber diameter and filter thickness, the operational conditions such as filtration velocity, temperature, humidity and aerosol characteristics such as particle density and size [4], [5].

The effect of particle size and concentration and gas flow velocity on particle collection efficiency of filter was assessed in some studies. The filter collection efficiency of homogeneous fibrous media is calculated by Eq. (2) [6].

$$E = 1 - \exp\left(-\frac{4\alpha Z\eta}{\pi(1-\alpha)d_f}\right) \quad (2)$$

Where E: filter collection efficiency,  $\alpha$ : packing fraction, Z: filter thickness,  $\mu\text{m}$ ,  $\eta$ : single fiber collection efficiency,  $d_f$ : fiber diameter  $\mu\text{m}$ .

The single fiber collection efficiency,  $\eta$  is expressed as a function of the efficiencies calculated for each of the different capture mechanisms considered for a single fiber. These mechanisms are direct interception, inertial impaction and Brownian diffusion. A simple general approach, described by Kasper, Preining, and Matteson and Brown is to assume that the aforesaid mechanisms act independently [7]. Making this assumption, a fraction  $(1 - \eta_d)$  of particles would escape capture by Brownian diffusion if this mechanism acted alone. If the capture of particles is also subjected to the other mechanisms, a fraction  $(1 - \eta_d)(1 - \eta_i)(1 - \eta_r)$  will escape capture by these different mechanisms. This means that the total single fiber collection efficiency can be calculated as follows (Kasper, Preining, & Matteson, 1987):

$$\eta = 1 - (1 - \eta_d)(1 - \eta_i)(1 - \eta_r) \quad (3)$$

Where:  $\eta_d$  is diffusion single fiber efficiency,  $\eta_i$  is inertial single fiber efficiency and  $\eta_r$  is interception single fiber efficiency (Figure 1).

Diffusion of extremely small, submicron particles is a result of Brownian motion. These particles are so small and the number of collisions with air molecules is low. Particles are moved from one gas streamline to the next by random motion. Diffusion mechanisms could be an effective collection mechanism under sufficient contact time and proper distance to the target [6].

Interception is a mechanism in which there is particles of roughly 0.1 to 1-micron diameter that are

carried by the gas streamline with sufficiently close to the surface of the fiber. These particles have insufficient inertia to leave the gas streamline and are carried with the streamline [6].

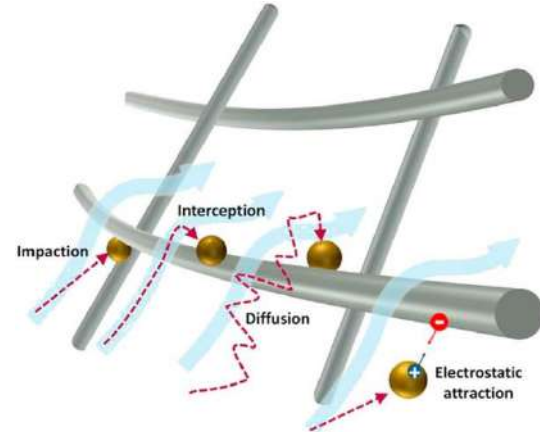


Figure 1 Basic particle collection mechanisms [8]

The diffusion and direct interception efficiencies,  $\eta_d$  and  $\eta_r$ , can be calculated by Eq. (4) and (5) respectively [9]. In these equations, the parameters  $C_d$  and  $C_r$  were later included by Liu and Rubow [10] to account for the slip flow effect.

$$\eta_d = 1.6 \left( \frac{\varepsilon}{Ku} \right)^{1/3} Pe^{-2/3} C_d \quad (4)$$

$$\eta_r = 0.6 \left( \frac{\varepsilon}{Ku} \right) \frac{R^2}{(1+R)} C_r \quad (5)$$

$$C_d = 1 + 0.388 K n_f \left( \frac{\varepsilon Pe}{Ku} \right)^{1/3} \quad (6)$$

$$C_r = 1 + \frac{1.996 K n_f}{R} \quad (7)$$

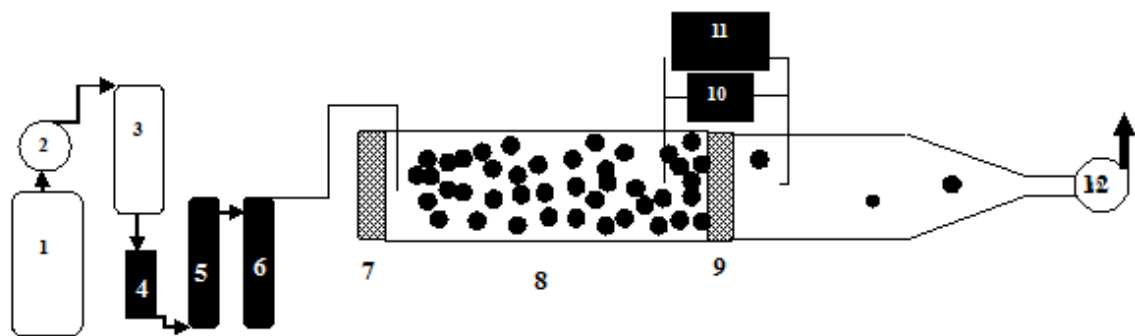
In these equations  $Pe$ ,  $K_{nf}$ ,  $R$  and  $Ku$  that are given in following equations, are Peclet number, fiber Knudsen number, interception parameter and Kuwabara number receptively.

In the mechanism called impaction, large particles moving toward the target have mass, and therefore momentum, which causes each particle to travel in a straight line toward the target. The particle leaves the streamline as the streamline bends to move around the

Table 1.

Characteristics of tested filter in the study

No. of filter	Kind of filter	Dimension (L×W×h) cm	Nominal efficiency (%)	Pressure lost (Pa.)
1-6	ULPA	305 × 305 × 150	99.999	220
7 -9	HEPA	305 × 305 × 150	99.997	180



- (1) compressed air                      (2) Pressure regulator                      (3) High efficiency drier                      (4) High efficiency filter  
 (5) Constant Output Atomizer                      (6) Evaporation-Condensation aerosol conditioner  
 (7) ULPA filter                      (8) Test Tunnel                      (9) test filter                      (10) micro manometer  
 (11) CNC                      (12) Fan                      (13) Air out put

Figure 2. diagram of the Setup for this study

target. The greater mass of the particle, the more likely that it will travel in a straight line. Also, as the velocity difference between the particle and the target increases, the particle will have increased momentum and will be more likely to be carried into the target. Impaction of a fiber can be calculated by [6]:

$$\eta_I = 0.0334STK^{3/2} \left( 1 + 0.0334STK^{3/2} \right)^{-1} \quad (8)$$

Where STK is Stock's Number.

Davies' law describes the pressure drop evolution ( $\Delta P$ ) of a clean fibrous filter with filtration velocity ( $U_0$ ) [5].

$$\frac{\Delta P}{Z} = 64\mu U_0 \frac{\alpha^{3/2} (1 + \alpha^3)}{d_f^2} \quad (9)$$

The aims of this study are experimental evaluation of effective particle collection mechanisms on HEPA and ULPA air filters.

## 2. Materials and Methods

In this study the efficient parameters in collection of particles were tested on 6 HEPA filters and 3 ULPA filters by DOP method (Table 1).

The lists of instruments used in this study are as followed:

1. Compressed air generator: Production of mono size aerosol of DOP needs to 35 PSI and 3.5 liter.
2. High efficiency drier: TSI manufactory and model 3074
3. Constant Output Atomizer: TSI manufactory and model 3076 that can produce aerosols from liquids. In this study DOP was used for production of aerosols.
4. Evaporation-Condensation aerosol conditioner: TSI manufactory and model 3072
5. Test Tunnel: the function of the tunnel is creative a specified air flow rate and defined DOP aerosol concentration. Dimension of the tunnel is length 350 cm, area section  $30 \times 30$  cm. A qualified ULPA filter that install in inlet of tunnel, removed 99.999% of atmospheric particle of entry air into the tunnel.
6. Fan: a fan with 287 rpm can produced air flow 0-600 m<sup>3</sup>/hr.
7. Air flow meter: Air flow manufactory model TA2 that has measured of gas flow rate.
8. Micro manometer: head loss of filters in test condition was determined by micro manometer model AMP 50K, Air Flow manufactory.
9. Condensation Nuclei Counter (CNC): This device is made by TSI manufactory and its model is 3022 A and has ability to count of particles in before and after of filter under test.
10. Impactor: the distribution of generated particle was determined by ten-stage Andersen Impactor that its model was 2740.

DOP was used as particulate matter. The DOP was dissolved in ethyl alcohol. This solution, fed to the aerosol generator, was atomized in the particle-free air. Different particle diameters could be obtained by changing the DOP concentration in the solution. In experimental section of this study, seven particle diameters were produced, including 0.04, 0.07, 0.1, 0.12, 0.3, 0.5, 0.7 and 1 nanometer at a concentration of 107 particles/cm<sup>3</sup>. The diameter of the particles was controlled by Andersen Impactor. The efficiencies of the filters were obtained by counting the particles before and after the filter by using a TSI CNC. The tests were accomplished at gas velocities varying from 1.58 to 4.9 cm/s. Also, the pressure lost through test filter was measured as function of air flow rate. Each test was triplicate.

### 3. Result and Discussion

The filters efficiency was evaluated in 8 gas velocities between 1.58 and 4.9 cm/s. Figure 3 shows typical results of filter efficiency as a function of particle size, at  $U_o = 2.42$  cm/s. It can be noticed that the minimum collection efficiency or maximum penetration for both filters was obtained in dp. 0.12 mic. Diffusion collection mechanisms causes of removing of smaller particle and Interception and Inertia impaction are effective mechanisms for collection of bigger particles.

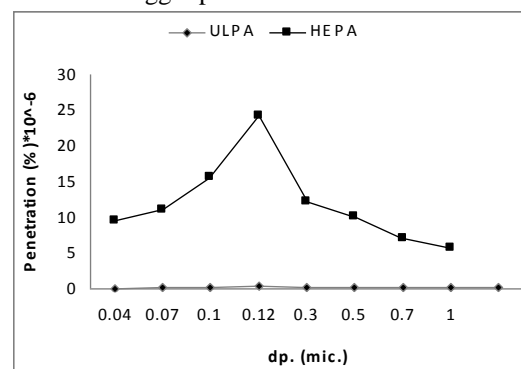


Figure 3. Comparison of penetration of HEPA and ULPA filter as function of particle diameters

As figure 4 and 5 show, the efficiency was decreased with increasing gas velocity. In this study defined conditions, the dp:0.12 mic. has maximum penetration and dp:1 mic. has maximum removal due to increasing of effect of inertia impaction mechanism.

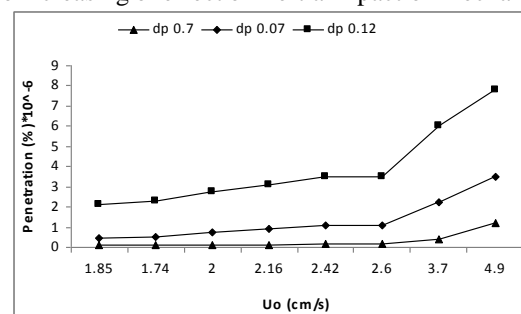


Figure 4. Variation of penetration of filter No 1 as a function of gas velocity for three particle size

As figure 5 shows, increasing of gas velocity from 1.85 cm/s to 4.9 cm/s causes of increasing penetration from  $1.6 \times 10^{-6}$  to  $4.4 \times 10^{-6}$  for dp. 0.12 mic, another

hand if the gas stream velocity will be increases to 264 percent, the penetration increases to 275 percent of initial penetration.

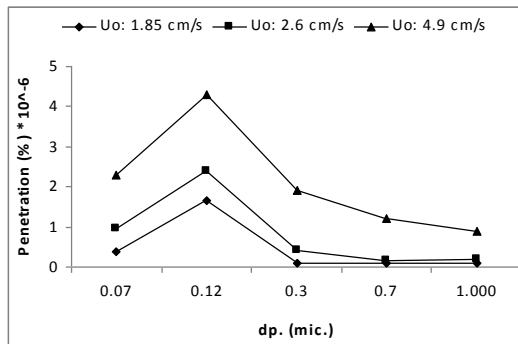


Figure 5. Variation of penetration of filter No 1 as a function of particle size diameter for three gas velocity

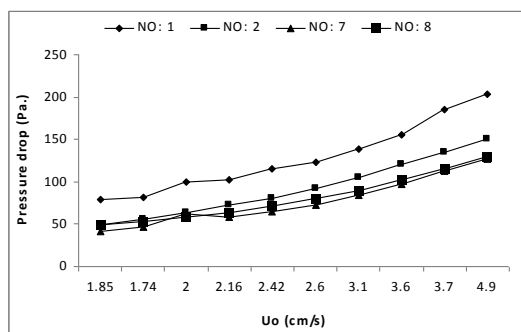


Figure 6. Comparison of variation of pressure drop of HEPA and ULPA filter as a function of gas velocity

Pressure drop of fiber filter directly increase with increasing of gas stream velocity (Eq.9). In this study pressure drop of 4 filters were determined as a function gas stream velocity. Increasing of velocity from 1.58 cm/s to 4.9 cm/s in filter No:1 lead to increasing of pressure drop from 70 pa. to 200 pa. Also, pressure drop in ULPA filter is higher than HEPA.

#### 4. Conclusion

In design of a dedusting projects for industrial or operation of clean room, identification of distribution of particle size and selection of best gas collection velocity are two important data. Although, the removal efficiency of sub-micro particles via ULPA and HEPA

filters are decreased with increasing of gas face velocity, for the particle with bigger than 1.2-micron size, increasing of gas face velocity leads to increasing of removal efficiency. Experimental results of this study show that:

- The penetration of HEPA filter is higher than ULPA filter. For example, penetration of a tested HEPA filter is greater than 55 times to ULPA filter.
- Maximum penetration of the ULPA and HEPA filter is funded in 0.1- 0.12 mic. particle size.
- Penetration of these fiber filters are increased by increasing of gas velocity. For example, increasing of gas velocity from 1.85 cm/s to 4.9 cm/s, lead to increases of penetration from  $1.65 \times 10^{-6}$  to  $4.3 \times 10^{-6}$  percent.
- Pressure drop of filter has direct relationship with gas velocity. For example, decreasing of gas velocity to third of its initial value cause to increase pressure drops to 2.6 time.
- All of experimental results of this study is supported by correlations from the literature.

#### References

- [1] W. Zhang, S. Deng, Y. Wang, and Z. Lin, "Modeling the surface filtration pressure drop of PTFE HEPA filter media for low load applications," *Build. Environ.*, vol. 177, 2020, doi: 10.1016/j.buildenv.2020.106905.
- [2] S. D. Lowther et al., "How efficiently can HEPA purifiers remove priority fine and ultrafine particles from indoor air?," *Environ. Int.*, vol. 144, 2020, doi: 10.1016/j.envint.2020.106001.
- [3] K. M. Lee, Y. M. Jo, J. H. Lee, and J. A. Raper, "Assessment of surface and depth filters by filter quality," *Powder Technol.*, vol. 185, no. 2, 2008, doi: 10.1016/j.powtec.2007.10.013.
- [4] J. Steffens and J. R. Coury, "Collection efficiency of fiber filters operating on the removal of nano-sized aerosol particles: I-Homogeneous fibers," *Sep. Purif. Technol.*, vol. 58, no. 1, 2007, doi: 10.1016/j.seppur.2007.07.011.
- [5] D. Thomas, S. Pacault, A. Charvet, N. Bardin-Monnier, and J. C. Appert-Collin, "Composite fibrous filters for nano-aerosol filtration: Pressure drop and efficiency model," *Sep. Purif. Technol.*, vol. 215, 2019, doi: 10.1016/j.seppur.2019.01.043.



- [6] K. B. Schnelle and C. A. (Charles A. Brown, Air pollution control technology handbook. CRC Press, 2002.
- [7] G. Kasper, O. Preining, and M. J. Matteson, "Penetration of a multistage diffusion battery at various temperatures," *J. Aerosol Sci.*, vol. 9, no. 4, 1978, doi: 10.1016/0021-8502(78)90035-6.
- [8] A. Mamun, T. Blachowicz, and L. Sabantina, "Electrospun Nanofiber Mats for Filtering Applications -Technology, Structure and Materials," Apr. 2021, doi: 10.3390/polym13091368.
- [9] K. W. Lee and B. Y. H. Liu, "Theoretical Study of Aerosol Filtration by Fibrous Filters," *Aerosol Sci. Technol.*, vol. 1, no. 2, pp. 147–161, Jan. 1982, doi: 10.1080/02786828208958584.
- [10] B. Y. . 'Liu and K. L. . 'Rubow, "Efficiency, Pressure Drop and Figure of Merit of High Efficiency Fibrous and Membrane Filter Media," 1990.
- [11] P. Audebert, P. Hapiot, *J. Electroanal. Chem.* 361 (1993) 177.
- [12] J. Newman, *Electrochemical Systems*, 2nd ed., Prentice-Hall, Englewood Cliffs, NJ, 1991.
- [13] A.R. Hillman, in: R.G. Linford (Ed.), *Electrochemical Science and Technology of Polymers*, vol. 1, Journals-Researchers, IRAN, 1987, Ch. 5.
- [14] B. Miller, *Proc. 6<sup>th</sup> Australian Electrochem. Conf.*, Geelong, Vic., 19-24 Feb., 1984; *J. Electroanal. Chem.*, 168 (1984) 91.
- [15] Jones, personal communication, 1992.

## **Author Guidelines EditEdit Author Guidelines**

### **GENERAL GUIDELINES FOR AUTHORS**

Journal of civil engineering researches invites unsolicited contributions of several forms: articles, reviews and discussion articles, translations, and fora. Contributions should fall within the broad scope of the journal, as outlined in the statement of scope and focus. Contributors should present their material in a form that is accessible to a general anthropological readership. We especially invite contributions that engage with debates from previously published articles in the journal.

Submissions are double-blind peer-reviewed in accordance with our policy. Submissions will be immediately acknowledged but due to the review process, acceptance may take up to three months. Submissions should be submitted via our website submission form (see links above for registration and login). Once you login, make sure your user profile has "author" selected, then click "new submission" and follow the instructions carefully to submit your article. If problems arise, first check the FAQ and Troubleshooting guide posted below. If you are still experiencing difficulty, articles can be submitted to the editors as email attachments.

Each article should be accompanied by a title page that includes: all authors' names, institutional affiliations, address, telephone numbers and e-mail address. Papers should be no longer than 10,000 words (inclusive of abstract 100-150 words, footnotes, bibliography and notes on contributors), unless permission for a longer submission has been granted in advance by the Editors. Each article must include a 100 words "note on contributor(s)" together with full institutional address details, including email address. We request that you submit this material (title page and notes on the contributors) as "supplementary files" rather than in the article itself, which will need to be blinded for peer-review.

We are unable to pay for permissions to publish pieces whose copyright is not held by the author. Authors should secure rights before submitting translations, illustrations or long quotes. The views expressed in all articles are those of the authors and not necessarily those of the journal or its editors. After acceptance, authors and Special Issue guest editors whose institutions have an Open Access library fund must commit to apply to assist in article production costs. Proof of application will be requested. Though publication is not usually contingent on the availability of funding, the Journal is generally under no obligation to publish a work if funding which can be destined to support open access is not made available.

### **Word template and guidelines**

Our tailored Word template and guidelines will help you format and structure your article, with useful general advice and Word tips.

## **(La)TeX template and guidelines**

We welcome submissions of (La)TeX files. If you have used any .bib files when creating your article, please include these with your submission so that we can generate the reference list and citations in the journal-specific style

### **Artwork guidelines**

Illustrations, pictures and graphs, should be supplied with the highest quality and in an electronic format that helps us to publish your article in the best way possible. Please follow the guidelines below to enable us to prepare your artwork for the printed issue as well as the online version.

Format: TIFF, JPEG: Common format for pictures (containing no text or graphs).

EPS: Preferred format for graphs and line art (retains quality when enlarging/zooming in).

Placement: Figures/charts and tables created in MS Word should be included in the main text rather than at the end of the document.

Figures and other files created outside Word (i.e. Excel, PowerPoint, JPG, TIFF, EPS, and PDF) should be submitted separately. Please add a placeholder note in the running text (i.e. "[insert Figure 1.]")

Resolution: Rasterized based files (i.e. with .tiff or .jpeg extension) require a resolution of at least 300 dpi (dots per inch). Line art should be supplied with a minimum resolution of 800 dpi.

Colour: Please note that images supplied in colour will be published in colour online and black and white in print (unless otherwise arranged). Therefore, it is important that you supply images that are comprehensible in black and white as well (i.e. by using colour with a distinctive pattern or dotted lines). The captions should reflect this by not using words indicating colour.

Dimension: Check that the artworks supplied match or exceed the dimensions of the journal. Images cannot be scaled up after origination

Fonts: The lettering used in the artwork should not vary too much in size and type (usually sans serif font as a default).

### **Authors services:**

For reformatting your manuscript to fit the requirement of the Journal of Civil Engineering Researchers and/or English language editing please send an email to the following address:

researchers.services@gmail.com

Noted: There is a fixed charge for these mentioned services that is a function of the manuscript length. The amount of this charge will be notified through a reply email.

## **FAQ AND TROUBLESHOOTING FOR AUTHORS**

I cannot log in to the system. How do I acquire a new user name and password?

If you cannot remember your username, please write an email to (journals.researchers@gmail.com), who will locate your username and notify you. If you know your username, but cannot remember your password, please click the "Login" link on the left-hand menu at homepage. Below the fields for entering your username and password, you will notice a link that asks "Forgot your password?"; click that link and then enter your email address to reset your password. You will be sent an automated message with a temporary password and instructions for how to create a new password. TIP: If you do not receive the automated email in your inbox, please check your SPAM or Junk Mail folder. For any other issues, please contact our Managing Editor, Kamyar Bagherinejad (admin@journals-researchers.com).

*How do I locate the online submission form and fill it out?*

First you need to register or login (see above). Once you are logged in, make sure the "roles" section of your profile has "Author" selected. Once you assign yourself the role of "Author," save your profile and then click the "New Submission" link on your user home page.

Once you arrive at the submission form page, please read the instructions carefully filling out all necessary information. Unless specified otherwise by the editors, the journal section to be selected for your submission should be "Articles." Proceed to the remaining sections, checking all boxes of the submission preparation checklist, and checking the box in the copyright notice section (thus agreeing to journals-researchers's copyright terms). Once the first page is completed, click "Save and Continue." The next page allows you to upload your submission. Use the form to choose your file from your computer. Make sure you click "Upload." The page will refresh and you may then click "Save and Continue." You will then proceed to a page for entering the metadata for your article. Please fill out all required fields and any further information you can provide. Click "Save and Continue." The next page allows you to upload supplementary files (images, audiovisual materials, etc.). These are not required, but if you wish to provide supplementary materials, please upload them here (do not forget to click "Upload." Then click "Save and Continue." This brings you to the final page of the submission form. Please click "Finish Submission" in order to close the

submission process. You will then be notified by email that your article has been successfully submitted. TIP: If you do not receive the automated email in your inbox, please check your SPAM or Junk Mail folder. For any other issues, please contact our Managing Editor, Kamyar Bagherinejad (admin@journals-researchers.com).

*Why am I not receiving any email notifications from HAU?*

Unfortunately, some automated messages from Open Journal Systems arrive in users' Spam (or Junk Mail) folders. First, check those folders to see if the message was filtered into there. You may also change the settings of your email by editing your preferences to accept all mail from [jcer] and related journals-researchers.com email accounts.

*I am trying to upload a revised article following an initial round of peer-review, but I cannot locate where to upload the article. Where do I submit a revised article?*

Follow the login process outlined above and when you successfully login you will see on your user home page a link next to "Author" for "active" articles in our system (usually it is only one article, but if you have multiple submissions currently in our system, the number could be higher. Click the "Active" link and you will be led to a page that lists your authored articles currently in our system. Click the link under the column labeled "Status" and this will take you to a page showing the current review status of your article. At the very bottom of the screen, you will see an upload form under the heading "Editor decision." Here you may upload your revised article. An automated email will be sent to the editors and you may also notify them directly via email. You may then logout.

I successfully submitted an article; how long will it take for the editors to respond to me with a decision.

For all articles that are recommended for peer-review, the editors of JCER strive to notify authors of a decision within 4-6 weeks. You may contact JCER's Managing Editor, Kamyar Bagherinejad (admin@journals-researchers.com). if you have any questions relating to the review process and its duration.

For all other inquiries, please contact: Kamyar Bagherinejad (Managing Editor)

## Privacy Statement

The names and email addresses entered in this journal site will be used exclusively for the stated purposes of this journal and will not be made available for any other purpose or to any other party.

## Articles

Section default policy

Make a new submission to the Articles section.

## Copyright Notice EditEdit Copyright Notice

Journal of Civil Engineering Researchers follows the regulations of the International Committee on Publication Ethics (COPE) and the ethical principles of publishing articles in this journal are set based on the rules of this committee, and in case of problems, it will be treated according to these rules.

This work is licensed under a Creative Commons Attribution 4.0 International License (CC BY 4.0).

In short, copyright for articles published in this journal is retained by the authors, with first publication rights granted to the journal. By virtue of their appearance in this open access journal, articles are free to use, with proper attribution and link to the licensing, in educational, commercial, and non-commercial settings

## Privacy Statement EditEdit Privacy Statement

The names and email addresses entered in this journal site will be used exclusively for the stated purposes of this journal and will not be made available for any other purpose or to any other party.

# Scholars Pavilion



**Scholars Pavilion** or **Scholars Chartagi** is a monument donated by the Islamic Republic of Iran to the United Nations Office at Vienna. The monument architecture is claimed by the Islamic Republic News Agency of Iran to be a combination of Islamic and Achaemenid architecture, although the latter clearly predominates in the decorative features, with Persian columns and other features from Persepolis and other remains from the Achaemenid dynasty. The Chahartaq pavilion form runs through the architecture of Persia from pre-Islamic times to the present.

Statues of four famous Persian medieval scholars, Omar Khayyam, Al-Biruni, Muhammad ibn Zakariya al-Razi and Ibn-Sina are inside the pavilion. This monument donated in June 2009 in occasion of Iran's peaceful developments in science.



**J-Researchers**